# From Angstroms to Nanometers: Measuring Interatomic Distances by Solid-State NMR

Alexander A. Shcherbakov[$], **João Medeiros-Silva**[$], **Nhi Tran**, **Martin D. Gelenter**, **Mei Hong**[*]

Department of Chemistry, Massachusetts Institute of Technology, 170 Albany Street, Cambridge, MA 02139

Abstract

Internuclear distances represent one of the main structural parameters in molecular structure determination using solid-state NMR spectroscopy, complementing chemical shifts and orientational restraints. Although a large number of magic-angle-spinning (MAS) NMR techniques have been available for distance measurements, traditional ^{13}C and ^{15}N NMR experiments are inherently limited to distances of a few angstroms due to the low gyromagnetic ratios of these nuclei. Recent development of fast MAS triple-resonance ^{19}F and ^{1}H NMR probes has stimulated the design of MAS NMR experiments that measure distances in the 1–2 nm range with high sensitivity. This review describes the principles and applications of these multiplexed multidimensional correlation distance NMR experiments, with an emphasis on ^{19}F- and ^{1}H-based distance experiments. Representative applications of these long-distance NMR methods to biological macromolecules as well as small molecules are reviewed.

Graphical Abstract
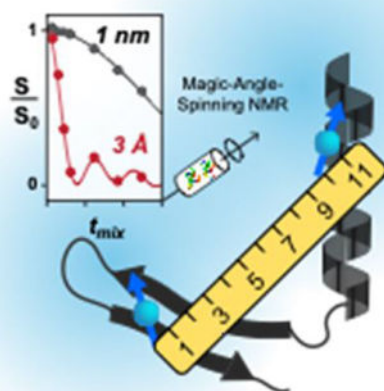
[*]Corresponding author: Mei Hong: meihong@mit.edu.
[$]These authors contributed equally.

The authors declare no competing financial interest.

1. Introduction

Structural studies of biomolecules using nuclear magnetic resonance (NMR) spectroscopy provide chemical shifts, orientation restraints, and inter-atomic distance restraints. Whereas chemical shifts reveal the chemical structure of functional groups and the three-dimensional structure in terms of bond torsion angles, distance restraints define the relative positions of atoms in space. In high-resolution magic-angle-spinning (MAS) solid-state NMR spectroscopy[1], distances between two atomic nuclei are measured through nuclear spin dipole-dipole coupling, $\omega_{12} \propto \gamma_1 \gamma_2 / r^3$. This dipolar coupling scales inversely with the cube of the distance r, and is proportional to the nuclear gyromagnetic ratio, γ, which determines the size of the magnetic dipole moment of the nucleus. Distance information is either encoded qualitatively in peak intensities in multidimensional correlation MAS NMR spectra[2–4], or measured quantitatively using dipolar recoupling experiments under MAS[5]. However, in biological molecules, some of the most common spin-1/2 nuclei such as ^{13}C and ^{15}N have relatively small γ, which makes it difficult to measure weak dipolar couplings for the structurally informative, long, distances within the relaxation time of the nuclear spins. The most common distance range that is measurable in ^{13}C and ^{15}N solid-state NMR experiments is less than 7–8 Å (Fig. 1A, B). A recent computational study found that, with distance restraints of < 7 Å, 9–15 distances per amino acid residue are required to obtain an accurate structural model of single-domain proteins[6]. Thus, for a moderately sized, 100-residue protein, over 1500 short-range distances would be required to determine an accurate structure. For multi-domain proteins or oligomeric proteins, even this large number of short-range distance restraints are insufficient to produce accurate structures, and additional data from other techniques such as cryoEM are required to define the relative positions and orientations of different domains. Therefore, long-range distance restraints are critical for determining the structures of multi-domain proteins and protein-protein complexes. Long-range distances also provide information about protein conformational changes in response to ligand binding, pH changes, and ion concentration changes, which are common in biology.

A number of approaches have been developed in the last decade to extend the distance reach of solid-state NMR spectroscopy. One approach is to measure paramagnetic relaxation enhancements and pseudocontact shifts caused by stable radicals or paramagnetic metal ions. This paramagnetic NMR approach can be exploited to provide information about distances above ~2 nm, where the uncertainty in the position of the flexible paramagnetic tag is small compared to the distance of interest. Paramagnetic NMR has been reviewed recently[7–9] and will not be discussed in the current review. Instead, this review focuses on the recent development of ^{19}F and ^{1}H solid-state NMR techniques for measuring long distances. ^{1}H and ^{19}F are the two highest-γ spin-1/2 nuclei among stable isotopes and can be readily exploited in MAS NMR experiments to measure distances to ~2 nm. We review multidimensional ^{19}F NMR techniques and ^{1}H-detected NMR techniques that are tailored to high magnetic fields and fast MAS conditions for distance measurement. We also review ^{13}C and ^{15}N NMR techniques that provide long distances through ^{1}H-mediated polarization transfer. We survey recent applications of these ^{19}F, ^{1}H, ^{13}C and ^{15}N long-distance techniques to membrane proteins, amyloid fibrils, and many biomolecular complexes. For

^{19}F NMR distance measurements, we also review some earlier applications to biomolecular systems to provide a more historical perspective.

2.   Heteronuclear ^{19}F-Based Distance Measurements

2.1   Long-Range ^{19}F Heteronuclear Distance NMR Techniques

Rotational-echo double-resonance (REDOR) is one of the most robust heteronuclear dipolar recoupling techniques in MAS solid-state NMR[10,11]. By applying two 180° pulses per rotation period to the observed and dephasing nuclei, one reintroduces distance-dependent dipolar couplings (Fig. 2A). This dipolar recoupling interferes with the formation of a spin echo, whose T_2-normalized intensity can be written as S/S_0, where S and S_0 denote the intensities of the dephased and control spectra, respectively. Since the invention of REDOR, a large number of heteronuclear and homonuclear dipolar recoupling sequences have been proposed and demonstrated in MAS NMR[12–14]. However, REDOR remains arguably the most widely used distance-measuring technique due to its simplicity and lack of scaling factors for the recoupled dipolar interaction. As a pulsed technique, REDOR has a relatively large recoupling bandwidth unless quadrupolar nuclei with large spectral widths are involved. Pulse imperfections in long REDOR pulse trains can be compensated for experimentally and taken into account in numerical simulations[15–17]. The simplicity of the REDOR pulse sequence also allows density operator propagation to be readily calculated for multi-spin systems[18,19]. These features make REDOR the method of choice for measuring heteronuclear distances.

The feasibility of long-distance measurement by solid-state NMR is determined by two factors: the buildup time for the dipolar coupling of interest and the nuclear spin relaxation time. Fig. 1B shows the dipolar coupling constant as a function of distances for common heteronuclear spin-1/2 pairs in solid-state NMR. Using 30 Hz as the lower bound of readily measurable dipolar couplings, heteronuclear distances involving ^{15}N cannot be measured beyond ~7 Å, whereas distances involving ^{19}F and ^{1}H can be measured to ~15 Å. The signal-to-noise ratio of the cross-polarization (CP) spectra (SNR_{CP}) that is required to measure REDOR distances with sufficient precision depends on the T_2 relaxation time of the observed spin and the desired precision of the S/S_0 values. Based on the propagated uncertainty ε of the S/S_0 value, it can be shown that $SNR_{CP} = \frac{1}{\varepsilon}\sqrt{1 + \left(\frac{S}{S_0}\right)^2}e^{t/T_2}$. Therefore, the higher the desired precision (small ε), the larger the required CP sensitivity. The shorter the T_2, the larger the required CP sensitivity (Fig. 1C, D).

To increase the dipolar coupling strength for a given distance, Schaefer and coworkers have long exploited the high-γ ^{19}F spin. An early example was the measurement of [13]C-^{19}F distances in the 143 kDa $\alpha_2\beta_2$ tetrameric enzyme, tryptophan synthase. ^{13}C-labeling of Tyr and 4-^{19}F labeling (4F) of Phe[20] allowed the authors to monitor four Tyr-Phe pairs in the β subunit that have [13]C-^{19}F distances of less than 8 Å. Binding of the ligand, Ser, caused only minor changes to [13]C-^{19}F REDOR dephasing, with an estimated distance change of less than 1 Å, indicating that ligand binding did not perturb the conformation of an indole tunnel in the enzyme. This pioneering work was conducted on a 4.7 Tesla NMR spectrometer (with a [19]F Larmor frequency of 188 MHz) using a quadruple-resonance (^{1}H,

^{19}F, ^{13}C and ^{15}N tuned) MAS probe, and the sample was spun at 5 kHz. Both ^{13}C-observed ^{19}F-dephased REDOR spectra and the reverse ^{19}F-observed ^{13}C-dephased REDOR spectra were measured.

In the 25 years since this study, increases in magnetic field strengths and MAS probes have led to significant advances in the ^{19}F REDOR NMR methodology. ^{19}F REDOR and Transferred-Echo Double Resonance (TEDOR) experiments have now been demonstrated for MAS frequencies of 20–40 kHz and at a magnetic field of 14.1 Tesla, corresponding to a ^{19}F Larmor frequency of 564 MHz[21–24]. The 1D REDOR pulse sequence has been extended to two dimensions, in order to extract many dipolar couplings from a single pair of 2D spectra, thus massively speeding up distance measurement and structure determination.

The first 2D-resolved ^{19}F REDOR experiment was reported by Rienstra and coworkers[21]. Using a 3.2 mm MAS probe simultaneously tuned to ^{1}H, ^{19}F, ^{13}C, and ^{15}N, the authors resolved the ^{15}N and ^{13}C chemical shifts in 2D NcaCX spectra while encoding the ^{15}N-^{19}F dipolar couplings by REDOR (Fig. 2B). In this so-called FRESH experiment, the ^{15}N REDOR 180° pulse is moved to define the t_1 period of a constant-time ^{15}N chemical shift period while retaining ^{15}N-^{19}F REDOR dipolar recoupling. The experiment was demonstrated on ^{13}C, ^{15}N-labeled GB1 containing a single fluorine at 5F-W43. Some of the strongest cross-peaks in the REDOR difference (S) spectra correspond to distances of 4.7–7.7 Å, and weaker cross-peaks corresponding to distances of 9–12 Å were also observed. The protein had a relatively low ^{19}F incorporation level of ~40%, which reduced the spectral sensitivity. Nevertheless, the eleven measured distances were found to be in good agreement with the high-resolution structure of this model protein.

Since the FRESH technique requires a quadruple-resonance HFCN probe, which is not widely available, Hong and coworkers introduced a triple-resonance 2D ^{13}C-^{13}C resolved ^{13}C-^{19}F REDOR technique in 2018[22]. The ^{13}C-^{19}F REDOR mixing period is inserted before the ^{13}C t_1 evolution time, thus encoding the C-F distances of carbons whose chemical shifts are manifested in the indirect dimension of the 2D spectrum (Fig. 2C). In this work, ^{13}C-^{13}C correlation was implemented using radiofrequency-driven recoupling (RFDR)[25], although many other polarization transfer sequences can also be used. Compared to the ^{15}N-^{19}F FRESH experiment, this 2D CC-resolved ^{13}C-^{19}F REDOR method has an intrinsically longer distance reach due to the 2.5-fold larger γ of ^{13}C than ^{15}N. The ^{13}C-^{19}F REDOR period features a selective Gaussian ^{13}C 180° pulse to remove the ^{13}C-^{13}C J-coupling and allow mixing times of ~10 ms to be used to measure long ^{13}C-^{19}F distances. These authors used 5F-W43 labeled GB1 and triply 3F-Tyr labeled GB1 to demonstrate this 2D CC resolved ^{13}C-^{19}F REDOR technique. Compared to the FRESH study, the authors increased the fluorine incorporation level to >95% by increasing the glyphosate concentration and optimizing the timing of the glyphosate addition[26]. With these improvements, the authors observed significant dipolar dephasing for many residues within 10 ms of REDOR mixing, and extracted 35 ^{13}C-^{19}F distances of 5–10 Å from the 2D ^{13}C-^{19}F REDOR spectra. The authors also investigated the effects of the ^{19}F chemical shift anisotropy (CSA) on REDOR dephasing using numerical simulations. At MAS frequencies that are smaller than the ^{19}F CSA, additional oscillations are observed in the REDOR dephasing that are absent in the universal REDOR curve[10,11,27] obtained under vanishing CSA. The large

^{19}F CSA also reduces the amplitude of REDOR dephasing to the first minimum. Fast MAS ameliorates these deleterious effects, restoring a nearly universal REDOR curve. Experimental parameters such as the radiofrequency (rf) field strength (ω_1) and the MAS rate (ω_r) are readily accounted for in the simulations.

An even longer distance ruler than ^{15}N-^{19}F and ^{13}C-^{19}F REDOR is ^{1}H-^{19}F REDOR, which exploits the two highest-γ nuclei among stable isotopes. Hong and coworkers first demonstrated this approach in 2004[28] by detecting the ^{1}H-^{19}F REDOR dephasing of amide protons through their directly-bonded nitrogens. In this proof-of-concept study, a slow MAS frequency of 3.3 kHz was used, therefore ^{1}H-^{1}H homonuclear decoupling was essential for prolonging the proton T_2 relaxation time. The experiment was demonstrated on the model peptide formyl-MLF[29,30], which incorporated 4F-Phe and ^{15}N-labeled Leu. The authors measured an H^N-F distance of 7.7 Å using REDOR mixing times up to ~6 ms. Because the ^{1}H-^{19}F dipolar couplings are scaled down by the homonuclear decoupling sequence, and the imperfection of homonuclear decoupling shortens ^{1}H T_2, the advantage of using the high-γ ^{1}H spin for distance measurement is diminished. Thus, this slow-MAS ^{1}H-^{19}F REDOR approach increased the distance reach by a modest margin compared to ^{13}C-^{19}F REDOR.

The bottleneck of ^{1}H homonuclear decoupling was decisively removed by the recent technological development of fast-MAS probes and the ensuing high-sensitivity ^{1}H-detected MAS NMR without complex ^{1}H homonuclear decoupling sequences. Combining the 2D-resolved REDOR approach with ^{1}H detection, Hong and coworkers introduced a ^{1}H-detected ^{1}H-^{19}F REDOR technique to measure many nanometer-range distances with high sensitivity[23]. The experiment inserts the ^{1}H-^{19}F REDOR period into a 2D ^{15}N-^{1}H heteronuclear correlation (HETCOR) pulse sequence. Amide protons that are close to the fluorine manifest intensities in the 2D REDOR difference ($\Delta S=S_0$-S) spectra (Fig. 2D). By combining the high-γ ^{1}H and ^{19}F spins, this 2D REDOR experiment significantly extends the distance reach compared to a ^{1}H-detected ^{1}H-^{13}C REDOR experiment[31]. The authors demonstrated this experiment on perdeuterated and ^{13}C,^{15}N (CDN)-labeled GB1 that was back-exchanged with protons. A single fluorine at 5F-W43 served as the dephasing nucleus. The average ^{1}H coherence lifetime was 4.2 ms at 30 kHz MAS and nearly doubled to 7.2 ms at 40 kHz MAS, underscoring the importance of fast MAS for measuring long distances. Amide protons that are within ~0.8 nm of the fluorine showed rapid dipolar dephasing to zero within 8 ms, while amide protons that are further than 1.3 nm from the fluorine still exhibited sizeable REDOR dephasing of S/S_0 ~0.8 within 10 ms. ^{1}H detection yielded high spectral sensitivity, with signal-to-noise ratios of 100–200 : 1 in the 2D control (S_0) spectra. Therefore, this ^{1}H-detected 2D ^{1}H-^{19}F REDOR technique allows rapid and multiplexed measurement of many nanometer-long distances. The main requirement of this technique is that the sample needs to be structurally sufficiently homogeneous to yield well-resolved 2D ^{15}N-^{1}H correlation spectra. The technique can in principle be extended to three dimensions to further resolve the signals. Such an extension will require quadruple-resonance HFCN probes.

2.2 Applications of ^{19}F Heteronuclear Distance Measurements to Biomolecules

2.2.1 Antimicrobial Peptides—The rapid spread of antibiotic-resistant bacteria has stimulated considerable efforts in understanding the mechanisms of action of antimicrobial compounds. Solid-state NMR spectroscopy is well suited for providing molecular insights into the structures and dynamics of these compounds. Many cationic antimicrobial peptides are produced by the innate immune system of animals[32,33] and are thought to operate by disrupting the membranes of microorganisms, but their detailed mechanisms of action were poorly understood. Schaefer and coworkers applied ^{19}F REDOR NMR to investigate an antimicrobial peptide called K3, (KIAGKIA)$_3$ (Fig. 3A)[34,35]. ^{13}C-^{19}F REDOR data of mixed ^{13}C and ^{19}F labeled peptides showed that the peptide forms parallel α-helical dimers in the membrane. By incorporating acyl-chain fluorinated DPPC and DPPG lipids, the authors measured the distances of the lipid tail from site-specifically labeled peptide carbonyls and from the lipid headgroups using ^{19}F-^{13}C and ^{19}F-^{31}P REDOR, respectively. These data indicate that the α-helical peptide is in close contact with the lipid tail. Moreover, the lipid tail – lipid headgroup ^{19}F-^{31}P distances decreased markedly from 9.9 Å in the peptide-free membrane to 7.6 Å in the peptide-bound membrane, indicating that the peptide increased membrane disorder (Fig. 3B, C). Based on these distance results, the authors proposed a toroidal-pore model for the mechanism of membrane permeabilization by this peptide.

Hong and coworkers employed ^{19}F REDOR NMR to determine the oligomeric structure of protegrin-1 (PG-1), a β-hairpin antimicrobial peptide[36]. ^{19}F Centerband-Only Detection of Exchange (CODEX) data showed that PG-1 forms dimers in 1-palmitoyl-2-oleoyl-sn-glycero-3-phosphocholine (POPC) bilayers. To determine whether these dimers are packed in a parallel or antiparallel fashion, and whether the dimer interface consists of the same strand or different strands of the β-hairpin, these authors incorporated ^{13}C and ^{19}F labels at the two ends of the C-terminal β-strand of the hairpin. The measured intermolecular ^{13}C-^{19}F REDOR dephasing indicates a ^{13}C-^{19}F distance of ~10 Å. This supports a parallel packing model in which the C-terminal strands of two β-hairpins face each other, while ruling out antiparallel models. Therefore, ^{13}C-^{19}F distance measurement was instrumental for constraining the oligomeric structure of the PG-1 dimers in lipid membranes.

^{19}F REDOR was also used to elucidate the binding site of a glycopeptide antibiotic in the cell walls of intact whole cells of *Staphyloccus aureus*[37]. Fluorinated oritavancin is a vancomycin analog that is effective against vancomysin-resistant enterococci. Schaefer and coworkers used ^{15}N-^{13}C TEDOR to suppress natural abundance ^{13}C signals and selectively detect only the signals of D-Ala ^{13}C that are adjacent to ^{15}N-labeled Gly in the cell wall peptidoglycan. The selected D-Ala ^{13}C signal was then subject to ^{19}F REDOR dephasing to measure the distance from oritavancin. The observed distance of 7.4 Å with a Gaussian distribution of 1.6 Å helped to constrain a molecular model of the peptidoglycan stems in complex with the drug.

^{13}C-^{19}F REDOR was used to investigate the self-assembly and sterol interaction of the antifungal compound, amphotericin B (AmB), in lipid bilayers. Murata and coworkers mixed ^{13}C-labeled AmB with fluorinated AmB and conducted ^{13}C-^{19}F REDOR experiments

to measure AmB-AmB separations in POPC bilayers[38]. The data show that the AmB-AmB separations are longer in ergosterol-containing POPC membranes compared to cholesterol-containing membranes. This result suggests that AmB forms a complex with ergosterol in lipid bilayers while self-aggregating and phase-separating from cholesterol in cholesterol-containing membranes. By combining fluorinated AmB with skip ^{13}C-labeled ergosterol and C26, C27-labeled ergosterol[39], the authors further measured AmB-ergosterol ^{13}C-^{19}F distances. The resulting distance distributions indicate heterogeneous AmB-ergosterol interactions, with both head-to-head and head-to-tail interactions possible.

2.2.2 Membrane Proteins—^{13}C-^{19}F REDOR has been fruitfully applied to α-helical membrane proteins to elucidate their structure and dynamics in lipid bilayers[4,40]. The influenza A M2 protein (AM2) is an acid-activated proton channel that is responsible for viral uncoating after endocytosis[41,42]. Proton selectivity and gating of this protein are accomplished by two residues, His37 and Trp41, respectively. Hong and coworkers measured the sidechain conformations and separations between these two functional residues using ^{13}C-labeled His37 and 5F-Trp41 and ^{13}C-^{19}F REDOR[43]. The REDOR dephasing is slower at high pH than at low pH, indicating that the imidazole ring and the indole ring approach each other more closely in the acidic open state of the channel compared to the neutral closed state of the channel. These results led to the model that cation-π interactions at low pH between His37 and Trp41 may be partially responsible for the orders of magnitude smaller proton flux (~1000 s^{-1}) of the channel compared to the measured microscopic histidine proton exchange rates of ~10^5 s^{-1} [44].

Long-range heteronuclear ^{19}F distances have also been used to probe the oligomeric structures of membrane proteins. Intermolecular distances in these systems are often too long to measure using low-γ nuclei such as ^{13}C and ^{15}N. Using ^{13}C-^{19}F REDOR experiments of mixed ^{13}C and ^{19}F labeled proteins, Hong and coworkers measured interhelical contacts that helped to constrain the high-resolution structures of the influenza BM2 proton channel[45] and the SARS-CoV-2 envelope (E) cationic channel[46]. For the tetrameric BM2, they incorporated 4F-Phe at the native Phe5 and Phe20, and mixed it with ^{13}C-labeled protein at a 1:1 ratio. REDOR dephasing of the ^{13}C signals by ^{19}F yielded distances of 4–8 Å. Moreover, the interhelical distances are longer for the low-pH open state of the channel than for the high-pH closed state, indicating that the four-helix bundle is more loosely packed in the open state (Fig. 4A–C). The final high-resolution structures of the closed and open BM2 channel show that the four-helix bundle activates in a scissor-like fashion, with the helices becoming more tilted and more separated from each other in the open state.

The same ^{13}C-^{19}F REDOR strategy was also used to determine the pentameric structure of the SARS-CoV-2 E protein. Solution NMR studies of detergent-bound E since the first SARS epidemic in 2003 yielded inconsistent information about the helical bundle structure, partly due to the scarcity of interhelical distance restraints[47,48]. Hong and coworkers measured interhelical distances using mixed ^{13}C and ^{19}F labeled proteins and 2D CC-resolved ^{13}C-^{19}F REDOR[46]. These experiments were carried out on the transmembrane peptide of E (ETM) bound to lipid bilayers that mimic the membrane of the endoplasmic reticulum Golgi intermediate compartment (ERGIC). Because ETM contains three native

and regularly spaced Phe residues (F20, F23 and F26), the authors also measured 2D ^{13}C-^{19}F HETCOR spectra to assign the ^{19}F signals. These data yielded 35 interhelical C-F distances, which helped to constrain the high-resolution structure of ETM in lipid bilayers (Fig. 4D–F). The authors also probed the binding site of fluorinated amantadine using ^{13}C-^{19}F REDOR, and found that the drug binds the N-terminus of the channel, in the same location as hexamethylene amiloride. The *de novo* structure determination of this SARS-CoV-2 membrane protein, carried out during the first six months of the COVID-19 pandemic, demonstrates the power of ^{19}F-based MAS NMR spectroscopy for protein structure determination.

In another study, ^{13}C-^{19}F REDOR was used to investigate the three-dimensional fold and topology of the HIV-1 fusion protein, gp41[49]. Despite considerable efforts, the structure of the transmembrane domain (TMD) and a membrane-proximal external region (MPER) of gp41 has been controversial in the literature. One discrepancy pertains to whether the MPER is kinked from the TMD or forms a continuous helix. Hong and coworkers incorporated ^{13}C-labeled residues into the TMD and fluorinated Trp678 into the MPER, and measured ^{13}C-^{19}F distances using REDOR. The continuous helix model would predict longer ^{13}C-^{19}F distances (11–13 Å) than the kinked helix model (9–10 Å). The authors found significant dipolar dephasing for I686 and L684 Cα, which correspond to distances of 9–10 Å from the Trp678 sidechain[49]. Thus, these REDOR data indicate that the MPER-TMD adopts a helix-turn-helix topology in lipid bilayers. Combined with ^{19}F CODEX data (see section 3.4.3 below), these results led to a trimeric umbrella-like fold, which differs from structures found in micelles and bicelles[50,51], suggesting the influence of the membrane environment on gp41 assembly.

2.2.3   Nucleic Acids—Nucleic acids are much less studied than proteins by NMR due to challenges associated with their low sequence complexity and the resulting spectral overlap. ^{31}P-^{19}F REDOR[52] is an effective probe of nucleic acid structures because of the presence of the high-γ ^{31}P in the nucleic acid backbone and the feasibility of fluorination reactions of aromatic substrates. Drobny and coworkers pioneered the approach of incorporating phosphorothioate (pS) and fluorinated nucleotides such as 2'-deoxy-5-fluorouridine and 2'-deoxy-2'-fluorouridine to measure nanometer ^{31}P-^{19}F distances in DNA and RNAs[53]. The substitution of a single non-bridging oxygen atom by a sulfur shifts the ^{31}P chemical shift downfield by ~55 ppm, thus giving a well-resolved reporter of the nucleotide without perturbing the backbone conformation[54].

Using this ^{31}P-^{19}F REDOR technique, Drobny and coworkers investigated the minor groove width of a DNA oligonucleotide duplex upon binding by a peptide antibiotic, distamycin[55]. The DNA duplex contains a 2'F-adenine in one chain and a phosphorothioate tag 3.5 residues away from the fluorinated base pair in the other chain. ^{31}P-^{19}F REDOR data showed that the minor groove width is 9.4 Å in the absence of the drug. However, addition of distamycin to a 1 : 1 ratio caused a major distance decrease to 7.0 Å, whereas addition of the drug to a 2:1 ratio caused a major distance increase to 13.6 Å. Thus, these ^{31}P-^{19}F REDOR data revealed a striking structural change of the DNA upon drug binding.

The same approach of phosphorothioate tagging and nucleotide fluorination was also applied to study structural changes of the RNA, HIV TAR, upon binding to the viral regulatory protein tat[56]. By installing ^{31}P and ^{19}F labels at A27 and U23, respectively, Drobny and coworkers measured ^{31}P-^{19}F distances, and found that tat binding dramatically shortened the distance from 10.3 Å to 6.6 Å (Fig. 5). Thus, ^{31}P-^{19}F REDOR yields insights into the impact of the protein on the conformation of the HIV TAR.

Additional studies of protein-nucleic acid complexes explored the flexibility of orthogonal ^{13}C, ^{15}N-labeling of the protein and fluorination of the oligonucleotide. For example, Drobny and coworkers investigated the interactions between the tat protein and TAR RNA using a ^{13}C, ^{15}N-Arg labeled peptide and 5-^{19}F-uracil labeled RNA[57]. REDOR dephasing of the ^{13}C and ^{15}N signals by ^{19}F yielded distances of 5.6 and 6.6 Å for the Arg Cζ and CO and ^{15}N-^{19}F distances of 4.3 – 6.7 Å. These distances constrained the position of R52 with respect to U23 of the RNA, in good agreement with a solution NMR structure of the tat-TAR complex.

Stivers, Schaefer and coworkers used ^{31}P-^{19}F REDOR to investigate nucleotide binding by a DNA repair enzyme, uracil DNA glycosylase (UDG)[58]. They introduced a difluorophenyl nucleotide, an analog of uracil, into a DNA duplex, and measured its binding to UDG. These ^{31}P-^{19}F distances can vary from 6 Å to 18 Å, depending on the conformation of uracil. The measured distances indicate a 50 : 50 mixture of B-form DNA and an out-flipped state for the nucleotide. Together with chemical shift and biochemical data, these results led to the conclusion that the difluorophenyl nucleotide forms a metastable intermediate with the enzyme, but the lack of hydrogen bonding precluded the formation of a catalytically productive Michaelis complex.

2.2.4   Biological Assemblies and Protein-Ligand Complexes—^{19}F REDOR

NMR has been extensively used to study protein-ligand complexes. An early application of ^{31}P-^{19}F REDOR was to the enzyme 5-enolpyruvylshikimate-3-phosphate (EPSP) synthase bound to two ligands, shikimate 3-phosphate (S3P) and glyphosate (Glp)[59]. EPSP catalyzes an intermediate step in the biosynthesis of aromatic amino acids via the shikimate pathway. The protein contains only two Trp residues, which were biosynthetically labeled as 6F-Trp, while both ligands contain native ^{31}P atoms, whose chemical shifts are resolved by 12 ppm. Schaefer and coworkers measured ^{31}P-^{19}F distances between each Trp and the ligands. The measured distances of 8.5 Å to 16 Å indicate that the C-shaped apo-enzyme clamps down on the ligands to form a globular ternary complex. This study demonstrated how nanometer distances can give insight into the structure of large protein-ligand complexes.

^{19}F REDOR has proven to be useful for constraining the oligomeric structures of large membrane receptors. The dimeric bacterial chemotaxis receptor forms clusters in lipid membranes whose structures were not known. Thompson and coworkers tested two structural models, a linear array 'hedgerow' model and a clustered 'trimer-of-dimers' model, using ^{13}C-^{19}F REDOR[60]. 4F-Phe and ^{13}C-labeled residues were introduced into the protein. The ^{13}C-^{19}F REDOR data yielded inter-dimer distances that are longer than predicted by both models, thus providing constraints to the protein structure.

[19]F REDOR has been applied to study cholesterol interaction with influenza AM2[61]. Employing isooctyl tail-fluorinated cholesterol and site-specifically ^{13}C-labeled peptides, Hong and coworkers measured [13]C-^{19}F REDOR spectra. The data show that cholesterol binds AM2 in the presence of an amphipathic helix (AH), but does not bind the transmembrane (TM) helix in the absence of the AH. In AH-containing peptides, the REDOR S/S_0 values decayed to a minimum of 0.5, indicating an unexpected protein : cholesterol binding stoichiometry of 2 : 1. Simulations of the REDOR data yielded distances of 7.0 to 9.3 Å, which provided crucial constraints to the structural model of the AM2-cholesterol complex in the membrane.

Intermolecular [13]C-^{19}F REDOR was also applied to understand the interaction between cholesterol and the HIV-1 fusion protein, gp41[62]. A gp41 peptide, MPER-TMD, was fluorinated at two aromatic residues, 4F-F673 and 5F-W680, and was combined with biosynthetic ^{13}C-labeled cholesterol in a virus-mimetic lipid bilayer. The latter was obtained from a mutant yeast strain that replaced ergosterol synthesis enzymes with cholesterol synthesis enzymes[63,64]. [13]C-^{19}F REDOR data indicate that the cholesterol C9 and C17 atoms approach the F673 sidechain with a distance of 7.0 Å. Moreover, a cholesterol recognition motif (CRAC) is not necessary for this complexation. By comparing protein ^{13}C-detected and cholesterol ^{19}F-detected REDOR data, these authors found that three cholesterol molecules bind each gp41 trimer at the protein/cholesterol molar ratio of 1:7 used in these samples.

When no structure information is available, REDOR based on site-specific isotopic labeling is inefficient for studying protein-ligand binding. Instead, the 2D multiplexed [1]H-^{19}F REDOR technique is much more efficient for structure determination. This approach was recently demonstrated by Hong, Henzler-Wildman, and coworkers for structure determination of the bacterial transporter, EmrE[65]. EmrE confers multidrug resistance to bacteria, but has eluded high-resolution structure determination for decades due to its conformational plasticity. Using 2D [1]H-^{15}N resolved [1]H-^{19}F REDOR experiments of CDN-labeled protein bound to a fluorinated ligand, tetraphenylphosphonium (TPP[+]), the authors measured 214 protein-ligand distances from 5.8 Å to 12 Å. These distances constrained a 2.1 Å structure of the dimeric protein in dimyristoyl-phosphatidylcholine (DMPC) bilayers (Fig. 6A–C). Moreover, the [1]H-^{19}F distances showed that TPP lies closer to one subunit of the protein than the other, thus explaining the asymmetric proton dissociation constant of the proton-binding residue, Glu14.

In some cases, the ligand conformation when bound to its protein target is unknown and can be defined using ^{19}F REDOR NMR. Bryostatin 1 is a protein kinase C (PKC) modulator that has shown promise in oncology, neurology, and infectious diseases. Cegelski, Schaefer and coworkers investigated the structure of a bryostatin analog, bound to the PKC receptor in lipid membranes by measuring [13]C-^{19}F, [13]C-^{2}H, and [2]H-^{19}F REDOR spectra of a triply ^{13}C, ^{2}H, and ^{19}F labeled analog[67]. The measured distance distributions (Fig. 6D, E)[66] show a long-distance component of 10–13.5 Å that coexists with a minor component of a ~6 Å distance. The latter cannot arise from intramolecular dephasing and must be attributed to intermolecular PKC dimers. MD simulations based on these distance restraints led to a

model of the membrane-bound PKC-bryolog complex, and suggested that design of future PKC modulators should consider the conformational flexibility of the ligand.

2.3 ^{19}F-Based Heteronuclear Correlation NMR Experiments

While ^{19}F REDOR NMR provides important long-range distance constraints, in systems containing multiple fluorines, ^{19}F resonance assignment becomes necessary. This assignment can be achieved by correlating ^{19}F chemical shifts with ^{13}C or other nuclei in 2D or 3D HETCOR spectra. Polenova and coworkers recently demonstrated a 2D [19]F-^{13}C HETCOR experiment using [19]F-^{13}C cross polarization (CP) for polarization transfer and dynamic nuclear polarization (DNP) for sensitivity enhancement (Fig. 7A)[68]. Since no DNP probe that simultaneously tunes ^{1}H, ^{19}F, and X was available at the time of this study, these authors tuned the ^{1}H channel of an HXY probe to [19]F. Even in the absence of ^{1}H decoupling, by using a MAS rate of 24 kHz and high-power ^{19}F and ^{13}C pulses, the authors obtained sufficiently resolved spectra. Absolute ^{19}F sensitivity enhancement factors of 12–29 were obtained. The authors demonstrated this DNP 2D [19]F-^{13}C HETCOR experiment on 5F-Trp labeled HIV-1 capsid tube assembly. The observed [19]F-^{13}C correlations correspond to distances of 8–11 Å, including both intramolecular and intermolecular contacts.

[13]C-^{19}F HETCOR spectra can also be obtained using REDOR as the polarization transfer building block. Hong and coworkers showed that TEDOR transfer from ^{13}C to ^{19}F for detection has higher efficiency and sensitivity compared to out-and-back sequences and compared to ^{13}C-detected TEDOR[24]. Applied to the influenza BM2 TM peptide, they observed cross peaks between ^{13}C-labeled Ile14 and 5F-Trp23, which can only arise from antiparallel packed BM2 tetramers (Fig. 7B).

In addition to [13]C-^{19}F HETCOR, [1]H-^{19}F HETCOR experiments were introduced recently. By combining [1]H-^{19}F CP with [1]H-^{1}H or [19]F-^{19}F RFDR recoupling, Su and coworkers conducted 3D [19]F-[1]H-[1]H (FHH) and [19]F-[19]F-[1]H (FFH) correlation experiments under 60 kHz MAS (Fig. 7C)[69]. Since both ^{1}H and ^{19}F are 100% abundant, these experiments do not require isotopic enrichment and are thus well suited to studies of pharmaceutical compounds. These authors demonstrated these experiments on aprepitant in its crystalline form and as a nanoparticulate formulation, EMEND. They obtained high spectral sensitivity and resolution by ^{1}H detection under 65 kHz MAS. These [19]F-^{1}H HETCOR spectra showed that the structure of the active pharmaceutical ingredients (API) is similar between the crystalline form and the drug formulation. Moreover, the 3D FHH spectra show correlations between the aromatic fluorine and one of the CF_3 groups, giving information about the conformation of the API.

2.4 ^{19}F Heteronuclear NMR for Pharmaceutical Sciences

Over 30% of pharmaceutical compounds contain fluorines[70], making ^{19}F NMR well suited for molecular structural characterization. Considerable efforts in the pharmaceutical industry center on the improvement of drug delivery strategies and product stability, where understanding the physiochemical properties of API's and excipients is crucial for drug formulation. ^{19}F NMR is a sensitive technique for understanding the interactions of API's with excipients, and for probing the local structure in amorphous solid drug products. In

crystalline pharmaceuticals, characterizing the packing of the drug product is important for maintaining product quality profiles.

Fast MAS ^{19}F-^1H HETCOR experiments were recently applied to posaconazole (POSA), the API in an antifungal drug. Su and coworkers detected intermolecular ^1H-^{19}F correlation signals under 60 kHz MAS, consistent with the presence of both "head-to-head" and "head-to-tail" packing in the crystalline lattice[71]. The authors also studied an amorphous form of POSA using ^{19}F-^1H HETCOR, ^{13}C-^{19}F CP, and ^{13}C-^{19}F REDOR[72]. The ^{13}C-^{19}F REDOR data indicate intermolecular distances of 3–5 Å for "head-to-tail" contacts. Interestingly, one ^{13}C-^{19}F distance increased from 3.3 Å to 6.2 Å between the crystalline and amorphous forms, suggesting that the amorphous form of the drug lacks the head-to-head packing. ^{19}F NMR was also used to probe the interactions between POSA and an excipient, hypromellose acetate succinate (HPMCAS), to understand the structural basis of the stability of amorphous solid dispersions (ASD)[73]. Using a symmetry-based sequence, $SR4_1^2$, for ^{13}C-^{19}F dipolar recoupling, Su and coworkers measured an intermolecular distance of 6.0 Å in the ASD, indicating head-to-tail packing. ^{13}C-^{19}F REDOR data of fluorinated POSA and a ^{13}C-carboxyl group in HPMCAS showed a distance of 4.3 Å, suggesting the possible interactions that stabilize the ASD. These studies demonstrate the power of ^{19}F solid-state NMR for giving molecular insights into the structures of pharmaceutical compounds.

3. Homonuclear ^{19}F-^{19}F Distance Techniques

Complementary to heteronuclear ^{19}F NMR, homonuclear ^{19}F-^{19}F dipolar NMR is an effective approach for measuring nanometer distances when multiple fluorines are present in a system. Due to the high gyromagnetic ratio of ^{19}F, ^{19}F-^{19}F dipolar couplings are 14-fold stronger than ^{13}C-^{13}C dipolar couplings for the same distance. This enables ^{19}F-^{19}F distances up to ~2 nm to be measured, either qualitatively as cross peaks in 2D spectra or more quantitatively as buildup rates or decay rates. Homonuclear ^{19}F-^{19}F distances can be measured using two NMR approaches: isotropic spin exchange and anisotropic spin exchange.

3.1 Principle of Isotropic ^{19}F Spin Exchange

When multiple fluorines are spectrally resolved, 2D ^{19}F-^{19}F correlation experiments allow the extraction of qualitative distance information from cross-peak intensities. Conventional spin diffusion experiments such as proton-driven spin diffusion (PDSD) and combined R_n^v-driven spin diffusion (CORD)[74] have been applied to ^{19}F-^{19}F distance measurements[75,76] Under relatively fast MAS rates of 20 kHz or higher, this ^{19}F isotropic spin exchange is more efficient with ^1H irradiation (CORD and DARR) than without (PDSD). Because ^{19}F labels are usually sparse in a biomolecular system, these ^{19}F-^{19}F cross peak intensities largely encode direct distances. This differs from ^{13}C-^{13}C spin exchange in uniformly ^{13}C-labeled proteins, where cross peaks reflect relayed polarization transfer and dipolar truncation effects[77], thus limiting the accuracy of the distance extraction. If multiple ^{19}F spins happen to be in close proximity, for example for a multi-fluorinated aromatic ring, then care should be taken to account for dipolar truncation effects in interpreting the ^{19}F-^{19}F cross peak intensities[75,78].

The first analytical treatment for quantifying ^{19}F-^{19}F distances from isotropic spin exchange was shown by Hong and coworkers[75]. They calibrated spin exchange rates (k_{sd}) using structurally known model compounds for ^{19}F spectra measured under 25–35 kHz MAS at a moderately high magnetic field of 14.1 T. For spin exchange in the weak-coupling limit, the product of k_{sd} with the square of isotropic shift difference ($k_{SD}\,\delta_{iso}^2$) depends on the distance as $1/r^6$:

$$k_{SD}\Delta\delta_{iso}^2 = 0.5\pi f_0 \omega_d^2 = \frac{c}{r^6}$$

Here f_0 is a phenomenological constant in the overlap integral between the normalized single-quantum lineshapes of the two spins; δ_{iso} is the isotropic chemical shift difference; and ω_d is the dipolar coupling. By measuring cross-peak intensity buildup rates of model compounds with known F-F distances (Fig. 8A), one can obtain the constant c. 2D spectra of model compounds containing both aromatic fluorines and aliphatic CF_3 show that CF_3-F polarization transfer was more efficient than F-F polarization transfer, reflecting the stronger dipolar coupling of three closely spaced fluorines in the trifluoromethyl group than a single F to a remote fluorine (Fig. 8B).

The effectiveness of this isotropic ^{19}F spin exchange for distance measurement in proteins was demonstrated by Hong and coworkers on the microcrystalline protein GB1[75] and by Polenova and coworkers on the HIV-1 capsid protein tubular assemblies[76]. Fast MAS rates of 25–60 kHz and high magnetic fields of 14.1 T and 19.96 T were used for these studies, to obtain high spectral sensitivity and resolution. 3F-Tyr labeled GB1 and 5F-Trp labeled HIV-1 CA proteins were produced by adding glyphosate to the bacterial culture prior to protein expression. For GB1, inter-Tyr cross peaks for distances of 0.5 nm to 1.6 nm were observed using ^{19}F CORD spin diffusion with mixing times up to ~300 ms under 25 kHz MAS (Fig. 8C). The measured cross peak buildup time constants follow the $1/r^6$ dependence after correcting for chemical shift differences. Thus, ^{19}F spin exchange can be analyzed to give semi-quantitative distances. For the HIV capsid protein, inter-Trp cross peaks for distances up to 2 nm were observed, using PDSD spin diffusion with mixing times up to 1 s under 35 kHz MAS.

3.2. Applications of ^{19}F Isotropic Spin Exchange to Structural Biology

3.2.1 HIV-1 Capsid Protein

—Polenova and coworkers applied the 2D ^{19}F correlation NMR approach to measure long distances in the HIV-1 capsid protein tubular assemblies[76]. The 25.6 kDa CA oligomerizes into hexameric subunits (Fig. 8D) arranged in a hexagonal lattice. 2D ^{19}F-^{19}F correlation spectra of 5F-Trp labeled CA measured at 19.96 T show narrow ^{19}F linewidths of 0.3–1.0 ppm even without ^{1}H decoupling for MAS frequencies of 35 to 60 kHz. With 1 s ^{19}F spin diffusion at 35 kHz MAS, multiple ^{19}F-^{19}F correlations were observed, among which the W23-W80 cross peak corresponds to the longest distance of 23 Å (Fig. 8D). Applying DNP[68], these authors showed that the ^{19}F spectral sensitivity can be enhanced up to 100-fold. This was achieved in CA samples containing 22 mM of the biradical AMUPol and spun at 24 kHz MAS. Polarization transfer from the unpaired electrons of the biradical to ^{19}F and the subsequent transfer among ^{19}F spins are efficient,

as shown by the similar sensitivity enhancements for ^{19}F and ^{1}H. Because the ^{19}F spin density is low, the ^{19}F DNP buildup times are much longer (9.5–14.4 s) than the ^{1}H buildup times (0.9–4.3 s). The ^{19}F buildup times also show little dependence on the biradical concentration, consistent with a lack of relayed polarization transfer. This DNP condition was also used to obtain high-sensitivity 2D ^{19}F-^{13}C HETCOR spectra in the absence of ^{1}H decoupling.

3.2.2 Protein-Lipid Interactions—Homonuclear ^{19}F NMR, like its heteronuclear analog, is well suited to characterize small-molecule interactions in biological membranes. Hong and coworkers recently applied 2D ^{19}F-^{19}F isotropic spin exchange to investigate cholesterol clustering in lipid membranes[79]. An isooctyl tail fluorinated cholesterol, F$_7$-cholesterol, contains two CF$_3$ groups and a CF moiety. Interestingly, the ^{19}F spectra resolve two CF$_3$ peaks (−76 ppm and −78 ppm) at high cholesterol concentrations but only one CF$_3$ peak (−76 ppm) at low concentrations. ^{19}F CODEX experiments (see section 3.4.4 below) indicate that the −76 ppm peak results from cholesterol dimers whereas the −78 ppm peak arises from cholesterol tetramers. 2D ^{19}F-^{19}F correlation spectra measured with 40 ms CORD revealed cross peaks between these two CF$_3$ signals, indicating tail-to-tail contacts between cholesterol dimers and tetramers. This study represents the first observation of oligomeric cholesterol assemblies in phospholipid bilayers.

Fluorinated cholesterol also allowed the study of cholesterol binding to the HIV fusion protein, gp41, using 2D ^{19}F-^{19}F correlation NMR[62]. By combining F$_7$-cholesterol with 4F-Phe and 5F-Trp labeled gp41, cholesterol-gp41 contacts were observed as cross peaks in 2D ^{19}F correlation spectra. These spectra were measured using 500 ms CORD mixing under 10 kHz MAS on a 9.4 T magnet. The MPER-cholesterol cross peaks indicate that the cholesterol tail lies within 2 nm of the surface-bound MPER helix. Together with ^{13}C-^{19}F REDOR data, these led to the proposal that three cholesterol molecules bind each gp41 trimer, and suggest that the MPER-TMD helix-turn-helix structure might sequester cholesterol for function.

3.3 Principle of Anisotropic ^{19}F Spin Exchange

Multiple ^{19}F spins of the same residue in a homo-oligomeric assembly have the same isotropic chemical shift, but usually have different anisotropic chemical shifts due to the different orientations of the ^{19}F chemical shift tensors. Distances between these ^{19}F spins can be measured using the Centerband-Only Detection of Exchange (CODEX) technique, originally developed by Schmidt-Rohr and coworkers for studying slow motion.[80,81] The ^{19}F spin diffusion CODEX experiment[82,83] encodes anisotropic spin exchange between orientationally inequivalent ^{19}F spins through a stimulated spin echo. Rotor-synchronized 180° pulses are applied to recouple the ^{19}F CSA under MAS (Fig. 9A). Two trains of 180° pulses before and after a mixing period (t_m) create a stimulated echo. If spin diffusion between fluorines with different chemical shift tensor orientations occurs during t_m, then it changes the ^{19}F CSA, thus preventing the complete refocusing of the stimulated echo. The echo intensity decrease thus provides information about the distance-dependent dipolar coupling. The CODEX experiment is conducted in pairs, with the control spectrum (S_0) correcting for T$_1$ relaxation effects for the exchange spectrum (S) through the intensity ratio,

S/S_0 (Fig. 9B). At sufficiently long mixing times, the magnetization is equally distributed among n orientationally distinct spins, giving an equilibrium intensity of $1/n$. Therefore, the equilibrium CODEX intensity reflects the oligomeric number, whereas the rate of CODEX intensity decay encodes the internuclear ^{19}F-^{19}F distance (Fig. 9C).

The ^{19}F CODEX decay curves can be quantified using an exchange-matrix formalism to extract distances[82]. The principle of this formalism is the same as the isotropic spin exchange analysis, but takes into account the multi-spin nature of the problem. As before, the only adjustable parameter in this distance extraction is the overlap integral between the lineshapes of the two spins, which depends on the ^{19}F CSA and MAS frequency. The value of this overlap integral can be calibrated using structurally known model compounds, and was found to vary between 15 and 40 μs for MAS frequencies below 35 kHz and at magnetic field strengths of 9.4 T and 14.1 T[75,82]. At these MAS rates, anisotropic spin exchange is more efficient in the absence of ^1H irradiation (i.e. PDSD) than in the presence (e.g. DARR), in contrast to isotropic spin exchange. This indicates that ^1H-^{19}F recoupling broadens the spectral lineshapes, thus reducing the overlap integral. To ensure that this ^{19}F CODEX technique detects spin diffusion instead of millisecond timescale motion, the experiments must be conducted at low temperature where molecular motions are frozen. For membrane proteins, ^{19}F CODEX is typically conducted well below the phase transition temperature of the lipid membrane.

3.4 Application of ^{19}F CODEX to Biomolecules

3.4.1 Influenza M2 Proton Channels—^{19}F spin diffusion CODEX has been extensively applied to the tetrameric M2 channels of influenza A and B viruses[41,42]. These studies incorporated fluorines into native Phe and Trp residues as 4F-Phe and 5F-Trp. All studies found that the ^{19}F CODEX echo intensities decayed to 0.25, thus directly showing the tetrameric nature of these peptides in lipid bilayers (Fig. 9C).

In addition to confirming the tetrameric nature of the peptides, ^{19}F CODEX has provided mechanistic insights into the conformation of the gating Trp residue in M2 channels. Both influenza AM2 and BM2 contain an HxxxW motif, which is essential for the proton selectivity and channel gating. 5F-Trp incorporated into the M2 peptides was used to probe the structural dynamics of this functional motif. ^{19}F CODEX experiments of 5F-Trp41 in AM2[84] yielded a nearest-neighbor ^{19}F-^{19}F distance of ~11 Å in DMPC bilayers. This distance constrained the Trp41 sidechain to the t90 rotamer ($\chi_1 \sim 180°$, $\chi_2 \sim 90°$). Together with a His37 Nδ1–Trp Cγ distance of 3.8 Å[85], these F-F distances implied a His37 sidechain conformation of t-160, which points the imidazole ring to the pore. These interhelical Trp41 distances in DMPC bilayers were relatively insensitive to pH. Subsequent experiments on AM2 bound to a virus-mimetic membrane refined these interhelical F-F distances to 11.3 Å and 12.4 Å at high and low pH, respectively[43]. These values indicate that the Trp41 χ_2 angle differs by 15–20° between high pH and low pH. Moreover, C-H dipolar couplings measured at high temperature indicate that the Trp41 sidechain undergoes larger-amplitude torsional fluctuations at low pH than at high pH. This implies periodic close contacts between the cationic His37 imidazolium and the Trp41 indole at low pH. Thus, these data support a dynamic gating model for the HxxxW motif of the M2 channel.

Influenza BM2 is a functional analogue of AM2 but exhibits little sequence homology. Although the amantadine class of antiviral drugs inhibit AM2, they are ineffective against BM2. [19]F CODEX of BM2's TM peptide was measured using 4F-Phe5[86]. The CODEX decay curves were found to be bimodal, centered at 7 Å and 15 Å, suggesting a rectangular geometry for the four-spin cluster. The long-distance component indicates a wide N-terminal pore, which is consistent with the lack of binding of amantadine to the BM2 channel. Further studies of BM2 at different pH found that the gating residue, Trp23, has pH-dependent interhelical distances (Fig. 9C)[87]. The distances increased from 9.4 Å at pH 7.5 to 10.5 Å at pH 4.5. This channel pore widening was attributed to electrostatic repulsion between the cationic His19 at low pH. Thus, ^{19}F CODEX data revealed subtle structural differences between AM2 and BM2 proton channels.

3.4.2 Antimicrobial Peptides and Cell-Penetrating Peptides—Antimicrobial peptides (AMPs) and cell-penetrating peptides (CPPs) modulate the physical properties of lipid membranes, to cause membrane permeation for host defense and to transport cargo into the cell. Both AMPs and CPPs are cationic and Arg-rich peptides, and share common features in many proposed mechanisms of action[32,33]. ^{19}F CODEX NMR has been useful for determining the oligomeric structure of these membrane-active peptides.

The first application of ^{19}F CODEX to AMP was to study the β-hairpin peptide PG-1[83]. Hong and coworkers introduced 4F-Phe at a native Phe12 in the C-terminal strand, and measured an equilibrium CODEX intensity (S/S$_0$) of 0.56. This result indicates that PG-1 oligomerizes into at least dimers, with two C-terminal strands in close proximity. Additional [13]C-^{15}N, [1]H-^{13}C and [13]C-^{19}F REDOR experiments revealed that the two peptides are aligned in parallel[36]. Interestingly, when 4F-phenylglycine (Phg) was introduced at residue 7 in the N-terminal strand, the ^{19}F CODEX data also showed intensity decays, with an equilibrium value of 0.45, indicating that the N-terminal strand is also dimerized[90]. Thus, the β-hairpins assemble into a larger oligomer like a β-barrel in the membrane. Simulations of the CODEX decays yielded [19]F-^{19}F distances of 9.0 Å for Phg$_7$ at the N-N interface and 6.5 Å for Phe$_{12}$ at the C-C interface. These distances and other biochemical data led to a structural model of a transmembrane β-barrel across the 1-palmitoyl-2-oleoyl-sn-glycero-3-phosphoethanolamine (POPE) / 1-palmitoyl-2-oleoyl-sn-glycero-3-phosphoglycerol (POPG) membrane. Additional [13]C-^{31}P REDOR data of Arg-labeled PG-1 indicate that the POPE/POPG membranes exhibit significant defects where some of the lipid headgroups are inserted into the membrane interior to form salt bridges with the guanidinium sidechains of Arg residues[91]. These results indicate that PG-1 forms a toroidal pore to disrupt the bacterial membrane.

[19]F CODEX was used to investigate the concentration-dependent self-assembly of the antibiotic peptide, alamethicin. This 19-residue peptaibol, rich in α-aminoisobutyric acid (Aib) residues, forms α-helical bundles of varying sizes. At high concentrations alamethicin can form ion-conducting TM pores. Bechinger and coworkers incorporated a CF$_3$ group into alamethicin and conducted the ^{19}F CODEX experiment under 15 kHz MAS on a 500 MHz spectrometer. The CODEX equilibrium value of the POPC-bound alamethicin showed a sensitive dependence on the peptide/lipid (P/L) molar ratio. At a P/L of 1:13, an equilibrium value of 0.186 was obtained, while at a lower P/L of 1:30, the equilibrium

value increased to ~0.5. Therefore, alamethicin associates into pentamers and dimers at high and low concentrations, respectively[88] (Fig. 9D). This study also determined the overlap integral of CF_3 groups, yielding a 10-fold higher value of 450 μs compared to the values for CF groups, consistent with the faster isotropic spin exchange observed between CF_3 and F groups[75].

The same authors applied ^{19}F CODEX to a 10-residue analog of alamethicin, trichogen, to understand its membrane-bound structure and assembly. Trichogin adopts a membrane-surface topology at low concentrations[89] but induces ion leakage from liposomes in a concentration-dependent manner. ^{19}F CODEX experiments on POPC-bound trichogin found a tetramer with F-F distances of 9–9.5 Å at a high P/L of 1:8. In comparison, EPR data showed dimer formation at a lower P/L of 1:20 (Fig. 9E). Oriented membrane ^{15}N chemical shifts indicate that most dimers and tetramers are oriented parallel to the membrane surface, but at high concentrations (P/L = 1:8), a small population with non-parallel orientation is also present, indicating that the tetramers are disordered.

Human defensins are cationic disulfide-bonded AMPs that are an essential component of the innate immune system. ^{19}F CODEX experiments were used to investigate the oligomeric structure of the human neutrophil peptide 1 (HNP-1) in DMPC/DMPG bilayers[92]. A 4F-Phg$_4$ labeled peptide yielded a CODEX equilibrium value of 0.66, indicating that the protein is partly dimerized. Several structural models of this basket-shaped HNP-1 dimer in the membrane are possible, differing in their membrane insertion depths, orientation in the membrane, and the positions of the four Arg sidechains from the membrane surface. Combining ^{13}C-^{31}P REDOR of ^{13}C-labeled Arg and lipid phosphate headgroups and membrane topology information obtained from lipid-protein ^1H spin diffusion data, Hong and coworkers found that HNP-1 adopts a dimer pore structure in which the polar top of the peptide faces an aqueous pore whereas the hydrophobic bottom faces the lipids. Among the four Arg residues, R25 forms a hydrogen-bonded guanidinium-phosphate complex to stabilize the structure.

While cationic AMPs disrupt microbial membranes for their action, cationic CPPs preserve the membrane integrity while carrying biological cargos into the cell. Understanding the mechanism of this membrane crossing is of both fundamental interest and practical interest in utilizing these peptides as drug-delivery agents. ^{19}F CODEX data of a CPP, penetratin, in DMPC/DMPG bilayers showed a trimeric assembly of three β-strands[93]. The measured F-F distance of 6 Å and 10 Å support antiparallel packing of these β-strands.

3.4.3 Viral Fusion Proteins—The TM domain of viral fusion proteins is important for fusing the viral and cell membranes, but its structural details are not well understood because of the hydrophobic nature of these peptides. ^{19}F CODEX of HIV-1 and parainfluenza virus 5 (PIV5) fusion proteins have provided information about the oligomeric structure of these α-helical peptides. Biophysical studies of gp41 in different membrane-mimetic environments had previously led to discrepant structural models in the literature. Using ^{19}F CODEX, Hong and coworkers showed that the gp41 MPER-TMD peptide forms trimeric helical bundles in virus-mimetic lipid bilayers (Fig. 9F)[49]. The intermolecular F-F distances between 5F-Trp residues in the MPER (W680 and W678) and between 4F-F699

in the TMD range from 11 to 12 Å. These CODEX data, together with membrane insertion data and REDOR distances, constrained a helix-turn-helix structure for each protomer of the trimer. In this assembly, the MPER helix lies on the membrane surface whereas the TMD spans the membrane.

[19]F CODEX experiments were also applied to the TM peptide of the PIV5 fusion protein F to determine its membrane-bound structure[94]. By placing 4F-Phe residues at three positions of the helix (L493F, L500F, and L504F) and measuring the CODEX decays, Hong and coworkers found interhelical distances of 8.2 to 10.5 Å. Together with crosslinking data, these distances constrained the interhelical packing of the helical bundle, and suggest that the leucine-rich central segment of this TM peptide is the trimerization core of the protein.

3.4.4 Cholesterol Clusters in Lipid Membranes—[19]F CODEX experiments are instrumental for proving the existence of small cholesterol clusters in lipid bilayers. Using isooctyl-tail fluorinated cholesterol, F_7-cholesterol, and a 2D extension of the ^{19}F CODEX experiment, Hong and coworkers found that cholesterol associates into dimers and tetramers in lipid bilayers[79]. Due to the presence of two CF_3 groups and a CF group with different chemical shifts, 2D CODEX was necessary to distinguish intermolecular anisotropic spin exchange from intramolecular isotropic exchange. The latter is manifested as cross peaks between CF_3 and CF peaks, whereas the former is manifested as decay of the diagonal intensities between the 2D CODEX S_0 and S spectra. [19]F spectra measured on a 17% and 44% cholesterol membrane showed two CF_3 chemical shifts. The major component's diagonal peak exhibited an equilibrium S/S_0 value of 0.23 in the 2D CODEX spectra, whereas the minor component, present only at high cholesterol concentration, showed an equilibrium value of 0.12. Since each cholesterol contains two CF_3 groups, these values indicate cholesterol dimers and tetramers, respectively. Together with ^{13}C CODEX data and MD simulations, these results led to experimentally constrained structures of small cholesterol clusters, and suggest that dimers are the basic structural unit of cholesterol in lipid bilayers under a wide range of biologically relevant conditions.

3.5. [19]F-[19]F Distance Measurements in Oriented Membranes

While MAS experiments account for the majority of distance measurement techniques in solid-state NMR, static ^{19}F NMR has also been explored for distance measurement. Ulrich and coworkers incorporated two fluorine labels into membrane peptides and used a Carr-Purcell-Meiboom-Gill (CPMG) experiment to measure well resolved [19]F-^{19}F dipolar splittings in static ^{19}F spectra of the oriented peptide[95]. By placing two rigid 4F-Phg labels in the antimicrobial peptide PGLa and aligning it in DMPC bilayers, they obtained distance-dependent [19]F –[19]F dipolar splittings. When the two 4F-Phg labels are separated by four and seven residues, they observed splittings of 363 Hz and 79 Hz, respectively, which correspond to F-F distances of 6.6 and 11.0 Å. Thus, if high membrane orientational order can be achieved, this static ^{19}F NMR is a simple and effective approach for measuring distances.

3.6 ^{19}F-^{19}F Homonuclear Dipolar Recoupling Techniques

At MAS frequencies above ~40 kHz, spin diffusion is no longer effective for polarization transfer, thus calling for homonuclear recoupling approaches for measuring ^{19}F-^{19}F distances. RFDR is one of the simplest homonuclear dipolar recoupling sequences[25,96], with only one 180° pulse per rotor period, and has been well explored for ^{19}F NMR. McDermott and coworkers first demonstrated this ^{19}F RFDR approach under 12–13 kHz MAS on a 400 MHz spectrometer (9.4 T)[97]. Fluorinated small molecules were synthesized with known distances and geometries to study the effects of internuclear distances and CSA tensor orientations on ^{19}F spin exchange. They measured significant ^{19}F spin exchange for distances up to ~12 Å using mixing times up to 35 ms. The CSA tensor orientation had significant effects on the magnetization exchange. But a distance precision of 1 Å was still achievable for shorter distances and 2 Å for longer distances.

Schmidt-Rohr and coworkers employed 2D ^{19}F-^{19}F RFDR experiments under fast MAS to investigate the perfluorinated polymer nafion[98]. Using 30 kHz MAS at 9.4 T, these authors obtained high-sensitivity 2D ^{19}F-^{19}F RFDR spectra of the polymer, from which they assigned the O, S and C-bonded CF_3, CF_2, and CF groups. The study was simplified by the lack of hydrogens in the polymer, which allowed the ^{1}H channel to be tuned to fluorine without the need for ^{1}H pulses. Fast MAS is highly beneficial for suppressing the CSA spinning sidebands.

Hong and coworkers investigated the effects of MAS frequencies, rf pulse duty cycle, ^{19}F CSA tensor orientations, and multi-spin effects on ^{19}F RFDR spin exchange[99]. Under 25 kHz MAS, RFDR polarization transfer rates were found to be two orders of magnitude faster compared to ^{19}F spin diffusion. The RFDR buildup time constants were several milliseconds for distances of 3 – 10 Å, whereas the corresponding spin diffusion buildup time constants are several hundreds of milliseconds. However, relaxation during the RFDR mixing period is also faster compared to T_1 relaxation during the spin diffusion mixing period. Therefore the relative rates of cross-peak buildup and relaxation decay should be examined to ascertain which technique has higher overall sensitivity. Under very fast MAS, relaxation during RFDR is sufficiently slowed down that RFDR outperforms spin diffusion for ^{19}F-^{19}F distance measurement. At MAS frequencies of 20–40 kHz, the ^{19}F 180° pulse occupies 15–30% of the rotation period using typical rf field strengths. Under these conditions, cross-peak buildup rates depend on both the ^{19}F CSA tensor orientation and the inter-fluorine distance. Above 40 kHz MAS, numerical simulations showed that the cross-peak buildup rates have a much smaller dependence on the CSA tensor orientation, thus allowing distances to be extracted more accurately. Fast MAS also reduced the ^{19}F relaxation loss in the absence of ^{1}H decoupling. These advantages allow ^{19}F-^{19}F distances up to ~1 nm to be measured with a precision better than 0.5 Å. Numerical simulations indicate that δ-pulse RFDR at MAS frequencies of ~25 kHz encodes both distance and tensor orientation, whereas finite-pulse RFDR (fpRFDR)[100] at the MAS frequency of 60 kHz yields primarily distances, thus simplifying the analysis. These conclusions were similarly reached by Polenova and coworkers, who examined the effects of multi-spin ^{19}F-^{19}F dipolar coupling and phase cycling on the performance of ^{19}F RFDR under 60 – 111 kHz MAS[101,102]. Using fluorinated aromatic compounds with defined distances,

these authors found that fpRFDR efficiently transfers polarization without requiring large chemical shift differences. Application of this ^{19}F RFDR experiment to the HIV-1 capsid protein[76] at 40 and 60 kHz MAS yielded cross peaks for fluorines separated by 9–23 Å, demonstrating the efficiency of ^{19}F RFDR spin exchange for distance measurement.

4. ^{1}H-^{1}H Distance Measurements Under Fast MAS

As the most abundant as well as the highest-γ stable spin-1/2 nucleus in organic and biological molecules, ^{1}H has long been the most sensitive nuclear spin for NMR. Its high γ also makes ^{1}H-^{1}H dipolar coupling a potential long-distances probe. However, ^{1}H NMR of solids have long been hampered by the severe line broadening caused by the extensive ^{1}H-^{1}H dipolar network. In the last decade, two technological advances have largely overcome this barrier to distance measurement. The first advance is to reduce the proton density of biomolecules by perdeuteration followed by back-exchange in protonated solvents[103,104], and the second advance is to spin samples at very fast MAS frequencies of ~100 kHz[105–107]. These advances have led to the introduction of pulse sequences tailored to ^{1}H-^{1}H distance measurements, which are often implemented with high-sensitivity ^{1}H detection in high-dimensional correlation experiments.

4.1. ^{1}H-^{1}H Distance Measurement Techniques

The simplest approach for measuring qualitative ^{1}H-^{1}H distances in solid-state NMR is Proton Spin Diffusion (PSD), as no rf pulses are applied during the mixing time (Fig. 10A). However, the spin diffusion mechanism is rapidly attenuated with increasing MAS frequencies. Thus, ^{1}H-^{1}H recoupling is necessary under the fast MAS condition where most high-resolution ^{1}H spectra are measured. Recently, several ^{1}H homonuclear recoupling techniques tailored to fast MAS have been examined or introduced for distance measurements[108–111]. These include fpRFDR, DREAM, SERP, AM-MIRROR, and BASS-SD.

The RFDR experiment[25,100] (Fig. 10B), uses rotor-synchronized 180° pulses to induce longitudinal magnetization transfer. With only one pulse per rotor period, this experiment has a relatively modest rf demand, and can be implemented even at fast MAS frequencies of ~100 kHz. Under fast MAS, the finite-pulse RFDR recoupling mechanism dominates[100]. ^{1}H-^{1}H distance measurements were first demonstrated by Zilm and Rienstra on model proteins ubiquitin[104] and GB1[112] that were CDN-labelled and back-exchange with H_2O to install amide protons. Correlation with ^{15}N and ^{13}C chemical shifts in 2D and 3D experiments resolved the resonances. In the initial demonstrations of this approach, MAS rates of 20 kHz and 39 kHz were used for ubiquitin and GB1, respectively. For GB1, 517 ^{1}H-^{1}H distance restraints up to 5.5 Å were measured and allowed *de novo* structure calculation, giving good agreement with the crystal structure[112]. Differences mainly lie in the sidechains, for which few constraints were available since only exchangeable H^N and H^O protons were measured in the perdeuterated protein. Reif, Linser and coworkers proposed 3D and 4D ^{15}N-resolved ^{1}H-^{1}H RFDR experiments and demonstrated them on perdeuterated and 25% back-exchanged α-spectrin SH3[113,114]. The sparse ^{1}H system allowed the measurement of distances up to 13 Å between amide H^N and sidechain methyl

protons even at a moderate MAS frequency of 20 and 24 kHz. When the perdeuterated protein was 100% back-exchanged with protons, then spinning to 55 kHz was necessary to give well-resolved ^{1}H spectra. When even faster MAS rates of 100 kHz are used for protonated proteins, RFDR still performs well, giving ^{1}H-^{1}H distance restraints of up to 5.5 Å in GB1 and in a bacteriophage coat protein,[115].

Although RFDR is simple to implement, its efficiency decreases with increasing MAS rates. Moreover, at ultrafast MAS, high RF field strengths close to 100 kHz become necessary to fit the 180° pulse into each rotor period. Meier and coworkers employed the DREAM (Dipolar Recoupling Enhanced by Amplitude Modulation) experiment (Fig. 10C)[116], originally developed for ^{13}C NMR, to bypass these limitations. DREAM recouples homonuclear dipolar interactions using an adiabatic pulse whose field strength is centered at the Homonuclear Rotary Resonance (HORROR) condition of $\omega_1=\omega_r/2$. Because of its double-quantum nature, the sign of DREAM cross-peaks alternates between positive and negative, depending on whether a ^{1}H-^{1}H correlation results from direct or relayed dipolar transfer. The DREAM recoupling method was incorporated into a 4D ^{1}H-^{13}C resolved HSQC-DREAM-HSQC experiment to measure ^{1}H-^{1}H correlations in methyl labelled ubiquitin. This DREAM experiment was first employed at 55 kHz MAS[117] and subsequently at 100 kHz MAS[118]. In the latter study, distances up to 7 Å were measured using mixing times of 8 ms.

BASS-SD (Band Selective Spectral Spin-Diffusion)[119] is a selective zero-quantum recoupling experiment in which a weak spin-lock pulse is applied to achieve selective polarization transfer only within the H^N band, the H^α band, or the methyl proton band (Fig. 10D). Using protonated GB1, Agarwal and coworkers showed that BASS-SD selectively transferred magnetization between like protons that are 6 Å apart under 111 kHz MAS. Compared to RFDR, the BASS-SD yields higher signal sensitivity and less rf demand. However, the distance constraints are more qualitative, and the method is limited to short mixing times due to $T_{1\rho}$ relaxation.

Other selective ^{1}H-^{1}H recoupling techniques for fast MAS were recently introduced by Agarwal and coworkers. The SERP (Selective Recoupling of Protons) experiment[124] uses phase-modulated pulses to generate double-quantum dipolar Hamiltonians, and is sensitive to ^{1}H-^{1}H distances up to 5 Å in fully protonated molecules (Fig. 10E). Quantitative dipolar oscillations are observed for short distances of ~3 Å[120], as shown on thymol at 68 kHz MAS[125]. SPR (Selective Phase-optimized Recoupling) is similar to SERP and was recently introduced for MAS rates higher than 150 kHz[122]. ^{1}H-^{1}H correlations for distances over 11 Å were observed in the model compound pioglitazone hydrochloride.

The reverse AM-MIRROR (Amplitude Modulated Mixed Rotational and Rotary Resonance) experiment was introduced by Ernst and coworkers to achieve chemical-shift compensated broadband ^{1}H spin diffusion under fast MAS[126]. Here the ^{1}H channel has the same simple pair of 90° pulses as in PSD, but additionally a weak adiabatic pulse is applied on the heteronuclear channel (Fig. 10F). Compared to BASS-SD, AM-MIRROR avoids severe signal loss during the spin-lock pulse. The method was demonstrated on ubiquitin, and long distances of up to 10 Å were measured with a mixing time of 20 ms under 100 kHz MAS.

Since the AM-MIRROR recoupling field strength is independent of the MAS frequency, the technique does not require high rf amplitudes under fast MAS.

4.2. Applications of Long-Range ^{1}H Distance Measurements to Structural Biology

These ^{1}H-^{1}H distance techniques have been increasingly applied to large, heterogeneous, and insoluble biomolecules under fast MAS frequencies of 60–150 kHz[127]. These systems include viral proteins, macromolecular assemblies, amyloid fibrils, membrane-bound proteins, and drug formulations[128–133]. Here, we highlight a few studies where high-sensitivity ^{1}H-detected measurements of ^{1}H-^{1}H distances provided crucial structural restraints for these biomolecules.

4.2.1 Viral Proteins—Pintacuda and co-workers solved the *de novo* structure of the 14 kDa *Acinetobacter* phage 205 coat protein (AP205CP) using ^{1}H-detected NMR (Fig. 11A)[115]. AP205CP is a dimeric protein that constitutes the basic subunit of the icosahedral capsid of the phage. Even with full protonation, sedimented microcrystals of AP205CP yielded narrow ^{1}H linewidths of 0.15–0.20 ppm when spun under 100 kHz on a 1 GHz NMR spectrometer. The presence of sidechain protons in addition to amide H^N allowed the measurement of ^{1}H-^{1}H correlations using 3D hNHH and hCHH experiments and RFDR mixing. In total, the authors obtained 410 intramolecular distances and 104 intermolecular distances up to 5.5 Å, which constrained the structure of this dimeric protein. The same approach was also applied to other viral proteins, including the hepatitis B virus nucleocapsid core and envelope proteins[134,135], and the hepatitis C virus nonstructural protein 4B bound to lipid bilayers[136].

Using ^{1}H-detected fast MAS NMR, Griffin and coworkers determined the structure of the S31N mutant of the influenza AM2$_{18–60}$ protein in diphytanoylphosphocholine bilayers[137]. To obtain interhelical distance constraints, the authors conducted ^{15}N-^{13}C TEDOR experiments on mixed ^{15}N and ^{13}C labeled samples as well as ^{1}H-^{1}H RFDR experiments under 60 kHz MAS. The latter involved ^{1}H exchanged, ^{15}N labeled and ILV-methyl ^{13}C-labeled proteins. A 4D HCHHCH experiment with 8 ms fpRFDR and a 3D hNHH experiment with 3.3 ms fpRFDR were conducted to give methyl-methyl and H^N-H^N distance restraints. The authors obtained nine inter-helical contacts, which constrained the sidechain conformations of the functionally important His37 and Trp41 residues in this proton channel.

Lange and co-workers investigated the oligomeric structure of gp17.1[138,139], a protein component of the extensive tail tubes from the SPP1 virus[140]. To probe the dimerization interface, the authors mixed ^{1}H-exchanged ^{2}H, ^{15}N-gp17.1 with equal amounts of isoleucine methyl-labeled (Ile-^{1}H$_\delta$–^{13}C$_\delta$)-(^{2}H, ^{12}C)-gp17.1. The latter was obtained from α-ketobutyrate-4-^{13}C-3,3-d2 precursors[141]. ^{1}H-detected 3D HNhH spectra with 10 ms RFDR mixing provided seven unambiguous interchain contacts between methyl and amide H^N protons (Fig. 11B). This result was subsequently corroborated by mutagenesis data, where deletion of the identified residues prevented oligomerization. Here the extensive deuteration and site-specific labeling of the protein obviated the need for very fast MAS, and 40 kHz MAS and a 900 MHz magnet sufficed to give well-resolved hNH and hCH spectra.

4.2.2 Membrane Proteins—For large membrane proteins, sparse ^{1}H labeling is an effective approach for distance measurements, by reducing both spectral congestion and ^{1}H linewidths. Weingarth and coworkers introduced amino-acid specific ^{1}H labeling into a perdeuterated protein to measure long-range interactions between non-exchangeable aliphatic protons[142]. This *proton cloud* strategy consists of adding ^{13}C, ^{15}N-labeled and protonated amino acids to *E. coli* minimal media prepared in D_2O (Fig. 12A). This strategy was first demonstrated on Val, Leu-labeled ubiquitin under 60 kHz MAS on an 800 MHz spectrometer. Distances up to 6 Å between Val and Leu sidechain protons were observed with 75 ms ^{1}H spin diffusion (Fig. 12A). Since proton clouds do not require re-protonation at exchangeable sites, which can be difficult to achieve for membrane-bound proteins, this approach is particularly useful for studying membrane proteins. This was demonstrated on BamA, a 52 kDa β-barrel assembly (Fig 12B)[142].

Oschkinat and coworkers determined the structure of the 14-stranded 34 kDa β-barrel formed by the outer membrane protein G (OmpG)[143]. Using 3D hNHH and hNhhNH experiments with 2 ms RFDR mixing under 60 kHz MAS, the authors measured 102 H^N-H^N distances. The protein was CDN-labeled followed by ^{1}H exchange and was bound to *E. coli* lipid extracts (Fig. 12C). These H^N-H^N distances helped to restrain a high-resolution structure of the protein using the ARIA[145] and CNS[146] software.

Andreas and coworkers determined the structures of another β-barrel membrane protein, AlkL, using fully protonated samples and ^{1}H-detected NMR. The 8-stranded protein is a member of the OmpW family and imports hydrophobic molecules such as alkanes and terpenoids across the outer membrane of Gram-negative bacteria. These authors investigated the AlkL structure in both DMPC bilayers and octyl glucoside micelles using solid-state and solution NMR, respectively[144] (Fig. 12D). For the bilayer-bound protein, [1]H-^{1}H distance restraints were measured using 4D HNNH experiments with fpRFDR and BASS-SD mixing schemes. These experiments yielded 769 [1]H-^{1}H restraints, many of which constrain the packing of the β-strands in the membrane. Full protonation of the protein is crucial for obtaining sidechain distances. The bilayer-bound structure shows a narrow TM pore that suggests that substrates are not transported in a straight path. Instead, the presence of several openings near the membrane surface suggests a dynamic lateral release model. This was supported by MD simulations and NMR relaxation data and chemical shift perturbations in the presence of the substrate octane and carvone.

Structural and mechanistic studies of membrane proteins can benefit from NMR spectral editing. Exchanging solvent-exposed NH groups with D_2O is a straightforward approach to render these residues invisible while keeping solvent-inaccessible residues in the TM domain visible from [1]H-detected experiments. This approach is especially well suited for examining the membrane topology of and water cavities in membrane proteins[147,148]. Conversely, water-exposed residues can be selectively detected by water magnetization transfer experiments in protonated solvents[149]. The water magnetization can be selected using a [1]H T_2 filter, then transferred to the protein[104,150]. Water contact with proteins has been studied under 55–60 kHz MAS for the anion channel hVDAC[151], AlkL[144], GlpG protease[152], and the potassium channel KcsA[153]. In the case of KcsA, residue-specific correlations between the protein and ordered water molecules were detected in a 2D HhN

experiment with 1.2 ms PSD. Weingarth and coworkers showed that these ordered water molecules play an important role in regulating channel gating[154]. Well-resolved ^{1}H chemical shifts are also informative for identifying structurally and functionally relevant hydrogen bonds in KcsA[154], the influenza M2 proton channel[155,156], human carbonic anhydrase II[157], nucleic acids[158], and amyloid fibrils[159].

4.2.3   Amyloid Fibrils—Fast MAS ^{1}H-detected NMR spectroscopy has also been used to investigate amyloid protein structure. Loquet, Habenstein and co-workers identified key molecular properties that modulate the aggregation of functional amyloids[160]. The authors determined the structure of the fungal amyloid protein, HELLF, based on [1]H-^{1}H distance restraints measured under 110 kHz MAS on a 1 GHz NMR spectrometer. The fibrils displayed a single molecular conformation featuring a rigid β-solenoid fold with a ^{1}H linewidth of 150–200 Hz. A total of 143 long-range intramolecular [1]H-^{1}H contacts were obtained from 3D hCHH, HhCH, and HhNH experiments with RFDR mixing. Intermolecular ^{1}H contacts were obtained using an HhNH experiment on an equimolar mixture of unlabeled and protonated HELLF mixed with perdeuterated and [1]H-exchanged ^{15}N-labeled HELLF (Fig. 13A). Interestingly, although HELLF shares a similar structure to the HET-s protein[161] and co-exists in the same fungus, *Podospora anserina*, these two prions do not cross-aggregate. After generating several HELLF mutants that exhibited the same three-dimensional fold but very different cross-aggregation propensities, the authors concluded that the overall protein fold is insufficient to induce prion strains but that crucial sidechain positions may be important for determining the cross-seeding propensity and prion specificity.

4.2.4   Protein-Ligand Complexes—The high spectral resolution provided by fast MAS and high magnetic fields brings new opportunities to investigate large enzymatic complexes. Recent studies have investigated the mechanisms[162], substrate-binding[163–165], and dynamics[166] of enzymes such as ATPases, peptidoglycan-crosslinking enzymes, and aminopeptidases. Linser and co-workers studied the structure and function of human carbonic anhydrase II (hCAII), a 29 kDa enzyme responsible for hydrating CO_2 to bicarbonate[167]. Using fully protonated ^{15}N, ^{13}C-labeled hCAII and 111 kHz MAS on an 800 MHz NMR, they conducted time-shared 3D Hh(N/C)H experiments with 1.53 ms ^{1}H RFDR mixing. These experiments yielded important [1]H-^{1}H sidechain restraints (Fig. 13B). In particular, the tautomeric structures and protonation states of the zinc-coordinating histidine residues, H94, H96 and H119, were observed in the [1]H-detected spectra. [15]N spin-lock relaxation dispersion experiments additionally showed that the active site is dynamic and is modulated by a water hydrogen-bonding network[157].

Fast MAS ^{1}H-detected NMR experiments have contributed to the studies of lipid-protein interactions. Although ^{1}H spin diffusion slows at fast MAS, NOE-mediated transfer from the lipid acyl chains to the protein remains appreciable[104]. Therefore, lipid-protein correlations can be measured with ^{1}H detection, as shown in an HhNH experiment for AlkL in phosphocholine membranes at 55 kHz MAS[151]. This [1]H-detected lipid-protein correlation technique was advantageous for investigating the mode of action of membrane-active antibiotics[168]. Complementarily, chemical shift perturbations in [1]H-detected spectra

allowed the identification of the binding sites of antibiotics[148,169]. For dynamic species such as phospholipids and disordered domains in membrane proteins, [1]H-detected 2D [13]C-^{1}H INEPT correlation spectra obtained at moderate MAS frequencies also provide useful structural information[170]. Finally, fast MAS allowed the investigations of protein-nucleic acid interactions through chemical shift perturbations in [1]H-detected correlation spectra[171,172] and through ^{31}P-detected NHHP experiments[173].

4.2.5 Integrative Approaches—The complexity of biomolecular machineries compels the integration of solid-state NMR spectroscopy with complementary techniques such as X-ray crystallography and cryo-EM[139,164,165,176]. Schanda and co-workers demonstrated an integrative NMR and cryo-EM approach for determining the three-dimensional structure of large biomolecular assemblies[174]. The central idea is to use secondary structure information from NMR and [1]H-^{1}H distance restraints from backbone amides and methyl groups to iteratively refine low-resolution cryoEM maps to high resolution. Using this integrative approach, these authors determined the structure and supramolecular assembly of TET2, a 468 kDa homo-dodecametric aminopeptidase, to better than 1 Å precision and accuracy. Intramolecular [1]H-^{1}H distance restraints of TET2 subunits were measured using time-shared 3D h(N/C)hh(N/C)H experiments with 5 ms ^{1}H RFDR mixing (Fig. 13C) under 55 kHz MAS. The resulting structure provided information about important loop regions of the protein that was not accessible from X-ray crystallography and that was important for understanding the enzyme activity.

4.2.6 Small Molecules and Material Sciences—Ultrafast MAS has not only been applied to biomolecular studies but has also opened new avenues of research in chemical, materials, and pharmaceutical sciences. Enhanced ^{1}H spectral resolution enables the characterization of pharmaceutical compounds[71,177,178] and organic compounds at natural abundance[71,130,179]. Su and coworkers employed [1]H-^{1}H RFDR experiments at 110 kHz MAS to investigate intermolecular interactions between active pharmaceutical ingredients and polymeric excipients[180]. These studies aid in the formulation of better amorphous solid dispersions to improve therapeutic efficacy. In materials science, fast MAS ^{1}H NMR is a powerful approach for characterizing heterogeneous catalysts and for tracking protons during chemical reactions. Wiegand and coworkers used 110 kHz MAS and 2D ^{1}H spin diffusion experiments to characterize the hydrogenation products of Frustrated Lewis Pairs compounds[181]. Wimperis and coworkers used 75 kHz MAS to explore the ^{1}H environment in silica and epoxy-silica materials and evaluate the hydration and structural integrity of the *in situ* immobilized biocatalysts with hCA II[182]. In biomaterials, Ramamoorthy and co-workers applied 110 kHz MAS to gain insight into bone structure[183]. These authors powdered bovine cortical bone samples into 0.75 mm rotors to investigate the molecular interactions between collagen and water molecules. Fast MAS rendered collagen backbone H[N] signals visible and resolved the sidechain ^{1}H signals. 2D ^{1}H fpRFDR experiments were used to show that water interactions with collagen backbone H[N] differ qualitatively from water interactions with sidechain protons.

NMR crystallography benefitted from fast MAS, as [1]H-^{1}H dipolar couplings and ^{1}H chemical shift anisotropy can now be measured in natural abundance organic

compounds[184,185]. Polenova and co-workers characterized the structure of posaconazole, an antifungal agent[175]. ^{1}H-^{1}H distance contacts were obtained from 3D ^{1}H-^{1}H-^{1}H DQSQ-RFDR experiments with 0.09–1.0 ms mixing. These spectra were measured under 111 kHz MAS on a 700 MHz NMR spectrometer (Fig. 13D). This approach yielded intra- and intermolecular ^{1}H restraints up to 6 Å, which defined the supramolecular packing of the compound.

5. ^{13}C and ^{15}N NMR for Long-Distance Measurements

5.1 ^{13}C-^{13}C Spin Diffusion Experiments

^{13}C spin diffusion NMR has long been the mainstay for measuring long-range distance restraints for structure characterization. These experiments are typically run in a 2D manner beginning with ^{1}H-^{13}C CP, followed by ^{13}C t_1 evolution, then storage of the ^{13}C magnetization along the *z*-axis to allow ^{13}C spin diffusion. This period can last hundreds of milliseconds to detect long-range correlations. Finally, the ^{13}C magnetization is returned to the transverse plane for detection. What distinguishes different spin diffusion techniques is the type of ^{1}H irradiation pulses during the ^{13}C mixing period. In the simplest ^{13}C spin diffusion experiment, PDSD[186], no ^{1}H irradiation is applied during the mixing period. This PDSD experiment is easy to set up, requires no optimization, and allows mixing times as long as several seconds to be used due to the lack of rf pulses.

However, even at moderate MAS frequencies of ~20 kHz, ^{13}C spin diffusion by PDSD is no longer efficient because of the diminishing zero-quantum overlap integral between the two carbons[187]. Therefore, many improved mixing sequences have been developed to increase the efficiency of ^{13}C magnetization transfer. ^{1}H irradiation at an rf field strength (ω_{1H}) that matches the MAS frequency ω_r with certain ratios can broaden the overlap integral, thus speeding up spin diffusion. The Dipolar-Assisted Rotary Resonance (DARR) technique uses the matching condition, $\omega_{1H} = \omega_r$, to give broadband and efficient spin diffusion[188,189]. The phase-alternated recoupling irradiation scheme (PARIS) alternates the phase of ^{1}H irradiation between +x and −x every half a rotor period or two rotor periods. Unlike DARR, the PARIS ^{1}H rf field strength does not need to fulfill any matching condition[190]. Therefore, weaker rf fields can be used, which are advantageous for fast MAS conditions where ^{1}H irradiation for hundreds of milliseconds can cause significant sample heating. At MAS frequencies of 30 kHz, PARIS was shown to have higher ^{13}C magnetization transfer efficiency than DARR and PDSD. PARIS is also less sensitive to rf field inhomogeneity, thus a larger proportion of the sample in the rotor experiences optimal ^{1}H-^{13}C recoupling. PARIS allows efficient aliphatic-aliphatic transfer but is not sufficiently broadband to promote spin diffusion from aliphatic carbons to aromatic or carbonyl carbons. PARIS-xy addresses this problem by using an orthogonal rf phase cycle during the recoupling period[191]. The second-order Hamiltonian among analogous nuclei generated by heteronuclear assistance irradiation (SHANGHAI) is another variant of these experiments. This experiment uses a super-cycled dipolar recoupling scheme to achieve efficient polarization transfer over large isotropic chemical shift differences and at high magnetic fields[192].

Combined R2$_n^v$ driven (CORD) spin diffusion is a broadband ^{1}H-^{13}C recoupling technique that promotes efficient spin diffusion over a range of MAS frequencies[74]. In the CORD experiment, ω_{1H} is equal to ω_r for one third of the mixing time but half the MAS frequency for two thirds of the time. Therefore, this experiment requires less rf power than DARR. Demonstrated on uniformly ^{13}C,^{15}N-labeled amino acids and the dynein light chain protein with mixing times up to 500 ms, the CORD experiment was found to be more broadband than PARIS-xy, while providing greater transfer efficiencies than the SHANGHAI experiment.

5.2 Applications of ^{13}C Spin Diffusion to Proteins

Since ^{13}C spin diffusion is an essential element in almost all biological solid-state NMR experiments, we only highlight a small number of its applications. Among amyloid proteins, the α-synuclein fibril that makes up the Lewy bodies and neurites in Parkinson's disease has been structurally determined using solid-state NMR[193]. This structure was challenging to solve because the protein is larger (14.5 kDa) than some of the well-studied amyloid peptides such as Aβ, and the amino acid sequence has low complexity. Using DARR mixing times of 50 ms to 500 ms on samples labeled with either 1,3-^{13}C glycerol or 2-^{13}C glycerol, Rienstra and coworkers measured 180 unambiguous and 80 ambiguous long-range ^{13}C-^{13}C distances. These correlations helped to constrain the novel Greek key motif for the fibril core. Of great utility in assigning these long-range correlations was a 3D ^{15}N-^{13}C-^{13}C experiment with 500 ms DARR mixing. The ^{15}N dimension provided spectral resolution to assign the many long-range contacts. These *in vitro* α-synuclein fibrils are pathogenic to neuronal cells, suggesting that they are relevant to the *in vivo* fibrils in Parkinson's disease.

The amyloid fibril formed by the peptide hormone glucagon presents a second case where ^{13}C spin diffusion was instrumental for structure determination. Glucagon functions in blood glucose homeostasis by raising the blood sugar level and is prescribed for treating severe hypoglycemia. However, at pharmaceutically relevant concentrations, glucagon aggregates rapidly from solution. Thus, it has to be formulated as a lyophilized powder, to be mixed with a diluent solution immediately before administration. Hong and coworkers solved the high-resolution structure of glucagon fibrils (Fig. 14A)[194]. All spectra show peak doubling in a 1:1 intensity ratio, indicating that the cross-β fibrils contain two coexisting β-strand conformations. ^{13}C CORD spin diffusion experiments with mixing times up to 500 ms gave numerous cross peaks between the N- and C-termini. These cross peaks disappear when the isotopically labeled monomers are diluted with unlabeled monomers. Therefore, these N- to C-contacts are intermolecular, indicating that the β-strands pack in an antiparallel fashion along the fibril axis. Additional ^{1}H-assisted ^{13}C-^{13}C correlation spectra (PULSAR) confirm this result (Fig. 14A).

The HIV-1 capsid that surrounds the viral RNA is made up of ~1,000 copies of the capsid protein. Polenova and coworkers determined a high-resolution structure of the CA in tubular assemblies by combining secondary structure information and distance restraints from solid-state NMR with low-resolution cryoEM maps and molecular dynamics simulations[195]. Using CORD mixing times of 25, 50, 200, and 500 ms on samples prepared with either 1,6-^{13}C-glucose or 2-^{13}C-glucose, they obtained 414 unambiguous inter-residue contacts.

Among these, 166 were medium-range and 219 were long-range in terms of amino acid sequence. These contacts were crucial for determining the high-resolution structure of the CA tubes.

5.3   Third-Spin Assisted Recoupling Experiments

Third-spin-assisted recoupling (TSAR) experiments[196,197] were developed by Griffin and coworkers to measure long-range distance restraints between low-γ nuclei. These experiments consist of spin lock of both ^{1}H and the heteronuclei at rf fields that avoid the Hartman-Hahn matching condition and rotary resonance conditions, while fulfilling zero- or double-quantum matching conditions. This class of experiments relies on second-order cross-terms between ^{1}H-A and ^{1}H-B dipolar couplings in the average Hamiltonian to achieve polarization transfer. Therefore, they differ from first-order recoupling experiments such as RFDR[96] or TEDOR[198,199], which rely on direct ^{13}C-^{13}C and ^{15}N-^{13}C dipolar couplings for polarization transfer. While the first-order average Hamiltonian for TSAR experiments averages to zero, the second-order average Hamiltonian contains trilinear terms of the form $H_zA^\pm B^\pm$, which drive polarization transfer.

The homonuclear TSAR experiment is superior to first-order homonuclear recoupling experiments by avoiding dipolar truncation, a phenomenon that masks the structurally informative long-range weak couplings by short-range strong couplings. Moreover, at high magnetic fields and high MAS frequencies, ^{13}C-^{13}C and ^{15}N-^{15}N spin diffusion in PDSD and DARR experiments becomes increasingly inefficient. In comparison, TSAR experiments continue to perform well under these high-field and fast MAS conditions. The first homonuclear TSAR experiment, called PAR (Proton Assisted Recoupling)[197], has been conducted at 20–65 kHz MAS at magnetic fields higher than 20 T[200]. PAR is also able to provide long-range ^{15}N-^{15}N correlations in proteins[201] despite the weakness of ^{15}N-^{15}N dipolar couplings. Sequential ^{15}N-^{15}N cross peaks help resonance assignment, particularly when combined with a ^{15}N-^{13}C ^{SPECIFIC}CP block to produce a 3D ^{15}N-^{15}N-^{13}C correlation spectrum[202]. Medium-range ^{15}N-^{15}N correlations obtained using the PAR experiment can help to identify α-helical secondary structure due to the relatively short distances between amide nitrogens in α-helices. Long-range ^{15}N-^{15}N contacts can help to identify the registry of antiparallel β-sheets. The first heteronuclear TSAR experiment is proton-assisted insensitive nuclei cross polarization (^{PAIN}CP)[196,203], which has also been widely applied for structure determination.

Improved variants of the PAR and ^{PAIN}CP experiments have also been introduced. One variant combines ^{13}C-^{13}C PAR and ^{15}N-^{13}C ^{PAIN}CP in one experiment by using simultaneous ^{1}H-^{13}C and ^{1}H-^{15}N CP at the beginning of the experiment[204,205]. Measuring these two spectra simultaneously gives nearly the same signal-to-noise ratio as measuring them in separate experiments. A careful choice of phase-cycling allows for the heteronuclear ^{13}C-^{15}N cross peaks obtained from ^{PAIN}CP to be negative, while the homonuclear ^{13}C-^{13}C cross peaks obtained from PAR to be positive. Furthermore, a z-filter during t_1 evolution on the ^{13}C channel allows the acquisition of indirect ^{13}C and ^{15}N dimensions with different spectral widths, which is important to fine tune these experiments given the very different chemical shift dispersion between ^{13}C and ^{15}N nuclei.

Recently, Hong and coworkers introduced pulsed variants of the TSAR experiments by replacing the continuous-wave (CW) spin lock on the low-γ channels with pulsed spin-lock. The homonuclear version of these Pulsed TSAR (P-TSAR) experiments is called pulsed proton assisted recoupling (PULSAR)[206] while the heteronuclear version is called proton enhanced rotor-echo short pulse irradiation cross-polarization ([PERSPIRATION]CP)[207]. These experiments reduce the rf duty cycle by 80–90% while producing similar polarization transfer as CW-TSAR experiments. When rf heating and probe hardware are the limiting factors in mixing times, these P-TSAR experiments allow for longer mixing times and thus longer-range contacts to be measured. P-TSAR experiments can be described with a simple analytical model[206] and are insensitive to rf field strengths. Therefore, they are simpler to optimize than the CW-TSAR experiments[208].

5.4 Applications of TSAR Experiments to Structural Biology

5.4.1 Amyloid Proteins—The peptide GNNQQNY is a fragment of the yeast prion protein Sup35p. Solid-state NMR spectra of this amyloid peptide show the presence of three conformers[209], whose sidechains are in molecular contact with each other based on PAR and [PAIN]CP spectra of mixed labeled samples measured with 10–14 ms mixing. These intermolecular contacts are attributed to distances of up to 7 Å, and indicate that each conformer makes up a parallel in-register β-sheet, and the different β-sheets associate via sidechain steric zippers. By mapping out which residues interact with each other, these authors identified the smallest building blocks that satisfy all the observed intermolecular correlations.

Tycko and coworkers determined a structure of Aβ$_{40}$ fibrils seeded from plaques obtained the brains of Alzheimer's disease patients[210]. Seeding allows isotopically enriched Aβ monomers to be used to replicate the brain Aβ conformation. Using a ^{13}C PAR experiment with 13 ms mixing, these authors measured many medium- and long-range ^{13}C-^{13}C correlations, which helped to constrain the three-dimensional structure of these AD brain-derived Aβ fibrils.

The 42-residue Aβ$_{42}$ peptide is more toxic than Aβ$_{40}$ and is more difficult to study because of its rapid fibrilization kinetics. Griffin, Riek, Meier, Böckmann and coworkers determined the structure of Aβ$_{42}$ fibrils using ^{13}C-^{13}C PAR and ^{15}N-^{13}C [PAIN]CP experiments in addition to other correlation experiments[211,212] (Fig. 14B). A 30 ms ^{15}N-^{13}C [PAIN]CP experiment gave cross peaks with a distance upper limit of ~12 Å, while ^{13}C PAR experiments with 10 and 15 ms mixing gave cross peaks with distance upper limits of 8.5 Å and 10 Å, respectively. The numerous long-range correlations constrained the structure of the fibril, showing a dimer of Aβ$_{42}$ each adopting a S-shaped fold. Intermolecular contacts between the two molecules were obtained by comparing the 20 ms ^{13}C PAR spectra measured on fully ^{13}C-labeled peptide and 30% ^{13}C-labeled monomers diluted in 70% unlabeled monomers. Intermolecular cross peaks decreased significantly in intensity upon dilution, whereas intramolecular cross peaks retained the same intensities. These distance restraints led to a high-resolution structure with a heavy-atom RMSD of 1.07 Å.

Determining the intermolecular packing and registry of β-strands is essential for amyloid protein structure determination. Mixed ^{13}C and ^{15}N labeled samples can be used to obtain

this information by comparing an intermolecular ^{PAIN}CP experiment with an intramolecular ^{SPECIFIC}CP-based N-Cα correlation experiment. If the same cross peaks are observed, then this is strong evidence that the fibrils have a parallel in-register packing. This approach was used to show that Aβ$_{40}$ fibrils bearing the E22 Osaka mutation[213], Aβ$_{42}$ fibrils[212], and human β-endorphin amyloids[214] all have parallel-in-register packing along the fibril axis.

The peptide Ac-IHVHLQI-CONH$_2$ self assembles into amyloid fibrils that coordinate Zn^{2+} to catalyze ester hydrolysis[215]. Hong and coworkers determined the structure of these Zn^{2+}-bound amyloid fibrils using solid-state NMR[216]. A 2D ^{13}C PAR experiment with 15 ms mixing yielded intermolecular contacts between V3 and I7 sidechains and between I1 and L5 sidechains, indicating that the hydrophobic faces of the β-sheets pack in an antiparallel fashion. In the final high-resolution structure, these intermolecular contacts correspond to distances of 8–10 Å.

Receptor-interacting protein kinases 1 (RIPK1) and 3 (RIPK3) are involved in neurodegenerative diseases, cancer, and immune defense. Amyloid fibrils made of RIPK1 and RIPK3 are important for signaling during necroptosis. McDermott and coworkers investigated the hetero-amyloid formed by alternating layers of RIPK1 and RIPK3[217]. TSAR experiments were used to determine the structure of the monomers as well as the packing of the monomers within the fibrils. ^{13}C PAR experiments with 12 and 15 ms mixing provided intermolecular contacts that established the parallel and alternating stacking of the monomers along the fibril axis. A 6 ms ^{PAIN}CP experiment helped to define the monomer bend and the registry of inter-residue contacts (Fig. 14C).

5.4.2   Nucleic Acids and Carbohydrates—Unambiguous assignment of Watson-Crick base pairs is a prerequisite for determining the three-dimensional structure of RNAs. Methods that directly probe the NH-N hydrogen bond are ideal for identifying such interactions, but have not been commonly used due to the difficulty of measuring ^{15}N-^{15}N correlations. ^{15}N-^{15}N PAR offers a promising avenue for measuring inter-nucleotide correlations because of the presence of a proton between two ^{15}N nuclei. Wang and coworkers identified G-C Watson-Crick base pairs in the dimerization initiation site of HIV-1 (DIS-HIV-1)[158]. This experiment begins with ^{1}H-^{13}C CP, followed by ^{13}C-^{15}N ^{SPECIFIC}CP to ^{15}N with chemical shifts greater than 140 ppm to select for the nitrogens involved in Watson-Crick base pairs. The ^{15}N chemical shift encoding was followed by 7 ms ^{15}N-^{15}N PAR mixing, after which the ^{15}N magnetization was transferred back to ^{1}H for high-sensitivity detection.

The carbohydrate structure and interactions in fungal cell walls are poorly understood. Using solid-state NMR, Wang and coworkers investigated the cell walls of intact *A. fumigatus* fungi that were grown in ^{13}C and ^{15}N-enriched media[218]. Using a 15 ms ^{13}C-^{13}C PAR experiment, they identified 23 long-range intermolecular cross peaks, which correspond to distances of 5–10 Å. This experiment helped to identify which carbohydrates are in close proximity to each other. Most of the contacts were seen between chitin and α-1,3-glucans, while some contacts occur between chitin-α-1,3-glucan complexes and β-glucans. Using a DNP sensitivity-enhanced ^{15}N-^{15}N PAR experiment, these authors observed correlations

between the three allomorphs of chitin. These results indicate that the three allomorphs coexist within each microfibril rather than being separated into different domains.

5.5 CHHC and NHHC Distance Techniques

Due to the high proton density and strong ^{1}H-^{1}H dipolar couplings in biological molecules, ^{1}H spin diffusion is highly efficient, and is not hampered by high magnetic fields and fast MAS frequencies in the same way that ^{13}C spin diffusion is. Thus, ^{1}H spin diffusion is attractive for distance measurements at moderate MAS frequencies. Baldus and coworkers introduced a CHHC technique for distance measurements using ^{1}H spin diffusion[219]. The experiment begins with ^{1}H-^{13}C CP and ^{13}C t_1 evolution to encode the ^{13}C chemical shift. The ^{13}C polarization is then transferred back to ^{1}H via a short CP step, after which ^{1}H spin diffusion is allowed to occur during a mixing period. Finally, a short CP back to ^{13}C allows detection. This experiment takes advantage of the spectral resolution afforded by ^{13}C while probing proton-proton distances. This experiment can be flexibly adapted to different heteronuclei to yield, for example, the NHHC experiment. When two different low-γ nuclei are used, the detection nucleus is typically the one with the higher γ in order to maximize the experimental sensitivity.

5.6 Application of the XHHY Experiments to Structural Biology

5.6.1. Membrane Proteins and Protein Assemblies—*Anabaena* sensory rhodopsin (ASR) is a microbial retinal-binding photoreceptor, and forms trimers of heptahelical monomers in lipid bilayers. Using 1,3 ^{13}C-labeled protein and a 2D CHHC experiment with 0.25 ms mixing, Ladizhansky and coworkers measured 14 interhelical ^{1}H-^{1}H distances with an upper bound of 5 Å in DMPC/DMPA membrane-bound protein[220] (Fig. 15A). Combined with interhelical ^{13}C-^{13}C correlations obtained from PDSD spectra, they determined the three-dimensional structure of this seven-TM helix protein to a backbone RMSD of 0.8 Å.

NHHC experiments can be readily applied to oligomeric membrane proteins to measure intermolecular distance restraints. Mixing ^{13}C-labeled monomers with ^{15}N-labeled monomers ensures that all ^{13}C-^{15}N cross peaks are intermolecular. This approach was used to determine the structure of the TM domain of the SARS-CoV-2 envelope protein[46]. The protein forms a cation-selective channel that is important for the virus's pathogenicity. By mixing ^{13}C-labeled and ^{15}N-labeled monomers at a 1:1 ratio and conducting NHHC experiments with mixing times of 0.5 ms and 1.0 ms, Hong and coworkers obtained 52 inter-helical contacts (Fig. 15B). Using a distance upper bound of 9.0 Å and 11.5 Å for the 0.5 and 1.0 ms mixing times, they calculated the structure of the five-helix bundle. The resulting closed-state structure shows a tight and narrow pore, stabilized by methyl-rich Ile, Val and Leu residues at the helix-helix interface and by three regularly spaced Phe residues.

Molecular assemblies such as molecular motors, bacterial secretion systems, and cytoskeletal filaments can be challenging to study structurally because of their large sizes and their structural disorder. Although cryoEM is ideal for obtaining the global fold of these molecular complexes, it often does not give sufficient resolution. Solid-state NMR is complementary to cryoEM in providing atomic-level structural information. Lange, Sgourakis and coworkers integrated cryoEM with solid-state NMR to obtain a

high-resolution structure of the Shigella type-III secretion needle[221]. Using a 7.7 Å resolution cryoEM structure and 996 solid-state NMR distance restraints obtained from PDSD experiments with 300 ms to 850 ms mixing, they determined the structure of this secretion needle to an RMSD of 0.4 Å. This structure was cross-validated with 96 unambiguous medium- and long-range ^{1}H-^{1}H restraints obtained from 0.25 ms NHHC and CHHC experiments and ambiguous restraints obtained from PDSD experiments. Less than 5% of these validation restraints were violated in the cross-validation step, supporting the accuracy of their high-resolution structure.

5.6.2 Amyloid Proteins—Identifying the mode of intermolecular packing is an important step in determining the high-resolution structure of amyloid fibrils. In an antiparallel β-sheet, Hα atoms on residues that are aligned along the hydrogen-bonded fibril axis are only 2.1 Å from each other. Thus, this intermolecular distance is even shorter than intramolecular Hα-Hα contacts. Using a CHHC experiment with a short ^{1}H-^{1}H mixing period of 0.2 ms, Tycko and coworkers showed that an antiparallel β-sheet can be unambiguously identified by strong ^{13}Cα–^{13}Cα intermolecular cross peaks[222]. Hong and coworkers successfully applied this approach to show that the peptide hormone glucagon forms an antiparallel hydrogen-bonded amyloid fibril with a well-defined registry[194]. Antiparallel β-sheets are rare among amyloid proteins, therefore the CHHC approach is complementary to the ^{15}N-^{13}C ^{PAIN}CP experiment for determining the structure of parallel hydrogen-bonded β-sheets.

The bacterium *Caulobacter Crescentus* produces bactofilin filaments made of the BacA protein, which are important for the stability and survival of the bacterium. Purified BacA polymerizes and forms single filaments, filament bundles, and two-dimensional semi-crystalline sheets. Lange and coworkers characterized these bactofilin filaments using electron microscopy and solid-state NMR[223]. They found that the rigid core of the filaments spans a conserved DUF583 domain, while the N- and C-termini are mobile. Chemical shifts indicate at least 10 β-strands in this domain, with no evidence for α-helical conformation. Mass-per-length measurements showed that each monomer spans about 2.7 nm along the fibril axis. This is inconsistent with a cross-β architecture, which would consist of integer multiples of monomers every 0.48 nm. This suggests a β-helical architecture, similar to that of the prion protein HET-s[161]. Using a homology model based on the crystal structure of the *Mycobacterium tuberculosis* acetyltransferase G1mU[224], Lange and coworkers these authors proposed that BacA adopts a β-helical structure in which the flat faces of the triangular assembly consist of β-strands, as identified from secondary chemical shifts. This model is supported by 8 long-range contacts measured in a 0.2 ms NHHC experiment and 12 long-range contacts measured in a 200 ms ^{13}C-^{13}C PDSD experiment. These long-range contacts provided strong evidence for the β-helical structure of these filaments.

Huntington's disease is a neurodegenerative disease caused by the formation of an extended polyQ sequence that is prone to aggregation. Van der Wel and coworkers investigated the structure of the amyloid fibrils formed by a huntingtin mutant with a 44-residue polyQ domain[225]. Chemical shifts and torsion angle data indicate a β-sheet conformation. Interestingly, peak doubling with a 1:1 intensity ratio was observed, indicating that two conformations of Gln coexist in these fibrils. NCACX and NCOCX spectra show that these

two forms exist in uniform segments, i.e. individual β-strands are made up of one form or the other. 2D ^{13}C-^{13}C PDSD experiments with 250 ms mixing on isotopically diluted samples show intermolecular cross peaks between the two conformers, suggesting that these fibrils contain a β-hairpin that places the two conformers in an antiparallel orientation along the fibril axis. 2D NHHC experiments with 0.25 ms mixing on mixed labeled proteins in which one quarter of the monomers were ^{13}C-labeled while three quarters were ^{15}N-labeled also showed intermolecular contacts between the two forms. Moreover, cross peaks involving sidechain ^{15}N are more intense than cross peaks involving backbone ^{15}N. This provides evidence for interdigitation of the sidechains to form an intermolecular steric zipper.

5.6.3   Nucleic Acids—RNA, DNA, and ribonucleoprotein proteins (RNPs) are ubiquitous in biology, but their structures are much less studied than proteins. Carlomagno and coworkers applied solid-state NMR to investigate the structure of a 26-residue Box C/D RNA from *Pyrococcus Furiosus* in complex with the L7Ae protein[226]. Due to the short ^1H-^1H distances associated with base pairs, the NHHC experiment is well suited for determining which bases are paired with each other. Using NHHC and CHHC experiments with mixing times of 0.1–0.2 ms, they obtained 27 unambiguous inter-nucleotide contacts with distances up to 5 Å. These proton-based distance restraints, together with ^{15}N-^{13}C distance restraints from TEDOR and ^{13}C-^{13}C restraints from PDSD experiments, helped to determine a three-dimensional structure of the RNA, giving a final structural ensemble with a heavy-atom RMSD of 0.9 Å.

Primases synthesize single-stranded DNA that can be extended by DNA polymerases. Allain and coworkers determined the high-resolution structure of the 115-residue helix bundle domain (HBD) of the pRN1 archaeal primase in complex with DNA 5'-CTGTGCTCA-3' and ATP, where the GTG nucleic acids make up the binding motif that interacts with the protein[227]. They found that the binding of two nucleotide triphosphates causes an allosteric change in the protein that makes DNA binding sequence-specific. Solid-state NMR CHHP and NHHP experiments provided intermolecular distance restraints from Lys and Arg residues on the protein to the DNA and ATP. Thus, the XHHY technique can be extended to other nuclei such as ^{31}P to obtain important distance restraints for structure investigation.

6.   Concluding Remarks and Outlook

This review shows the broad range of solid-state NMR techniques that are now available to biophysicists, chemists, and materials scientists to measure inter-atomic distances to ~2 nm. ^{19}F MAS NMR plays a prominent role in these long-distance measurements. It should be mentioned that ^{19}F NMR has also been widely used in the solution state to probe structure, dynamics, and ligand binding[228–231]. These nanometer distances are especially valuable for revealing the molecular structures of partially disordered biomolecular assemblies, including membrane-bound proteins, amyloid proteins, protein-protein complexes, protein-nucleic acid complexes, and carbohydrates in cell walls. To harvest the full power of these distance NMR techniques, one should combine multinuclear detection, fast MAS, high magnetic fields, and multidimensional correlation. The technological barrier for producing ultrahigh

magnetic fields has been recently overcome with the commercialization of high-temperature superconducting magnets at field strengths above 28 Tesla. Therefore, we envision that the next step in the widespread application of these distance NMR experiments is the development of more versatile and powerful NMR probes. These probes should be able to simultaneously tunable to four or five nuclear spins, including ^{1}H, ^{19}F, ^{13}C, ^{15}N, and ^{31}P. By illuminating the 1–2 nm distance range, which used to fall in the gap between the detection range of traditional NMR experiments and the detection range of other techniques such as paramagnetic relaxation enhancement NMR, electron paramagnetic resonance and fluorescence spectroscopy, these long-distance solid-state NMR techniques promise to make unique and significant contributions to biophysical chemistry.

Acknowledgements

Biographies

Alexander A. Shcherbakov is a Ph.D. candidate in the laboratory of Professor Mei Hong at the Massachusetts Institute of Technology (MIT). He received his B.S. degree with honors in Biochemistry and Chemistry and a minor in Mathematics at the University of Washington in Seattle. There he worked in the laboratory of Professor Niels Andersen studying the thermodynamics and kinetics of β-sheet peptide folding using solution NMR and circular dichroism. As a graduate student, Alexander developed fast MAS ^{19}F solid-state NMR techniques for rapid and high-sensitivity measurement of nanometer-length inter-atomic distances. He applied these techniques to the structure determination of several membrane proteins, including influenza B M2, SARS CoV-2 E, and the *E. coli.* multidrug-resistance protein EmrE.

João Medeiros-Silva studied biochemistry at NOVA University Lisbon and obtained his Ph.D. *cum laude* in Molecular Life Sciences from Utrecht University. There he investigated the structure and dynamics of potassium channels, antibiotic peptides, and protein-lipid interactions in the laboratory of Professor Markus Weingarth. In 2020 he joined the Hong laboratory at MIT as a Rubicon Postdoctoral Fellow, where he employs advanced solid-state NMR techniques to investigate the structure and biophysics of SARS-CoV-2 membrane proteins and other systems in their native membrane environment.

Nhi Tran received her Ph.D. in Physical Chemistry at the University of Florida in Gainesville under the supervision of Professor Joanna Long. Her research there centered on the application of solid-state NMR and dynamic nuclear polarization to characterize the structure and mechanism of pulmonary surfactant peptides and the investigation of lipid membrane dynamics. As a postdoctoral associate in the group of Professor Mei Hong, Nhi applied ^{19}F solid-state NMR techniques to investigate the structure and oligomeric assembly of membrane proteins involved in virus-cell membrane fusion. Currently, Nhi is a Process Engineer at Intel Corporation.

Martin D. Gelenter received his Ph.D. in Chemistry from MIT under the supervision of Professor Mei Hong. His research focused on studying the structure and aggregation of glucagon fibrils, characterizing the interaction of water with the influenza A M2 proton channel, and developing solid-state NMR techniques for studying the structure and dynamics of biomacromolecules. Currently he is a postdoctoral research fellow in the laboratory of Dr. Ad Bax at the National Institutes of Health. His research at NIH utilizes pressure-jump solution state NMR to study protein folding and misfolding.

Mei Hong is a Professor of Chemistry at the Massachusetts Institute of Technology. She obtained her Ph.D. from the University of California at Berkeley in 1996, where she developed and applied variable-angle spinning solid-state NMR techniques to study the conformation and dynamics of phospholipid membranes in the laboratory of Professor Alex Pines. After a one-year period as an NIH postdoctoral fellow in the laboratory of Bob Griffin at MIT, she went to the University of Massachusetts at Amherst and developed selective and extensive isotopic labeling strategies and multidimensional MAS NMR methods to achieve protein resonance assignment. She established her own laboratory at Iowa State University in 1999, became a full professor in 2005, and held the first John D. Corbett Professorship before returning to MIT in 2014. The Hong group develops and applies solid-state NMR spectroscopy to elucidate the molecular structure, dynamics, and mechanism of action of membrane proteins and amyloid proteins important for human health, as well as the structure and dynamics of plant cell walls.

References

(1). Reif B; Ashbrook SE; Emsley L; Hong M, Solid-State NMR Spectroscopy. Nat. Rev. Methods Primers 2021, 1.

(2). McDermott AE, Structure and Dynamics of Membrane Proteins by Magic Angle Spinning Solid-State NMR. Annu. Rev. Biophys 2009, 38, 385–403. [PubMed: 19245337]

(3). Comellas G; Rienstra CM, Protein Structure Determination by Magic-Angle Spinning Solid-State NMR, and Insights into the Formation, Structure, and Stability of Amyloid Fibrils. Annu. Rev. Biophys 2013, 42, 515–536. [PubMed: 23527778]

(4). Mandala VS; Williams JK; Hong M, Structure and Dynamics of Membrane Proteins from Solid-State NMR. Ann. Rev. Biophys 2018, 47, 201–222. [PubMed: 29498890]

(5). Griffin R, Dipolar Recoupling in MAS Spectra of Biological Solids. Nature Struct. Biol 1998, 5, 508–512. [PubMed: 9665180]

(6). Russell RW; Fritz MP; Kraus J; Quinn CM; Polenova T; Gronenborn AM, Accuracy and Precision of Protein Structures Determined by Magic Angle Spinning NMR Spectroscopy: For Some 'with a Little Help from a Friend'. J. Biomol. NMR 2019, 73, 333–346. [PubMed: 30847635]

(7). Clore MG; Iwahara J, Theory, Practice, and Applications of Paramagnetic Relaxation Enhancement for the Characterization of Transient Low-Population States of Biological Macromolecules and Their Complexes. Chem. Rev 2009, 109, 4108–4139. [PubMed: 19522502]

(8). Sengupta I; Nadaud PS; Jaroniec CP, Protein Structure Determination with Paramagnetic Solid-State NMR Spectroscopy. Acc. Chem. Res 2013, 46, 2117–2126. [PubMed: 23464364]

(9). Clore MG, Practical Aspects of Paramagnetic Relaxation Enhancement in Biological Macromolecules; Qin PZ;Warncke K, Eds.; Academic Press, 2015; Vol. 564.

(10). Gullion T; Schaefer J, Rotational Echo Double Resonance NMR. J. Magn. Reson 1989, 81, 196–200.

(11). Pan Y; Gullion T; Schaefer J, Determination of C-N Internuclear Distances by Rotational-Echo Double-Resonance NMR of Solids. J. Magn. Reson 1990, 90, 330.

(12). Levitt MH, Symmetry in the Design of NMR Multiple-Pulse Sequences. J. Chem. Phys 2008, 128, 052205. [PubMed: 18266410]

(13). De Paëpe G, Dipolar Recoupling in Magic Angle Spinning Solid-State Nuclear Magnetic Resonance. Annu. Rev. Phys. Chem 2012, 63, 661–684. [PubMed: 22404583]

(14). Brinkmann A; Kentgens AP, Proton-Selective 17o-1H Distance Measurements in Fast Magic-Angle-Spinning Solid-State NMR Spectroscopy for the Determination of Hydrogen Bond Lengths. J. Am. Chem. Soc 2006, 128, 14758–14759. [PubMed: 17105257]

(15). Sinha N; Schmidt-Rohr K; Hong M, Compensation for Pulse Imperfections in Rotational-Echo Double-Resonance NMR by Composite Pulses and Exorcycle. J. Magn. Reson 2004, 168, 358–365. [PubMed: 15140448]

(16). Gullion T; Schaefer J, Elimination of Resonance Offset Effects in Rotational-Echo Double Resonance NMR. J. Magn. Reson 1991, 92, 439–442.

(17). Weldeghiorghis TK; Schaefer J, Compensating for Pulse Imperfections in REDOR. J. Magn. Reson 2003, 165, 230–236. [PubMed: 14643704]

(18). Bak M; Rasmussen T; Nielsen NC, Simpson: A General Simulation Program for Solid-State NMR Spectroscopy. J. Magn. Reson 2000, 147, 296–330. [PubMed: 11097821]

(19). Veshtort M; Griffin RG, Spinevolution: A Powerful Tool for the Simulation of Solid and Liquid State NMR Experiments. J. Magn. Reson 2006, 178, 248–282. [PubMed: 16338152]

(20). McDowell LM; Lee M; McKay RA; Anderson KS; Schaefer J, Intersubunit Communication in Tryptophan Synthase by Carbon-13 and Fluorine-19 REDOR NMR. Biochemistry 1996, 35, 3328–3334. [PubMed: 8605170]

(21). Graesser DT; Wylie BJ; Nieuwkoop AJ; Franks WT; Rienstra CM, Long-Range 19F-15N Distance Measurements in Highly-13C, 15N-Enriched Solid Proteins with 19F-Dephased REDOR Shift (Fresh) Spectroscopy. Magn. Reson. Chem 2007, 45, S129–S134. [PubMed: 18157807]

(22). Shcherbakov AA; Hong M, Rapid Measurement of Long-Range Distances in Proteins by Multidimensional 13C–19F REDOR NMR under Fast Magic-Angle Spinning. J. Biomol. NMR 2018, 71, 31–43. [PubMed: 29785460]

(23). Shcherbakov AA; Mandala VS; Hong M, High-Sensitivity Detection of Nanometer 1H–19F Distances for Protein Structure Determination by 1H-Detected Fast MAS NMR. J. Phys. Chem. B 2019, 123, 4387–4391. [PubMed: 31034230]

(24). Shcherbakov AA; Roos M; Kwon B; Hong M, Two-Dimensional (19)F-(13)C Correlation NMR for (19)F Resonance Assignment of Fluorinated Proteins. J. Biomol. NMR 2020, 74, 193–204. [PubMed: 32088840]

(25). Bennett AE; Griffin RG; Ok JH; Vega S, Chemical Shift Correlation Spectroscopy in Rotating Solids: Radio Frequency-Driven Dipolar Recoupling and Longitudinal Exchange. J. Chem. Phys 1992, 96, 8624–8627.

(26). Kim HW; Perez JA; Ferguson SJ; Campbell ID, The Specific Incorporation of Labelled Aromatic Amino Acids into Proteins through Growth of Bacteria in the Presence of Glyphosate. Application to Fluorotryptophan Labelling to the H(+)-Atpase of Escherichia Coli and NMR Studies. FEBS Lett. 1990, 272, 34–36. [PubMed: 2146161]

(27). Gullion T, Measuring 13C-2D Dipolar Couplings with a Universal REDOR Dephasing Curve. J. Magn. Reson 2000, 146, 220–222. [PubMed: 10968975]

(28). Wi S; Sinha N; Hong M, Long-Range ^{1}H-^{19}F Distance Measurement in Peptides by Solid-State NMR. J. Am. Chem. Soc 2004, 126, 12754–12755. [PubMed: 15469252]

(29). Hong M; Griffin RG, Resonance Assignment for Solid Peptides by Dipolar-Mediated 13C/15N Correlation Solid-State NMR. J. Am. Chem. Soc 1998, 120, 7113–7114.

(30). Rienstra CM; Tucker-Kellogg L; Jaroniec CP; Hohwy M; Reif B; McMahon MT; Tidor B; Lozano-Perez T; Griffin RG, De Novo Determination of Peptide Structure with Solid-State Magic-Angle Spinning NMR Spectroscopy. Proc. Natl. Acad. Sci. USA 2002, 99, 10260–10265. [PubMed: 12149447]

(31). Ghosh M; Rienstra CM, 1H-Detected REDOR with Fast Magic-Angle Spinning of a Deuterated Protein. J. Phys. Chem. B 2017, 121, 8503–8511. [PubMed: 28816462]

(32). Su Y; Li S; Hong M, Cationic Membrane Peptides: Atomic-Level Insight of Structure-Activity Relationships from Solid-State NMR. Amino Acids 2013, 44, 821–833. [PubMed: 23108593]

(33). Hong M; Su Y, Structure and Dynamics of Cationic Membrane Peptides and Proteins: Insights from Solid-State NMR. Protein Sci. 2011, 20, 641–655. [PubMed: 21344534]

(34). Toke O; Lee Maloy W; Kim SJ; Blazyk J; Schaefer J, Secondary Structure and Lipid Contact of a Peptide Antibiotic in Phospholipid Bilayers by REDOR. Biophys. J 2004, 87, 662–674. [PubMed: 15240500]

(35). Toke O; O'Connor RD; Weldeghiorghis TK; Maloy WL; Glaser RW; Ulrich AS; Schaefer J, Structure of (Kiagkia)3 Aggregates in Phospholipid Bilayers by Solid-State NMR. Biophys. J 2004, 87, 675–687. [PubMed: 15240501]

(36). Mani R; Tang M; Wu X; Buffy JJ; Waring AJ; Sherman MA; Hong M, Membrane-Bound Dimer Structure of a B-Hairpin Antimicrobial Peptide from Rotational-Echo Double-Resonance Solid-State NMR. Biochemistry 2006, 45, 8341–8349. [PubMed: 16819833]

(37). Cegelski L; Steuber D; Mehta AK; Kulp DW; Axelsen PH; Schaefer J, Conformational and Quantitative Characterization of Oritavancin–Peptidoglycan Complexes in Whole Cells of Staphylococcus Aureus by in Vivo 13C and 15N Labeling. J. Mol. Biol 2006, 357, 1253–1262. [PubMed: 16483598]

(38). Umegawa Y; Matsumori N; Oishi T; Murata M, Ergosterol Increases the Intermolecular Distance of Amphotericin B in the Membrane-Bound Assembly as Evidenced by Solid-State NMR. Biochemistry 2008, 47, 13463–13469. [PubMed: 19053254]

(39). Umegawa Y; Adachi T; Matsumori N; Murata M, Possible Conformation of Amphotericin B Dimer in Membrane-Bound Assembly as Deduced from Solid-State NMR. Bioorg. Med. Chem 2012, 20, 5699–5704. [PubMed: 22959766]

(40). Hong M, Oligomeric Structure, Dynamics, and Orientation of Membrane Proteins from Solid-State NMR. Structure 2006, 14, 1731–1740. [PubMed: 17161364]

(41). Hong M; DeGrado WF, Structural Basis for Proton Conduction and Inhibition by the Influenza M2 Protein. Protein Sci. 2012, 21, 1620–1633. [PubMed: 23001990]

(42). Pinto LH; Lamb RA, The M2 Proton Channels of Influenza A and B Viruses. J. Biol. Chem 2006, 281, 8997–9000. [PubMed: 16407184]

(43). Williams, Jonathan K; Zhang Y; Schmidt-Rohr K; Hong M, Ph-Dependent Conformation, Dynamics, and Aromatic Interaction of the Gating Tryptophan Residue of the Influenza M2 Proton Channel from Solid-State NMR. Biophys. J 2013, 104, 1698–1708. [PubMed: 23601317]

(44). Hu F; Luo W; Hong M, Mechanisms of Proton Conduction and Gating by Influenza M2 Proton Channels from Solid-State NMR. Science 2010, 330, 505–508. [PubMed: 20966251]

(45). Mandala VS; Loftis AR; Shcherbakov AA; Pentelute BL; Hong M, Atomic Structures of Closed and Open Influenza B M2 Proton Channel Reveal the Conduction Mechanism. Nat. Struct. Mol. Biol 2020, 27, 160–167. [PubMed: 32015551]

(46). Mandala VS; McKay MJ; Shcherbakov AA; Dregni AJ; Kolocouris A; Hong M, Structure and Drug Binding of the Sars-Cov-2 Envelope Protein Transmembrane Domain in Lipid Bilayers. Nat. Struct. Mol. Biol 2020, 27, 1202–1208. [PubMed: 33177698]

(47). Surya W; Li Y; Torres J, Structural Model of the Sars Coronavirus E Channel in Lmpg Micelles. Biochim. Biophys. Acta Biomembr 2018, 1860, 1309–1317. [PubMed: 29474890]

(48). Pervushin K; Tan E; Parthasarathy K; Lin X; Jiang FL; Yu D; Vararattanavech A; Soong TW; Liu DX; Torres J, Structure and Inhibition of the Sars Coronavirus Envelope Protein Ion Channel. PLoS Pathog. 2009, 5, e1000511. [PubMed: 19593379]

(49). Kwon B; Lee M; Waring AJ; Hong M, Oligomeric Structure and Three-Dimensional Fold of the Hiv Gp41 Membrane-Proximal External Region and Transmembrane Domain in Phospholipid Bilayers. J. Am. Chem. Soc 2018, 140, 8246–8259. [PubMed: 29888593]

(50). Chiliveri SC; Louis JM; Ghirlando R; Baber JL; Bax A, Tilted, Uninterrupted, Monomeric Hiv-1 Gp41 Transmembrane Helix from Residual Dipolar Couplings. J. Am. Chem. Soc 2018, 140, 34–37. [PubMed: 29277995]

(51). Dev J; Park D; Fu Q; Chen J; Ha HJ; Ghantous F; Herrmann T; Chang W; Liu Z; Frey G et al. , Structural Basis for Membrane Anchoring of Hiv-1 Envelope Spike. Science 2016, 353, 172–175. [PubMed: 27338706]

(52). Pan Y, 31P-19F Rotational-Echo, Double-Resonance Nuclear Magnetic Resonance Experiment on Fluoridated Hydroxyapatite. Solid State Nucl. Magn. Reson 1995, 5, 263–268. [PubMed: 9053117]

(53). Merritt ME; Sigurdsson ST; Drobny GP, Long-Range Distance Measurements to the Phosphodiester Backbone of Solid Nucleic Acids Using 31P–19F REDOR NMR. J. Am. Chem. Soc 1999, 121, 6070–6071.

(54). Cruse WBT; Salisbury SA; Brown T; Cosstick R; Eckstein F; Kennard O, Chiral Phosphorothioate Analogues of B-DNA: The Crystal Structure of Rp-D¦Gp(S)Cpgp(S)Cpgp(S)C¦. J. Mol. Biol 1986, 192, 891–905. [PubMed: 3108513]

(55). Olsen GL; Louie EA; Drobny GP; Sigurdsson ST, Determination of DNA Minor Groove Width in Distamycin-DNA Complexes by Solid-State NMR. Nucleic Acids Res. 2003, 31, 5084–5089. [PubMed: 12930959]

(56). Olsen GL; Edwards TE; Deka P; Varani G; Sigurdsson ST; Drobny GP, Monitoring Tat Peptide Binding to Tar Rna by Solid-State 31P–19F REDOR NMR. Nucleic Acids Res. 2005, 33, 3447–3454. [PubMed: 15961729]

(57). Huang W; Varani G; Drobny GP, 13C/15N–19F Intermolecular REDOR NMR Study of the Interaction of Tar Rna with Tat Peptides. J. Am. Chem. Soc 2010, 132, 17643–17645. [PubMed: 21105680]

(58). Jiang YL; McDowell LM; Poliks B; Studelska DR; Cao C; Potter GS; Schaefer J; Song F; Stivers JT, Recognition of an Unnatural Difluorophenyl Nucleotide by Uracil DNA Glycosylase. Biochemistry 2004, 43, 15429–15438. [PubMed: 15581354]

(59). Studelska DR; Klug CA; Beusen DD; McDowell LM; Schaefer J, Long-Range Distance Measurements of Protein Binding Sites by Rotational-Echo Double-Resonance NMR. J. Am. Chem. Soc 1996, 118, 5476–5477.

(60). Fowler DJ; Weis RM; Thompson LK, Kinase-Active Signaling Complexes of Bacterial Chemoreceptors Do Not Contain Proposed Receptor–Receptor Contacts Observed in Crystal Structures. Biochemistry 2010, 49, 1425–1434. [PubMed: 20088541]

(61). Elkins MR; Williams JK; Gelenter MD; Dai P; Kwon B; Sergeyev IV; Pentelute BL; Hong M, Cholesterol-Binding Site of the Influenza M2 Protein in Lipid Bilayers from Solid-State NMR. Proc. Natl. Acad. Sci. U. S. A 2017, 114, 12946. [PubMed: 29158386]

(62). Kwon B; Mandal T; Elkins MR; Oh Y; Cui Q; Hong M, Cholesterol Interaction with the Trimeric Hiv Fusion Protein Gp41 in Lipid Bilayers Investigated by Solid-State NMR Spectroscopy and Molecular Dynamics Simulations. J. Mol. Biol 2020, 432, 4705–4721. [PubMed: 32592698]

(63). Elkins MR; Sergeyev IV; Hong M, Determining Cholesterol Binding to Membrane Proteins by Cholesterol 13C Labeling in Yeast and Dynamic Nuclear Polarization NMR. J. Am. Chem. Soc 2018, 140, 15437–15449. [PubMed: 30338997]

(64). Souza CM; Schwabe TM; Pichler H; Ploier B; Leitner E; Guan XL; Wenk MR; Riezman I; Riezman H, A Stable Yeast Strain Efficiently Producing Cholesterol Instead of Ergosterol Is Functional for Tryptophan Uptake, but Not Weak Organic Acid Resistance. Metab. Eng 2011, 13, 555–569. [PubMed: 21741494]

(65). Shcherbakov AA; Hisao G; Mandala VS; Thomas NE; Soltani M; Salter EA; Davis JH; Henzler-Wildman KA; Hong M, Structure and Dynamics of the Drug-Bound Bacterial Transporter Emre in Lipid Bilayers. Nat. Commun 2021, 12. [PubMed: 33397888]

(66). Yang H; Staveness D; Ryckbosch SM; Axtman AD; Loy BA; Barnes AB; Pande VS; Schaefer J; Wender PA; Cegelski L, REDOR NMR Reveals Multiple Conformers for a Protein Kinase C Ligand in a Membrane Environment. ACS Cent. Sci 2018, 4, 89–96. [PubMed: 29392180]

(67). Loy BA; Lesser AB; Staveness D; Billingsley KL; Cegelski L; Wender PA, Toward a Biorelevant Structure of Protein Kinase C Bound Modulators: Design, Synthesis, and Evaluation of Labeled Bryostatin Analogues for Analysis with Rotational Echo Double Resonance NMR Spectroscopy. J. Am. Chem. Soc 2015, 137, 3678–3685. [PubMed: 25710634]

(68). Lu M; Wang M; Sergeyev IV; Quinn CM; Struppe J; Rosay M; Maas W; Gronenborn AM; Polenova T, 19F Dynamic Nuclear Polarization at Fast Magic Angle Spinning for NMR of Hiv-1 Capsid Protein Assemblies. J. Am. Chem. Soc 2019, 141, 5681–5691. [PubMed: 30871317]

(69). Lu X; Skomski D; Thompson KC; McNevin MJ; Xu W; Su Y, Three-Dimensional NMR Spectroscopy of Fluorinated Pharmaceutical Solids under Ultrafast Magic Angle Spinning. Anal. Chem 2019, 91, 6217–6224. [PubMed: 30990668]

(70). Inoue M; Sumii Y; Shibata N, Contribution of Organofluorine Compounds to Pharmaceuticals. ACS Omega 2020, 5, 10633–10640. [PubMed: 32455181]

(71). Lu X; Lu X; Tsutsumi Y; Huang C; Xu W; Byrn SR; Templeton AC; Buevich AV; Amoureux JP; Amoureux JPet al. , Molecular Packing of Pharmaceuticals Analyzed with Paramagnetic Relaxation Enhancement and Ultrafast Magic Angle Pinning NMR. Phys. Chem. Chem. Phys 2020, 22, 13160–13170. [PubMed: 32495810]

(72). Lu X; Huang C; Li M; Skomski D; Xu W; Yu L; Byrn SR; Templeton AC; Su Y, Molecular Mechanism of Crystalline-to-Amorphous Conversion of Pharmaceutical Solids from (19)F Magic Angle Spinning NMR. J. Phys. Chem. B 2020, 124, 5271–5283. [PubMed: 32378905]

(73). Lu X; Li M; Huang C; Lowinger MB; Xu W; Yu L; Byrn SR; Templeton AC; Su Y, Atomic-Level Drug Substance and Polymer Interaction in Posaconazole Amorphous Solid Dispersion from Solid-State NMR. Mol. Pharm 2020, 17, 2585–2598. [PubMed: 32401529]

(74). Hou G; Yan S; Trébosc J; Amoureux JP; Polenova T, Broadband Homonuclear Correlation Spectroscopy Driven by Combined R2(N)(V) Sequences under Fast Magic Angle Spinning for NMR Structural Analysis of Organic and Biological Solids. J. Magn. Reson 2013, 232, 18–30. [PubMed: 23685715]

(75). Roos M; Wang T; Shcherbakov AA; Hong M, Fast Magic-Angle-Spinning 19F Spin Exchange NMR for Determining Nanometer 19F–19F Distances in Proteins and Pharmaceutical Compounds. J. Phys. Chem. B 2018, 122, 2900–2911. [PubMed: 29486126]

(76). Wang M; Lu M; Fritz MP; Quinn CM; Byeon IL; Byeon CH; Struppe J; Maas W; Gronenborn AM; Polenova T, Fast Magic-Angle Spinning 19F NMR Spectroscopy of Hiv-1 Capsid Protein Assemblies. Angew. Chem. Int. Ed. Engl 2018, 57, 16375–16379. [PubMed: 30225969]

(77). Bayro MJ; Huber M; Ramachandran R; Davenport TC; Meier BH; Ernst M; Griffin RG, Dipolar Truncation in Magic-Angle Spinning NMR Recoupling Experiments. J. Chem. Phys 2009, 130, 114506–114506. [PubMed: 19317544]

(78). Roos M; Mandala VS; Hong M, Determination of Long-Range Distances by Fast Magic-Angle-Spinning Radiofrequency-Driven 19F–19F Dipolar Recoupling NMR. J. Phys. Chem. B 2018, 122, 9302–9313. [PubMed: 30211552]

(79). Elkins MR; Bandara A; Pantelopulos GA; Straub JE; Hong M; Gerling UIM; Salwiczek M; Cadicamo CD; Erdbrink H; Czekelius Cet al. , Direct Observation of Cholesterol Dimers and Tetramers in Lipid Bilayers. J. Phys. Chem. B 2021, 5, 819–830.

(80). deAzevedo ER; Bonagamba TJ; Hu W; Schmidt-Rohr K, Centerband-Only Detection of Exchange: Efficient Analysis of Dynamics in Solids by NMR. J. Am. Chem. Soc 1999, 121, 8411–8412.

(81). deAzevedo ER; Hu WG; Bonagamba TJ; Schmidt-Rohr K, Principles of Centerband-Only Detection of Exchange in Solid-State Nuclear Magnetic Resonance, and Extension to Four-Time Centerband-Only Detection of Exchange. J. Chem. Phys 2000, 112, 8988–9001.

(82). Luo W; Hong M, Determination of the Oligomeric Number and Intermolecular Distances of Membrane Protein Assemblies by Anisotropic 1H-Driven Spin Diffusion NMR Spectroscopy. J. Am. Chem. Soc 2006, 128, 7242–7251. [PubMed: 16734478]

(83). Buffy JJ; Waring AJ; Hong M, Determination of Peptide Oligomerization in Lipid Bilayers Using 19F Spin Diffusion NMR. J. Am. Chem. Soc 2005, 127, 4477–4483. [PubMed: 15783230]

(84). Luo W; Mani R; Hong M, Side-Chain Conformation of the M2 Transmembrane Peptide Proton Channel of Influenza A Virus from 19F Solid-State NMR. J. Phys. Chem. B 2007, 111, 10825–10832. [PubMed: 17705425]

(85). Nishimura K; Kim S; Zhang L; Cross TA, The Closed State of a H+ Channel Helical Bundle Combining Precise Orientational and Distance Restraints from Solid State NMR. Biochemistry 2002, 41, 13170–13177. [PubMed: 12403618]

(86). Williams JK; Shcherbakov AA; Wang J; Hong M, Protonation Equilibria and Pore-Opening Structure of the Dual-Histidine Influenza B Virus M2 Transmembrane Proton Channel from Solid-State NMR. J. Biol. Chem 2017, 292, 17876–17884. [PubMed: 28893910]

(87). Kwon B; Roos M; Mandala VS; Shcherbakov AA; Hong M; Lane Gilchrist M; Monde K; Tomita Y; Iwashita T; Nakanishi Ket al. , Elucidating Relayed Proton Transfer through a His–Trp–His Triad of a Transmembrane Proton Channel by Solid-State NMR. J. Mol. Biol 2019, 431, 2554–2566. [PubMed: 31082440]

(88). Salnikov ES; Raya J; De Zotti M; Zaitseva E; Peggion C; Ballano G; Toniolo C; Raap J; Bechinger B, Alamethicin Supramolecular Organization in Lipid Membranes from 19F Solid-State NMR. Biophys. J 2016, 111, 2450–2459. [PubMed: 27926846]

(89). Salnikov ES; De Zotti M; Bobone S; Mazzuca C; Raya J; Siano AS; Peggion C; Toniolo C; Stella L; Bechinger B, Trichogin Ga Iv Alignment and Oligomerization in Phospholipid Bilayers. Chembiochem 2019, 20, 2141–2150. [PubMed: 31125169]

(90). Mani R; Cady SD; Tang M; Waring AJ; Lehrer RI; Hong M, Membrane-Dependent Oligomeric Structure and Pore Formation of a Beta-Hairpin Antimicrobial Peptide in Lipid Bilayers from Solid-State NMR. Proc. Natl. Acad. Sci. U. S. A 2006, 103, 16242–16247. [PubMed: 17060626]

(91). Tang M; Waring AJ; Hong M, Intermolecular Packing and Alignment in an Ordered B-Hairpin Antimicrobial Peptide Aggregate from 2D Solid-State NMR. J. Am. Chem. Soc 2005, 127, 13919–13927. [PubMed: 16201813]

(92). Zhang Y; Lu W; Hong M, The Membrane-Bound Structure and Topology of a Human A-Defensin Indicate a Dimer Pore Mechanism for Membrane Disruption. Biochemistry 2010, 49, 9770–9782. [PubMed: 20961099]

(93). Su Y; Doherty T; Waring AJ; Ruchala P; Hong M, Roles of Arginine and Lysine Residues in the Translocation of a Cell-Penetrating Peptide from (13)C, (31)P, and (19)F Solid-State NMR. Biochemistry 2009, 48, 4587–4595. [PubMed: 19364134]

(94). Lee M; Yao H; Kwon B; Waring AJ; Ruchala P; Singh C; Hong M, Conformation and Trimer Association of the Transmembrane Domain of the Parainfluenza Virus Fusion Protein in Lipid Bilayers from Solid-State NMR: Insights into the Sequence Determinants of Trimer Structure and Fusion Activity J. Mol. Biol 2018, 430, 695–709.

(95). Grage SL; Xu X; Schmitt M; Wadhwani P; Ulrich AS, (19)F-Labeling of Peptides Revealing Long-Range NMR Distances in Fluid Membranes. J. Phys. Chem. Lett 2014, 5, 4256–4259. [PubMed: 26273971]

(96). Bennett AE; Rienstra CM; Griffiths JM; Zhen W; Lansbury PT Jr.; Griffin RG, Homonuclear Radio Frequency-Driven Recoupling in Rotating Solids. J. Chem. Phys 1998, 108, 9463–9479.

(97). Lane Gilchrist M; Monde K; Tomita Y; Iwashita T; Nakanishi K; McDermott AE, Measurement of Interfluorine Distances in Solids. J. Magn. Reson 2001, 152, 1–6. [PubMed: 11531358]

(98). Chen Q; Schmidt-Rohr K, 19F and 13C NMR Signal Assignment and Analysis in a Perfluorinated Ionomer (Nafion) by Two-Dimensional Solid-State NMR. Macromolecules 2004, 37, 5995–6003.

(99). Roos M; Mandala VS; Hong M, Determination of Long-Range Distances by Fast Magic-Angle-Spinning Radiofrequency-Driven (19)F-(19)F Dipolar Recoupling NMR. J. Phys. Chem. B 2018, 122, 9302–9313. [PubMed: 30211552]

(100). Ishii Y, 13C-13C Dipolar Recoupling under Very Fast Magic Angle Spinning in Solid-State Nuclear Magnetic Resonance: Applications to Distance Measurements, Spectral Assignments, and High-Throughput Secondary-Structure Determination. J. Chem. Phys 2001, 114, 8473–8483.

(101). Quinn CM; Zadorozhnyi R; Struppe J; Sergeyev IV; Gronenborn AM; Polenova T, Fast 19F Magic-Angle Spinning Nuclear Magnetic Resonance for the Structural Characterization of Active Pharmaceutical Ingredients in Blockbuster Drugs. Anal. Chem 2021, 93, 13029–13037. [PubMed: 34517697]

(102). Fritz M; Kraus J; Quinn CM; Yap GPA; Struppe J; Sergeyev IV; Gronenborn AM; Polenova T, Measurement of Accurate Interfluorine Distances in Crystalline Organic Solids: A High-Frequency Magic Angle Spinning NMR Approach. J. Phys. Chem. B 2019, 123, 10680–10690. [PubMed: 31682453]

(103). Reif B, Ultra-High Resolution in MAS Solid-State NMR of Perdeuterated Proteins: Implications for Structure and Dynamics. J. Magn. Reson 2012, 216, 1–12. [PubMed: 22280934]

(104). Paulson EK; Morcombe CR; Gaponenko V; Dancheck B; Byrd RA; Zilm KW, High-Sensitivity Observation of Dipolar Exchange and Noes between Exchangeable Protons in Proteins by

3D Solid-State NMR Spectroscopy. J. Am. Chem. Soc 2003, 125, 14222–14223. [PubMed: 14624539]

(105). Barbet-Massin E; Pell AJ; Retel JS; Andreas LB; Jaudzems K; Franks WT; Nieuwkoop AJ; Hiller M; Higman V; Guerry Pet al. , Rapid Proton-Detected NMR Assignment for Proteins with Fast Magic Angle Spinning. J. Am. Chem. Soc 2014, 136, 12489–12497. [PubMed: 25102442]

(106). Penzel S; Smith AA; Agarwal V; Hunkeler A; Org ML; Samoson A; Böckmann A; Ernst M; Meier BH, Protein Resonance Assignment at MAS Frequencies Approaching 100 kHz: A Quantitative Comparison of J-Coupling and Dipolar-Coupling-Based Transfer Methods. J. Biomol. NMR 2015, 63, 165–186. [PubMed: 26267840]

(107). Andreas LB; Le Marchand T; Jaudzems K; Pintacuda G, High-Resolution Proton-Detected NMR of Proteins at Very Fast MAS. J. Magn. Reson 2015, 253, 36–49. [PubMed: 25797003]

(108). Ji Y; Liang L; Bao X; Hou G, Recent Progress in Dipolar Recoupling Techniques under Fast MAS in Solid-State NMR Spectroscopy; Elsevier B.V, 2021; Vol. 112.

(109). Vasa SK; Rovó P; Linser R, Protons as Versatile Reporters in Solid-State NMR Spectroscopy. Acc. Chem. Res 2018, 51, 1386–1395. [PubMed: 29763290]

(110). Zhang R; Mroue KH; Ramamoorthy A, Proton-Based Ultrafast Magic Angle Spinning Solid-State NMR Spectroscopy. Acc. Chem. Res 2017, 50, 1105–1113. [PubMed: 28353338]

(111). Duong NT; Raran-Kurussi S; Nishiyama Y; Agarwal V, Can Proton-Proton Recoupling in Fully Protonated Solids Provide Quantitative, Selective and Efficient Polarization Transfer? J. Magn. Reson 2020, 317, 106777–106777. [PubMed: 32619889]

(112). Zhou DH; Shea JJ; Nieuwkoop AJ; Franks WT; Wylie BJ; Mullen C; Sandoz D; Rienstra CM, Solid-State Protein-Structure Determination with Proton-Detected Triple-Resonance 3D Magic-Angle-Spinning NMR Spectroscopy. Angew. Chem. Int. Ed. Engl 2007, 46, 8380–8383. [PubMed: 17907259]

(113). Grohe K; Nimerovsky E; Singh H; Vasa SK; Söldner B; Vögeli B; Rienstra CM; Linser R, Exact Distance Measurements for Structure and Dynamics in Solid Proteins by Fast-Magic-Angle-Spinning NMR. Chem. Commun 2019, 55, 7899–7902.

(114). Linser R; Bardiaux B; Higman V; Fink U; Reif B, Structure Calculation from Unambiguous Long-Range Amide and Methyl 1H-1H Distance Restraints for a Microcrystalline Protein with MAS Solid-State NMR Spectroscopy. J. Am. Chem. Soc 2011, 133, 5905–5912. [PubMed: 21434634]

(115). Andreas LB; Jaudzems K; Stanek J; Lalli D; Bertarelloa A; Marchand TL; De Paepe DC; Kotelovica S; Akopjana I; Knott Bet al. , Structure of Fully Protonated Proteins by Proton-Detected Magic- Angle Spinning NMR. Proc. Natl. Acad. Sci. U. S. A 2016, 113, 9187–9192. [PubMed: 27489348]

(116). Verel R; Ernst M; Meier BH, Adiabatic Dipolar Recoupling in Solid-State NMR: The Dream Scheme. J. Magn. Reson 2001, 150, 81–99. [PubMed: 11330986]

(117). Huber M; Hiller S; Schanda P; Ernst M; Böckmann A; Verel R; Meier BH, A Proton-Detected 4D Solid-State NMR Experiment for Protein Structure Determination. Chemphyschem 2011, 12, 915–918. [PubMed: 21442705]

(118). Agarwal V; Penzel S; Szekely K; Cadalbert R; Testori E; Oss A; Past J; Samoson A; Ernst M; Böckmann Aet al. , De Novo 3D Structure Determination from Sub-Milligram Protein Samples by Solid-State 100 kHz MAS NMR Spectroscopy. Angew. Chem. Int. Ed. Engl 2014, 53, 12253–12256. [PubMed: 25225004]

(119). Jain MG; Lalli D; Stanek J; Gowda C; Prakash S; Schwarzer TS; Schubeis T; Castiglione K; Andreas LB; Madhu PKet al. , Selective 1H-1H Distance Restraints in Fully Protonated Proteins by Very Fast Magic-Angle Spinning Solid-State NMR. J. Phys. Chem. Lett 2017, 8, 2399–2405. [PubMed: 28492324]

(120). Jain MG; Mote KR; Madhu PK, NMR Crystallography at Fast Magic-Angle Spinning Frequencies: Application of Novel Recoupling Methods. Crystals 2019, 9, 231.

(121). Potnuru LR; Duong NT; Sasank B; Raran-Kurussi S; Nishiyama Y; Agarwal V, Selective (1)H-(1)H Recoupling Via Symmetry Sequences in Fully Protonated Samples at Fast Magic Angle Spinning. J. Magn. Reson 2021, 328, 107004. [PubMed: 34049237]

(122). Zhang Z; Oss A; Org ML; Samoson A; Li M; Tan H; Su Y; Yang J, Selectively Enhanced 1H-1H Correlations in Proton-Detected Solid-State NMR under Ultrafast MAS Conditions. J. Phys. Chem. Lett 2020, 11, 8077–8083. [PubMed: 32880459]

(123). Wittmann JJ; Hendriks L; Meier BH; Ernst M, Controlling Spin Diffusion by Tailored Rf-Irradiation Schemes. Chem. Phys. Lett 2014, 608, 60–67.

(124). Duong NT; Raran-Kurussi S; Nishiyama Y; Agarwal V, Quantitative 1H-1H Distances in Protonated Solids by Frequency-Selective Recoupling at Fast Magic Angle Spinning NMR. J. Phys. Chem. Lett 2018, 9, 5948–5954. [PubMed: 30247041]

(125). Potnuru LR; Duong NT; Ahlawat S; Raran-Kurussi S; Ernst M; Nishiyama Y; Agarwal V, Accuracy of 1H-1H Distances Measured Using Frequency Selective Recoupling and Fast Magic-Angle Spinning. J. Chem. Phys 2020, 153.

(126). Wittmann JJ; Agarwal V; Hellwagner J; Lends A; Cadalbert R; Meier BH; Ernst M, Accelerating Proton Spin Diffusion in Perdeuterated Proteins at 100 khz MAS. J. Biomol. NMR 2016, 66, 233–242. [PubMed: 27803998]

(127). Schledorn M; Malär AA; Torosyan A; Penzel S; Klose D; Oss A; Org ML; Wang S; Lecoq L; Cadalbert Ret al. , Protein NMR Spectroscopy at 150 kHz Magic-Angle Spinning Continues to Improve Resolution and Mass Sensitivity. Chembiochem 2020, 21, 2540–2548. [PubMed: 32501630]

(128). Kotschy J; Linser R, Proton-Detected Solid-State NMR and Its Applications to Membrane Proteins; IOP Publishing, 2020.

(129). Li M; Xu W; Su Y, Solid-State NMR Spectroscopy in Pharmaceutical Sciences. Trends in Analytical Chemistry 2021, 135, 116152.

(130). Kobayashi T; Mao K; Paluch P; Nowak-Krõl A; Sniechowska J; Nishiyama Y; Gryko DT; Potrzebowski MJ; Pruski M, Study of Intermolecular Interactions in the Corrole Matrix by Solid-State NMR under 100 kHz MAS and Theoretical Calculations. Angew. Chem. Int. Ed. Engl 2013, 52, 14108–14111. [PubMed: 24227750]

(131). Schütz AK, Solid-State NMR Approaches to Investigate Large Enzymes in Complex with Substrates and Inhibitors. Biochem. Soc. Trans 2021, 49, 131–144. [PubMed: 33367567]

(132). Schubeis T; Le Marchand T; Andreas LB; Pintacuda G, 1H Magic-Angle Spinning NMR Evolves as a Powerful New Tool for Membrane Proteins. J. Magn. Reson 2018, 287, 140–152. [PubMed: 29413327]

(133). Lecoq L; Fogeron ML; Meier BH; Nassal M; Böckmann A, Solid-State NMR for Studying the Structure and Dynamics of Viral Assemblies. Viruses 2020, 12.

(134). David G; Fogeron ML; Schledorn M; Montserret R; Haselmann U; Penzel S; Badillo A; Lecoq L; André P; Nassal Met al. , Structural Studies of Self-Assembled Subviral Particles: Combining Cell-Free Expression with 110 kHz MAS NMR Spectroscopy. Angew. Chem. Int. Ed. Engl 2018, 57, 4787–4791. [PubMed: 29457857]

(135). Lecoq L; Schledorn M; Wang S; Smith-Penzel S; Malär AA; Callon M; Nassal M; Meier BH; Böckmann A, 100 kHz MAS Proton-Detected NMR Spectroscopy of Hepatitis B Virus Capsids. Front. Mol. Biosci 2019, 6.

(136). Jirasko V; Lakomek NA; Penzel S; Fogeron ML; Bartenschlager R; Meier BH; Böckmann A, Proton-Detected Solid-State NMR of the Cell-Free Synthesized A-Helical Transmembrane Protein Ns4b from Hepatitis C Virus. Chembiochem 2020, 21, 1453–1460. [PubMed: 31850615]

(137). Andreas LB; Reese M; Eddy MT; Gelev V; Ni QZ; Miller EA; Emsley L; Pintacuda G; Chou JJ; Griffin RG, Structure and Mechanism of the Influenza A M218–60 Dimer of Dimers. J. Am. Chem. Soc 2015, 137, 14877–14886. [PubMed: 26218479]

(138). Zinke M; Fricke P; Lange S; Zinn-Justin S; Lange A, Protein–Protein Interfaces Probed by Methyl Labeling and Proton-Detected Solid-State NMR Spectroscopy. Chemphyschem 2018, 19, 2457–2460. [PubMed: 29917302]

(139). Zinke M; Sachowsky KAA; Öster C; Zinn-Justin S; Ravelli R; Schröder GF; Habeck M; Lange A, Architecture of the Flexible Tail Tube of Bacteriophage Spp1. Nat. Commun 2020, 11, 5759. [PubMed: 33188213]

(140). Zinke M; Fricke P; Samson C; Hwang S; Wall JS; Lange S; Zinn-Justin S; Lange A, Bacteriophage Tail-Tube Assembly Studied by Proton-Detected 4D Solid-State NMR. Angew. Chem. Int. Ed. Engl 2017, 56, 9497–9501. [PubMed: 28644511]

(141). Gardner KH; Kay LE, Production and Incorporation of 15N, 13C, 2H (1H- 1 Methyl) Isoleucine into Proteins for Multidimensional NMR Studies. J. Am. Chem. Soc 1997, 119, 7599–7600.

(142). Sinnige T; Daniëls M; Baldus M; Weingarth M, Proton Clouds to Measure Long-Range Contacts between Nonexchangeable Side Chain Protons in Solid-State NMR. J. Am. Chem. Soc 2014, 136, 4452–4455. [PubMed: 24467345]

(143). Retel JS; Nieuwkoop AJ; Hiller M; Higman VA; Barbet-Massin E; Stanek J; Andreas LB; Franks WT; Van Rossum BJ; Vinothkumar KRet al. , Structure of Outer Membrane Protein G in Lipid Bilayers. Nat. Commun 2017, 8. [PubMed: 28364116]

(144). Schubeis T; Le Marchand T; Daday C; Kopec W; Movellan KT; Stanek J; Schwarzer TS; Castiglione K; de Groot BL; Pintacuda Get al. , A B-Barrel for Oil Transport through Lipid Membranes: Dynamic NMR Structures of Alkl. Proc. Natl. Acad. Sci. U. S. A 2020, 117, 21014–21021. [PubMed: 32817429]

(145). Bardiaux B; Malliavin T; Nilges M, Aria for Solution and Solid-State NMR. Methods Mol. Biol 2012, 831, 453–483. [PubMed: 22167687]

(146). Brünger AT; Adams PD; Clore GM; Delano WL; Gros P; Grossekunstleve RW; Jiang JS; Kuszewski J; Nilges M; Pannu NSet al. , Crystallography & NMR System: A New Software Suite for Macromolecular Structure Determination. Acta Crystallogr. D 1998, 54, 905–921. [PubMed: 9757107]

(147). Medeiros-Silva J; Mance D; Daniëls M; Jekhmane S; Houben K; Baldus M; Weingarth M, 1H-Detected Solid-State NMR Studies of Water-Inaccessible Proteins in Vitro and in Situ. Angew. Chem. Int. Ed. Engl 2016, 55, 13606–13610. [PubMed: 27671832]

(148). Medeiros-Silva J; Jekhmane S; Paioni AL; Gawarecka K; Baldus M; Swiezewska E; Breukink E; Weingarth M, High-Resolution NMR Studies of Antibiotics in Cellular Membranes. Nat. Commun 2018, 9, 3963–3963. [PubMed: 30262913]

(149). Huster D; Yao XL; Hong M, Membrane Protein Topology Probed by 1H Spin Diffusion from Lipids Using Solid-State NMR Spectroscopy. J. Am. Chem. Soc 2002, 124, 874–883. [PubMed: 11817963]

(150). Lesage A; Gardiennet C; Loquet A; Verel R; Pintacuda G; Emsley L; Meier BH; Böckmann A, Polarization Transfer over the Water-Protein Interface in Solids. Angew. Chem. Int. Ed. Engl 2008, 47, 5851–5854. [PubMed: 18613186]

(151). Najbauer EE; Movellan KT; Schubeis T; Schwarzer T; Castiglione K; Giller K; Pintacuda G; Becker S; Andreas LB, Probing Membrane Protein Insertion into Lipid Bilayers by Solid-State NMR. Chemphyschem 2019, 20, 302–310. [PubMed: 30452110]

(152). Shi C; Öster C; Bohg C; Li L; Lange S; Chevelkov V; Lange A, Structure and Dynamics of the Rhomboid Protease Glpg in Liposomes Studied by Solid-State NMR. J. Am. Chem. Soc 2019, 141, 17314–17321. [PubMed: 31603315]

(153). Weingarth M; Van Der Cruijsen EAW; Ostmeyer J; Lievestro S; Roux B; Baldus M, Quantitative Analysis of the Water Occupancy around the Selectivity Filter of a K+ Channel in Different Gating Modes. J. Am. Chem. Soc 2014, 136, 2000–2007. [PubMed: 24410583]

(154). Jekhmane S; Medeiros-Silva J; Li J; Kümmerer F; Müller-Hermes C; Baldus M; Roux B; Weingarth M, Shifts in the Selectivity Filter Dynamics Cause Modal Gating in K + Channels. Nat. Commun 2019, 10, 123–123. [PubMed: 30631074]

(155). Hong M; Fritzsching KJ; Williams JK, Hydrogen-Bonding Partner of the Proton-Conducting Histidine in the Influenza M2 Proton Channel Revealed from 1H Chemical Shifts. J. Am. Chem. Soc 2012, 134, 14753–14755. [PubMed: 22931093]

(156). Movellan KT; Wegstroth M; Overkamp K; Leonov A; Becker S; Andreas LB, Imidazole-Imidazole Hydrogen Bonding in the Ph-Sensing Histidine Side Chains of Influenza A M2. J. Am. Chem. Soc 2020, 142, 2704–2708. [PubMed: 31970979]

(157). Singh H; Vasa SK; Jangra H; Rovó P; Päslack C; Das CK; Zipse H; Schäfer LV; Linser R, Fast Microsecond Dynamics of the Protein-Water Network in the Active Site of Human Carbonic

Anhydrase Ii Studied by Solid-State NMR Spectroscopy. J. Am. Chem. Soc 2019, 141, 19276–19288. [PubMed: 31647225]

(158). Yang Y; Xiang S; Liu X; Pei X; Wu P; Gong Q; Li N; Baldus M; Wang S, Proton-Detected Solid-State NMR Detects the Inter-Nucleotide Correlations and Architecture of Dimeric Rna in Microcrystals. Chem. Commun 2017, 53, 12886–12889.

(159). Wiegand T; Malär AA; Cadalbert R; Ernst M; Böckmann A; Meier BH, Asparagine and Glutamine Side-Chains and Ladders in Het-S(218–289) Amyloid Fibrils Studied by Fast Magic-Angle Spinning NMR. Front. Mol. Biosci 2020, 7, 261–261.

(160). Daskalov A; Martinez D; Coustou V; Mammeri NE; Mélanie B; Andreas LB; Bardiaux B; Stanek J; Noubhani A; Kauffmann Bet al. , Structural and Molecular Basis of Cross-Seeding Barriers in Amyloids. Proc. Natl. Acad. Sci. U. S. A 2020, 118.

(161). Wasmer C; Lange A; Van Melckebeke H; Siemer AB; Riek R; Meier BH, Amyloid Fibrils of the Het-S(218–289) Prion Form a Beta Solenoid with a Triangular Hydrophobic Core. Science 2008, 319, 1523–1526. [PubMed: 18339938]

(162). Rydzek S; Shein M; Bielytskyi P; Schütz AK, Observation of a Transient Reaction Intermediate Illuminates the Mechanochemical Cycle of the Aaa-Atpase P97. J. Am. Chem. Soc 2020, 142, 14472–14480. [PubMed: 32790300]

(163). Schanda P; Triboulet S; Laguri C; Bougault CM; Ayala I; Callon M; Arthur M; Simorre JP, Atomic Model of a Cell-Wall Cross-Linking Enzyme in Complex with an Intact Bacterial Peptidoglycan. J. Am. Chem. Soc 2014, 136, 17852–17860. [PubMed: 25429710]

(164). Kosol S; Gallo A; Griffiths D; Valentic TR; Masschelein J; Jenner M; de los Santos ELC; Manzi L; Sydor PK; Rea Det al. , Structural Basis for Chain Release from the Enacyloxin Polyketide Synthase. Nat. Chem 2019, 11, 913–923. [PubMed: 31548674]

(165). Felix J; Weinhäupl K; Chipot C; Dehez F; Hessel A; Gauto DF; Morlot C; Abian O; Gutsche I; Velazquez-Campoy Aet al. , Mechanism of the Allosteric Activation of the Clpp Protease Machinery by Substrates and Active-Site Inhibitors. Sci. Adv 2019, 5.

(166). Gauto DF; Macek P; Barducci A; Fraga H; Hessel A; Terauchi T; Gajan D; Miyanoiri Y; Boisbouvier J; Lichtenecker Ret al. , Aromatic Ring Dynamics, Thermal Activation, and Transient Conformations of a 468 Kda Enzyme by Specific 1H-13C Labeling and Fast Magic-Angle Spinning NMR. J. Am. Chem. Soc 2019, 141, 11183–11195. [PubMed: 31199882]

(167). Vasa SK; Singh H; Grohe K; Linser R, Assessment of a Large Enzyme–Drug Complex by Proton-Detected Solid-State NMR Spectroscopy without Deuteration. Angew. Chem. Int. Ed. Engl 2019, 58, 5758–5762. [PubMed: 30688395]

(168). Shukla R; Medeiros-Silva J; Parmar A; Vermeulen BJA; Das S; Paioni AL; Jekhmane S; Lorent J; Bonvin AMJJ; Baldus Met al. , Mode of Action of Teixobactins in Cellular Membranes. Nat. Commun 2020, 11, 1–10. [PubMed: 31911652]

(169). Öster C; Walkowiak GP; Hughes DE; Spoering AL; Peoples AJ; Catherwood AC; Tod JA; Lloyd AJ; Herrmann T; Lewis Ket al. , Structural Studies Suggest Aggregation as One of the Modes of Action for Teixobactin. Chem. 2018, 9, 8850–8859.

(170). Ward ME; Ritz E; Ahmed MAM; Bamm VV; Harauz G; Brown LS; Ladizhansky V, Proton Detection for Signal Enhancement in Solid-State NMR Experiments on Mobile Species in Membrane Proteins. J. Biomol. NMR 2015, 63, 375–388. [PubMed: 26494649]

(171). Xiang SQ; le Paige UB; Horn V; Houben K; Baldus M; van Ingen H, Site-Specific Studies of Nucleosome Interactions by Solid-State NMR Spectroscopy. Angew. Chem. Int. Ed. Engl 2018, 57, 4571–4575. [PubMed: 29465771]

(172). Lacabanne D; Boudet J; Malär AA; Wu P; Cadalbert R; Salmon L; Allain FHT; Meier BH; Wiegand T, Protein Side-Chain-DNA Contacts Probed by Fast Magic-Angle Spinning NMR. J. Phys. Chem. B 2020, 124, 11089–11097. [PubMed: 33238710]

(173). Wiegand T; Schledorn M; Malär AA; Cadalbert R; Däpp A; Terradot L; Meier BH; Böckmann A, Nucleotide Binding Modes in a Motor Protein Revealed by 31P- and 1H-Detected MAS Solid-State NMR Spectroscopy. Chembiochem 2020, 21, 324–330. [PubMed: 31310428]

(174). Gauto DF; Estrozi LF; Schwieters CD; Effantin G; Macek P; Sounier R; Sivertsen AC; Schmidt E; Kerfah R; Mas Get al. , Integrated NMR and Cryo-Em Atomic-Resolution Structure

Determination of a Half-Megadalton Enzyme Complex. Nat. Commun 2019, 10, 2697. [PubMed: 31217444]

(175). Struppe J; Quinn CM; Sarkar S; Gronenborn AM; Polenova T, Ultrafast 1H MAS NMR Crystallography for Natural Abundance Pharmaceutical Compounds. Mol. Pharm 2020, 17, 674–682. [PubMed: 31891271]

(176). Stöppler D; Macpherson A; Smith-Penzel S; Basse N; Lecomte F; Deboves H; Taylor RD; Norman T; Porter J; Waters LCet al. , Insight into Small Molecule Binding to the Neonatal Fc Receptor by X-Ray Crystallography and 100 kHz Magic-Angle-Spinning NMR. PLoS Biol. 2018, 16.

(177). Li M; Lu X; Xu W; Troup GM; McNevin MJ; Nie H; Su Y, Quantifying Pharmaceutical Formulations from Proton Detected Solid-State NMR under Ultrafast Magic Angle Spinning. J. Pharm. Sci 2020, 109, 3045–3053. [PubMed: 32679211]

(178). Hirsh DA; Wijesekara AV; Carnahan SL; Hung I; Lubach JW; Nagapudi K; Rossini AJ, Rapid Characterization of Formulated Pharmaceuticals Using Fast MAS 1H Solid-State NMR Spectroscopy. Mol. Pharm 2019, 16, 3121–3132. [PubMed: 31095913]

(179). Nishiyama Y, Fast Magic-Angle Sample Spinning Solid-State NMR at 60–100khz for Natural Abundance Samples. Solid State Nucl. Magn. Reson 2016, 78, 24–36. [PubMed: 27400153]

(180). Li M; Meng F; Tsutsumi Y; Amoureux J-P; Xu W; Lu X; Zhang F; Su Y, Understanding Molecular Interactions in Rafoxanide–Povidone Amorphous Solid Dispersions from Ultrafast Magic Angle Spinning NMR. Mol. Pharm 2020, 17, 2196–2207. [PubMed: 32392076]

(181). Malär AA; Dong S; Kehr G; Erker G; Meier BH; Wiegand T, Characterization of H2-Splitting Products of Frustrated Lewis Pairs: Benefit of Fast Magic-Angle Spinning. Chemphyschem 2019, 20, 672–679. [PubMed: 30663843]

(182). Varghese S; Halling PJ; Häussinger D; Wimperis S, Two-Dimensional 1H and 1H-Detected NMR Study of a Heterogeneous Biocatalyst Using Fast MAS at High Magnetic Fields. Solid State Nucl. Magn. Reson 2018, 92, 7–11. [PubMed: 29587153]

(183). Mroue KH; Nishiyama Y; Kumar Pandey M; Gong B; McNerny E; Kohn DH; Morris MD; Ramamoorthy A, Proton-Detected Solid-State NMR Spectroscopy of Bone with Ultrafast Magic Angle Spinning. Sci. Rep 2015, 5.

(184). Damron JT; Kersten KM; Pandey MK; Mroue KH; Yarava JR; Nishiyama Y; Matzger AJ; Ramamoorthy A, Electrostatic Constraints Assessed by 1H MAS NMR Illuminate Differences in Crystalline Polymorphs. J. Phys. Chem. Lett 2017, 8, 4253–4257. [PubMed: 28825828]

(185). Paluch P; Trébosc J; Amoureux JP; Potrzebowski MJ, 1H-31P Cpvc NMR Method under Very Fast Magic Angle Spinning for Analysis of Dipolar Interactions and Dynamics Processes in the Crystalline Phosphonium Tetrafluoroborate Salts. Solid State Nucl. Magn. Reson 2017, 87, 96–103. [PubMed: 28602610]

(186). Szeverenyi NM; Sullivan MJ; Maciel GE, Observation of Spin Exchange by Two-Dimensional Fourier Transform 13C Cross Polarization-Magic-Angle Spinning. J. Magn. Reson 1982, 47, 462–475.

(187). Meier BH, Polarization Transfer and Spin Diffusion in Solid-State NMR. Adv. Magn. Opt. Reson 1994, 18, 1–115.

(188). Takegoshi K; Nakamura S; Terao T, 13C–1H Dipolar-Assisted Rotational Resonance in Magic-Angle Spinning NMR. Chem. Phys. Lett 2001, 344, 631–637.

(189). Takegoshi K; Nakamura S; Terao T, 13C–1H Dipolar-Driven 13C–13C Recoupling without 13C RF Irradiation in Nuclear Magnetic Resonance of Rotating Solids. J. Chem. Phys 2003, 118, 2325–2341.

(190). Weingarth M; Demco DE; Bodenhausen G; Tekely P, Improved Magnetization Transfer in Solid-State NMR with Fast Magic Angle Spinning. Chem. Phys. Lett 2009, 469, 342–348.

(191). Weingarth M; Bodenhausen G; Tekely P, Broadband Magnetization Transfer Using Moderate Radio-Frequency Fields for NMR with Very High Static Fields and Spinning Speeds. Chem. Phys. Lett 2010, 488, 10–16.

(192). Hu B; Lafon O; Trébosc J; Chen Q; Amoureux JP, Broad-Band Homo-Nuclear Correlations Assisted by 1H Irradiation for Bio-Molecules in Very High Magnetic Field at Fast and Ultra-Fast MAS Frequencies. J. Magn. Reson 2011, 212, 320–329. [PubMed: 21873091]

(193). Tuttle MD; Comellas G; Nieuwkoop AJ; Covell DJ; Berthold DA; Kloepper KD; Courtney JM; Kim JK; Barclay AM; Kendall Aet al. , Solid-State NMR Structure of a Pathogenic Fibril of Full-Length Human A-Synuclein. Nat. Struct. Mol. Biol 2016, 23, 409–415. [PubMed: 27018801]

(194). Gelenter MD; Smith KJ; Liao SY; Mandala VS; Dregni AJ; Lamm MS; Tian Y; Xu W; Pochan DJ; Tucker TJet al. , The Peptide Hormone Glucagon Forms Amyloid Fibrils with Two Coexisting B-Strand Conformations. Nat. Struct. Mol. Biol 2019, 26, 592–598. [PubMed: 31235909]

(195). Lu M; Russell RW; Bryer AJ; Quinn CM; Hou G; Zhang H; Schwieters CD; Perilla JR; Gronenborn AM; Polenova T, Atomic-Resolution Structure of Hiv-1 Capsid Tubes by Magic-Angle Spinning NMR. Nat. Struct. Mol. Biol 2020, 27, 863–869. [PubMed: 32901160]

(196). Lewandowski JR; De Paëpe G; Griffin RG, Proton Assisted Insensitive Nuclei Cross Polarization. J. Am. Chem. Soc 2007, 129, 728–729. [PubMed: 17243786]

(197). De Paëpe G; Lewandowski JR; Loquet A; Böckmann A; Griffin RG, Proton Assisted Recoupling and Protein Structure Determination. J. Chem. Phys 2008, 129, 245101. [PubMed: 19123534]

(198). Hing AW; Vega S; Schaefer J, Transferred-Echo Double-Resonance NMR. J. Magn. Reson 1992, 96, 205–209.

(199). Jaroniec CP; Filip C; Griffin RG, 3D Tedor NMR Experiments for the Simultaneous Measurement of Multiple Carbon-Nitrogen Distances in Uniformly (13)C,(15)N-Labeled Solids. J. Am. Chem. Soc 2002, 124, 10728–10742. [PubMed: 12207528]

(200). Lewandowski JR; De Paëpe G; Eddy MT; Struppe J; Maas W; Griffin RG, Proton Assisted Recoupling at High Spinning Frequencies. J. Phys. Chem. B 2009, 113, 9062–9069. [PubMed: 19489532]

(201). Lewandowski JR; De Paëpe G; Eddy MT; Griffin RG, (15)N-(15)N Proton Assisted Recoupling in Magic Angle Spinning NMR. J. Am. Chem. Soc 2009, 131, 5769–5776. [PubMed: 19334788]

(202). Donovan KJ; Silvers R; Linse S; Griffin RG, 3D MAS NMR Experiment Utilizing through-Space (15)N-(15)N Correlations. J. Am. Chem. Soc 2017, 139, 6518–6521. [PubMed: 28447786]

(203). De Paëpe G; Lewandowski JR; Loquet A; Eddy M; Megy S; Böckmann A; Griffin RG, Heteronuclear Proton Assisted Recoupling. J. Chem. Phys 2011, 134, 095101. [PubMed: 21384999]

(204). Nielsen AB; Székely K; Gath J; Ernst M; Nielsen NC; Meier BH, Simultaneous Acquisition of Par and Pain Spectra. J. Biomol. NMR 2012, 52, 283–288. [PubMed: 22371268]

(205). Lamley JM; Lewandowski JR, Simultaneous Acquisition of Homonuclear and Heteronuclear Long-Distance Contacts with Time-Shared Third Spin Assisted Recoupling. J. Magn. Reson 2012, 218, 30–34. [PubMed: 22578552]

(206). Gelenter MD; Dregni AJ; Hong M, Pulsed Third-Spin-Assisted Recoupling NMR for Obtaining Long-Range (13)C-(13)C and (15)N-(13)C Distance Restraints. J. Phys. Chem. B 2020, 124, 7138–7151. [PubMed: 32700540]

(207). Gelenter MD; Hong M, Efficient (15)N-(13)C Polarization Transfer by Third-Spin-Assisted Pulsed Cross-Polarization Magic-Angle-Spinning NMR for Protein Structure Determination. J. Phys. Chem. B 2018, 122, 8367–8379. [PubMed: 30106585]

(208). Donovan KJ; Jain SK; Silvers R; Linse S; Griffin RG, Proton-Assisted Recoupling (Par) in Peptides and Proteins. J. Phys. Chem. B 2017, 121, 10804–10817. [PubMed: 29043804]

(209). Lewandowski JR; van der Wel PC; Rigney M; Grigorieff N; Griffin RG, Structural Complexity of a Composite Amyloid Fibril. J. Am. Chem. Soc 2011, 133, 14686–14698. [PubMed: 21766841]

(210). Lu JX; Qiang W; Yau WM; Schwieters CD; Meredith SC; Tycko R, Molecular Structure of B-Amyloid Fibrils in Alzheimer's Disease Brain Tissue. Cell 2013, 154, 1257–1268. [PubMed: 24034249]

(211). Colvin MT; Silvers R; Ni QZ; Can TV; Sergeyev I; Rosay M; Donovan KJ; Michael B; Wall J; Linse Set al. , Atomic Resolution Structure of Monomorphic Aβ42 Amyloid Fibrils. J. Am. Chem. Soc 2016, 138, 9663–9674. [PubMed: 27355699]

(212). Wälti MA; Ravotti F; Arai H; Glabe CG; Wall JS; Böckmann A; Güntert P; Meier BH; Riek R, Atomic-Resolution Structure of a Disease-Relevant Aβ(1–42) Amyloid Fibril. Proc. Natl. Acad. Sci. U. S. A 2016, 113, E4976–4984. [PubMed: 27469165]

(213). Schütz AK; Vagt T; Huber M; Ovchinnikova OY; Cadalbert R; Wall J; Güntert P; Böckmann A; Glockshuber R; Meier BH, Atomic-Resolution Three-Dimensional Structure of Amyloid B Fibrils Bearing the Osaka Mutation. Angew. Chem. Int. Ed. Engl 2015, 54, 331–335. [PubMed: 25395337]

(214). Seuring C; Verasdonck J; Gath J; Ghosh D; Nespovitaya N; Wälti MA; Maji SK; Cadalbert R; Güntert P; Meier BHet al. , The Three-Dimensional Structure of Human B-Endorphin Amyloid Fibrils. Nat. Struct. Mol. Biol 2020, 27, 1178–1184. [PubMed: 33046908]

(215). Rufo CM; Moroz YS; Moroz OV; Stohr J; Smith TA; Hu XZ; DeGrado WF; Korendovych IV, Short Peptides Self-Assemble to Produce Catalytic Amyloids. Nat. Chem 2014, 6, 303–309. [PubMed: 24651196]

(216). Lee M; Wang T; Makhlynets OV; Wu Y; Polizzi NF; Wu H; Gosavi PM; Stöhr J; Korendovych IV; DeGrado WFet al. , Zinc-Binding Structure of a Catalytic Amyloid from Solid-State NMR. Proc. Natl. Acad. Sci. U. S. A 2017, 114, 6191–6196. [PubMed: 28566494]

(217). Mompeán M; Li W; Li J; Laage S; Siemer AB; Bozkurt G; Wu H; McDermott AE, The Structure of the Necrosome Ripk1-Ripk3 Core, a Human Hetero-Amyloid Signaling Complex. Cell 2018, 173, 1244–1253.e1210. [PubMed: 29681455]

(218). Kang X; Kirui A; Muszy ski A; Widanage MCD; Chen A; Azadi P; Wang P; Mentink-Vigier F; Wang T, Molecular Architecture of Fungal Cell Walls Revealed by Solid-State NMR. Nat. Commun 2018, 9, 2747. [PubMed: 30013106]

(219). Lange A; Luca S; Baldus M, Structural Constraints from Proton-Mediated Rare-Spin Correlation Spectroscopy in Rotating Solids. J. Am. Chem. Soc 2002, 124, 9704–9705. [PubMed: 12175218]

(220). Wang S; Munro RA; Shi L; Kawamura I; Okitsu T; Wada A; Kim SY; Jung KH; Brown LS; Ladizhansky V, Solid-State NMR Spectroscopy Structure Determination of a Lipid-Embedded Heptahelical Membrane Protein. Nat. Methods 2013, 10, 1007–1012. [PubMed: 24013819]

(221). Demers JP; Habenstein B; Loquet A; Kumar Vasa S; Giller K; Becker S; Baker D; Lange A; Sgourakis NG, High-Resolution Structure of the Shigella Type-Iii Secretion Needle by Solid-State NMR and Cryo-Electron Microscopy. Nat. Commun 2014, 5, 4976. [PubMed: 25264107]

(222). Tycko R; Ishii Y, Constraints on Supramolecular Structure in Amyloid Fibrils from Two-Dimensional Solid-State NMR Spectroscopy with Uniform Isotopic Labeling. J. Am. Chem. Soc 2003, 125, 6606–6607. [PubMed: 12769550]

(223). Vasa S; Lin L; Shi C; Habenstein B; Riedel D; Kühn J; Thanbichler M; Lange A, B-Helical Architecture of Cytoskeletal Bactofilin Filaments Revealed by Solid-State NMR. Proc. Natl. Acad. Sci. U. S. A 2015, 112, E127–136. [PubMed: 25550503]

(224). Zhang Z; Bulloch EM; Bunker RD; Baker EN; Squire CJ, Structure and Function of Glmu from Mycobacterium Tuberculosis. Acta Crystallogr. D 2009, 65, 275–283. [PubMed: 19237750]

(225). Hoop CL; Lin HK; Kar K; Magyarfalvi G; Lamley JM; Boatz JC; Mandal A; Lewandowski JR; Wetzel R; van der Wel PC, Huntingtin Exon 1 Fibrils Feature an Interdigitated B-Hairpin-Based Polyglutamine Core. Proc. Natl. Acad. Sci. U. S. A 2016, 113, 1546–1551. [PubMed: 26831073]

(226). Marchanka A; Simon B; Althoff-Ospelt G; Carlomagno T, Rna Structure Determination by Solid-State NMR Spectroscopy. Nat. Commun 2015, 6, 7024. [PubMed: 25960310]

(227). Boudet J; Devillier JC; Wiegand T; Salmon L; Meier BH; Lipps G; Allain FH, A Small Helical Bundle Prepares Primer Synthesis by Binding Two Nucleotides That Enhance Sequence-Specific Recognition of the DNA Template. Cell 2019, 176, 154–166.e113. [PubMed: 30595448]

(228). Gakh YG; Gakh AA; Gronenborn AM, Fluorine as an NMR Probe for Structural Studies of Chemical and Biological Systems. Magn. Reson. Chem 2000, 38, 551–558.

(229). Kitevski-LeBlanc JL; Prosser RS, Current Applications of 19F NMR to Studies of Protein Structure and Dynamics. Prog. Nucl. Magn. Reson. Spectrosc 2012, 62, 1–33. [PubMed: 22364614]

(230). Sharaf NG; Gronenborn AM, 19F-Modified Proteins and 19F-Containing Ligands as Tools in Solution NMR Studies of Protein Interactions; Kelman Z, Ed.; Academic Press, 2015; Vol. 565.
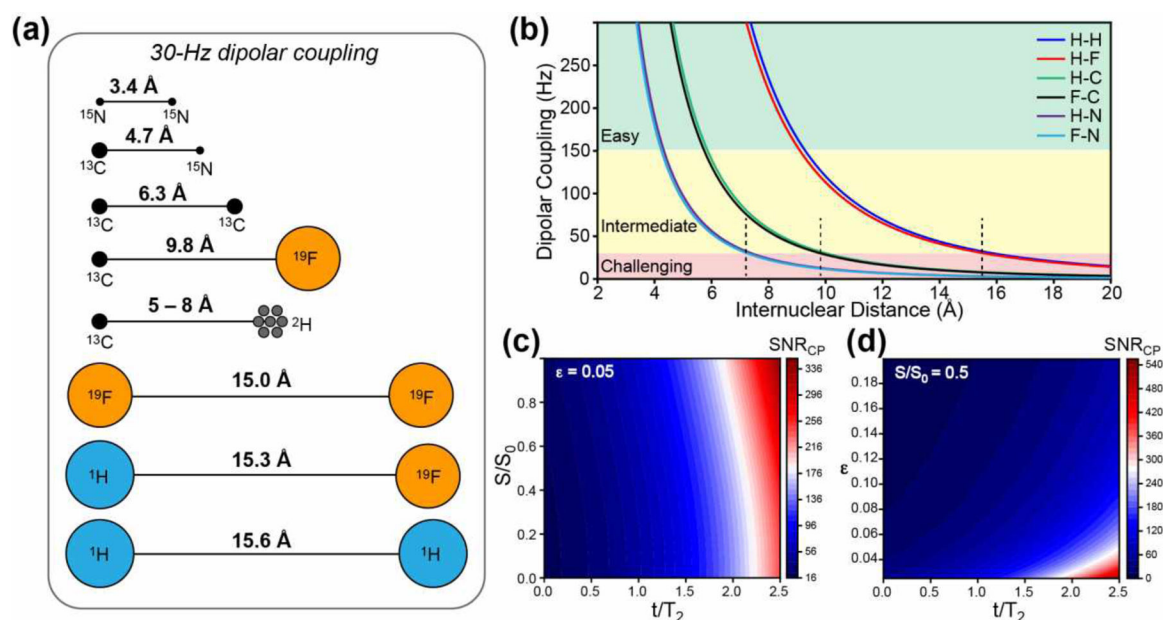
(231). Arntson KE; Pomerantz WCK, Protein-Observed Fluorine NMR: A Bioorthogonal Approach for Small Molecule Discovery. J. Med. Chem 2016, 59, 5158–5171. [PubMed: 26599421]

Figure 1.
Distance rulers in solid-state NMR spectroscopy. (**a**) Schematic representation of distances corresponding to a 30-Hz dipolar coupling between NMR-active nuclei that are commonly studied in biological systems. (**b**) Dipolar coupling strength as a function of internuclear distance for common spin pairs. The longest distances measurable for the intermediate difficulty regime of 30–150 Hz are marked by dashed lines. These distance upper bounds are ~7 Å for ^{1}H-^{15}N and ^{19}F-^{15}N spin pairs, ~10 Å for ^{1}H-^{13}C and ^{19}F-^{13}C spin pairs, and ~15 Å for ^{1}H-^{1}H and ^{1}H-^{19}F spin pairs. (**c**) Required CP sensitivity as a function of the REDOR dephasing value S/S_0 and T_2-parameterized REDOR mixing time t/T_2, if an uncertainty ε of 0.05 is desired for the measured S/S_0 value. (**d**) Required CP sensitivity as a function of the desired uncertainty ε and t/T_2 for an S/S_0 value of 0.5.
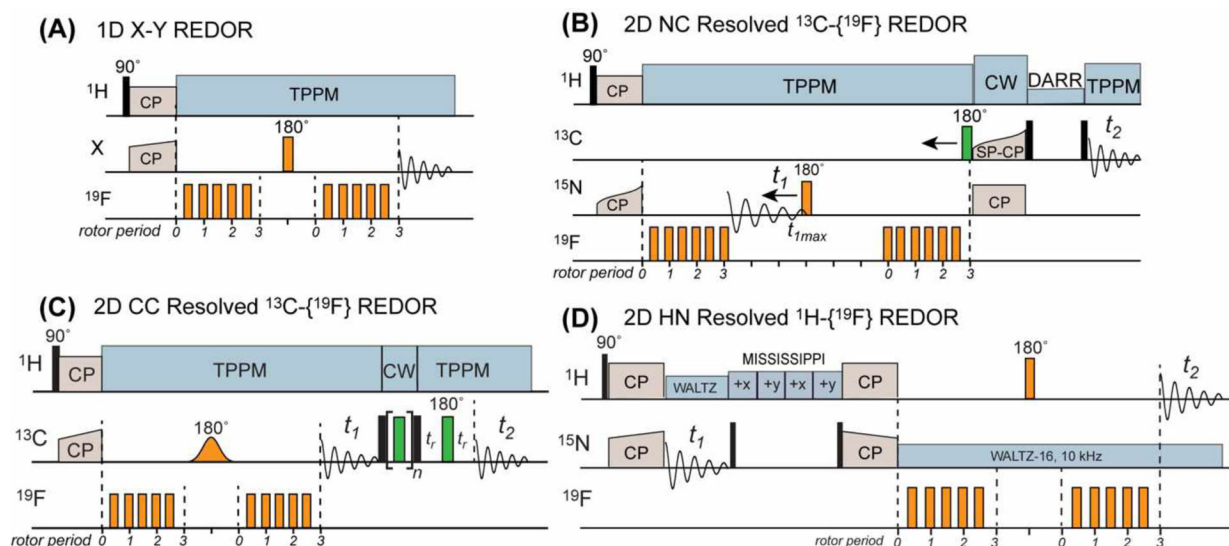
Figure 2.
^{19}F-based REDOR pulse sequences for measuring long distances. (**A**) Standard 1D X-^{19}F REDOR, where the X nucleus can be ^{13}C, ^{31}P, ^{15}N, or other nuclei[10]. For simplicity, the version of REDOR with most 180° pulses on the ^{19}F channel is shown, but other variations such as alternating 180° pulses on the two channels can also be implemented. (**B**) 2D ^{15}N-^{13}C resolved ^{13}C-^{19}F REDOR (FRESH) pulse sequence[21]. (**C**) 2D ^{13}C-^{13}C resolved ^{13}C-^{19}F REDOR pulse sequence[22]. The ^{13}C polarization transfer is implemented using RFDR here, but other polarization transfer schemes such as Dipolar-Assisted Rotational Resonance (DARR) can also be used. An optional pre-detection Hahn echo allows the measurement of spectra with a clean baseline. (**D**) 2D ^{15}N-^{1}H resolved ^{1}H-^{19}F REDOR[23].
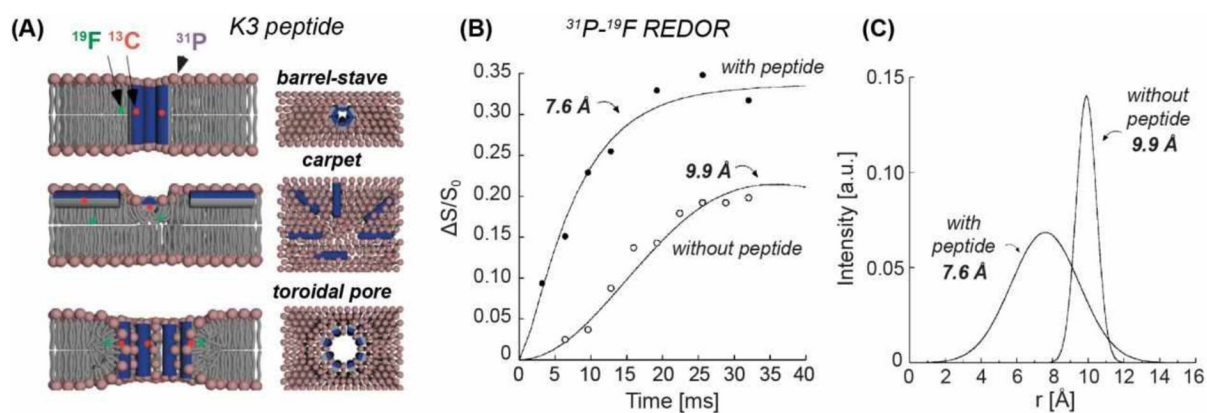
Figure 3.
^{31}P-^{19}F REDOR for studying the structure of the antimicrobial peptide K3[34]. **(A)** Structural and mechanistic models of K3 in lipid membranes. The barrel-stave mode shows minimal membrane disorder and a small pore. The carpet model shows more membrane disorder but no pore. The toroid model shows both membrane disorder and a large pore. **(B)** ^{31}P-^{19}F REDOR dephasing curves between the lipid headgroup ^{31}P and the fluorinated lipid tail. Peptide binding shortened the P-F distance from 9.9 Å to 7.6 Å. **(C)** Comparison of the distance distributions between the peptide-free and peptide-bound lipid membranes. K3 binding increased the distance distribution, indicating increased membrane disorder. These data support the toroidal-pore model as the mechanism of membrane disruption by K3.[34,35]
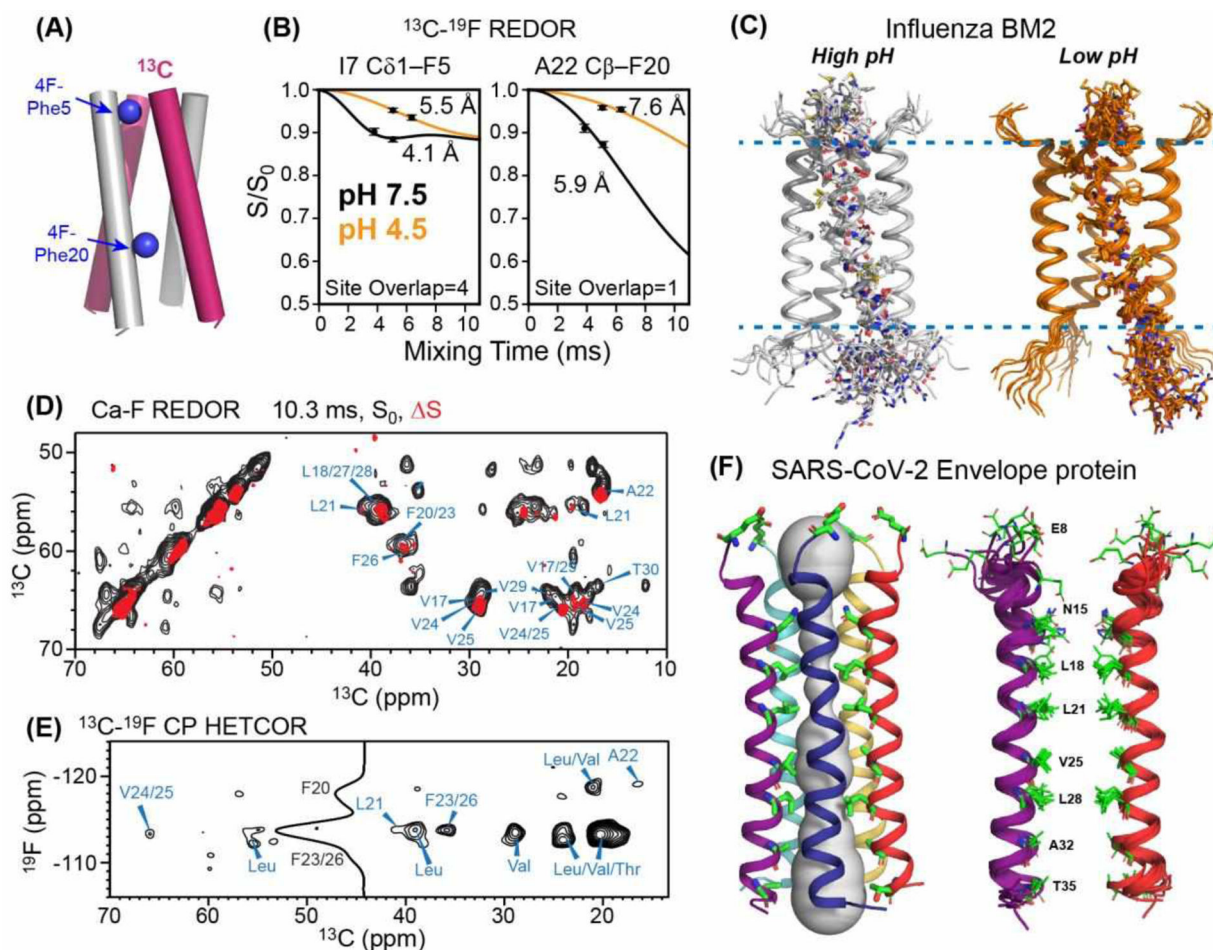
Figure 4.
[19]F-based heteronuclear distance measurements to determine membrane protein structures. **(A)** Mixed ^{13}C and ^{19}F labeling strategy for measuring interhelical distances in influenza BM2 tetramers[45]. **(B)** Representative [13]C-^{19}F REDOR data of BM2. The interhelical distances increase from high pH to low pH, indicating that the four-helix bundle is loosened at low pH. **(C)** BM2 tetramer structures at high and low pH (PDB 6PVR and 6PVT). **(D)** 2D [13]C-^{13}C resolved [13]C-^{19}F REDOR spectra of the SARS-CoV-2 envelope protein TMD in lipid bilayers. Control spectrum (S_0, black) is overlaid with the difference spectrum (ΔS, red) to show which residues are the closest to the fluorinated Phe residues. **(E)** 2D [13]C-^{19}F HETCOR spectrum to assign the fluorinated Phe residues that are close to each [13]C. **(F)** ETM structure determined in part using these [13]C-^{19}F distance restraints. The pentameric helical bundle (left) has a highly hydrophobic pore, as shown for two helices on the right for clarity[46] (PDB 7K3G).
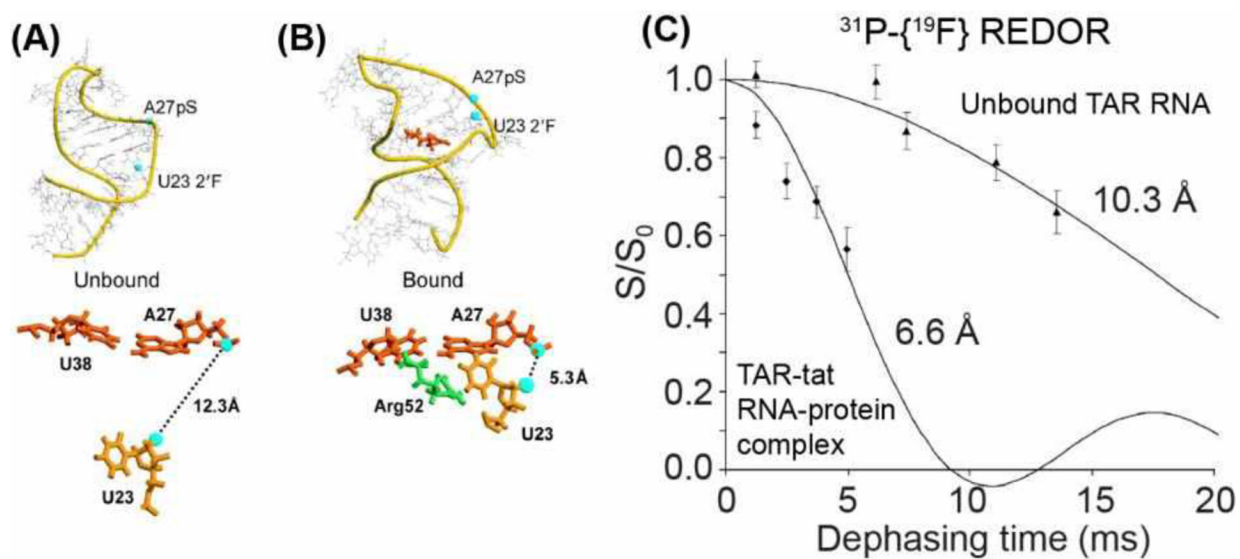
Figure 5.
^{31}P-^{19}F REDOR for distance measurements in the tat-TAR complex[56]. **(A)** Solution NMR model of TAR RNA (PDB 1ANR), showing locations of the pS-tagged A27 and the fluorodeoxyuridine at U23. **(B)** Model of tat-bound TAR RNA (PDB 1ANJ), showing a decrease of the ^{31}P-^{19}F distance. The structural model shows that binding of R52 in tat changes the RNA conformation. **(C)** ^{31}P-^{19}F REDOR dephasing indicates that tat binding shortened the distance between pS-A27 and fluoro-U23[56].
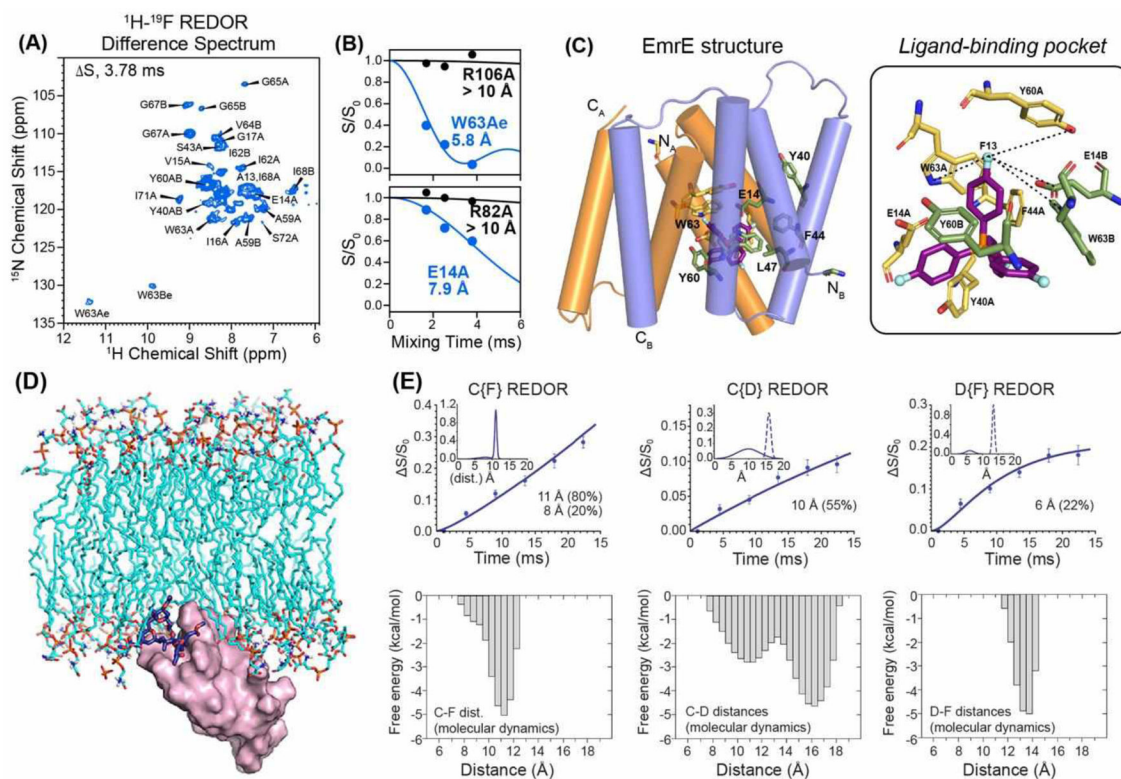
Figure 6.
^{19}F NMR for studying ligand binding to proteins. **(A)** 2D NH-resolved [1]H-^{19}F REDOR difference (ΔS) spectrum of EmrE in DMPC bilayers[65]. The difference peaks indicate residues in close proximity to the fluorinated ligand, F_4-TPP$^+$. **(B)** Representative [1]H-^{19}F REDOR dephasing curves and best-fit simulations. **(C)** Distance-restrained structure of TPP-bound EmrE. Key residues in the binding pocket are shown on the right (PDB 7JK8). **(D)** Model of Protein Kinase C (magenta) and a Bryostatin analog (dark blue sticks)[66]. **(E)** [13]C-^{19}F, [13]C-^{2}H and [2]H-^{19}F REDOR dephasing curves and best-fit simulations of the bryostatin analog. The corresponding distance distributions obtained from molecular dynamics (MD) simulations are shown below each REDOR data panel[66].
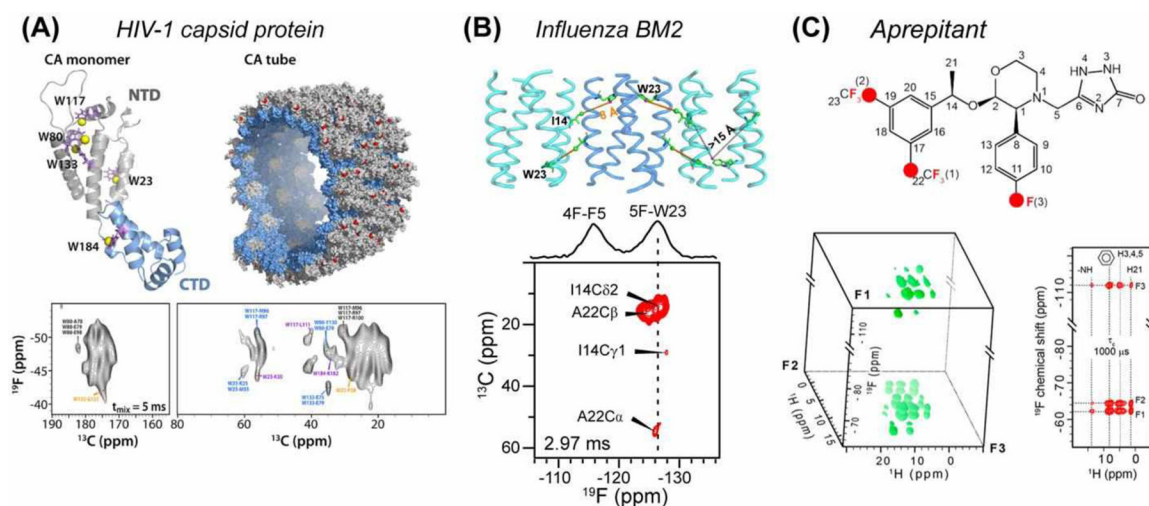
Figure 7.

2D and 3D ^{19}F-X HETCOR experiments for structure determination. **(A)** HIV-1 capsid protein (CA) structure, showing 5F-Trp residues in yellow in the monomer (PDB 4XFX) and red in the capsid tubes[68] (PDB 3J4F). DNP sensitivity-enhanced 2D ^{19}F-^{13}C HETCOR spectra were measured using ^{19}F-^{13}C CP. Many ^{13}C-^{19}F correlations for distances > 7 Å were observed. **(B)** Clustering of the influenza BM2 tetramers in lipid bilayers is revealed by cross peaks between ^{13}C-labeled Ile14 and 5F-Trp23 in 2D ^{13}C-^{19}F HETCOR spectra[24]. **(C)** 3D ^{19}F-^{1}H-^{1}H experiments for studying the pharmaceutical drug aprepitant[69]. The 3D spectrum is shown on the left, while a 2D plane extracted from the F2 chemical shift of 8.1 ppm is shown on the right.
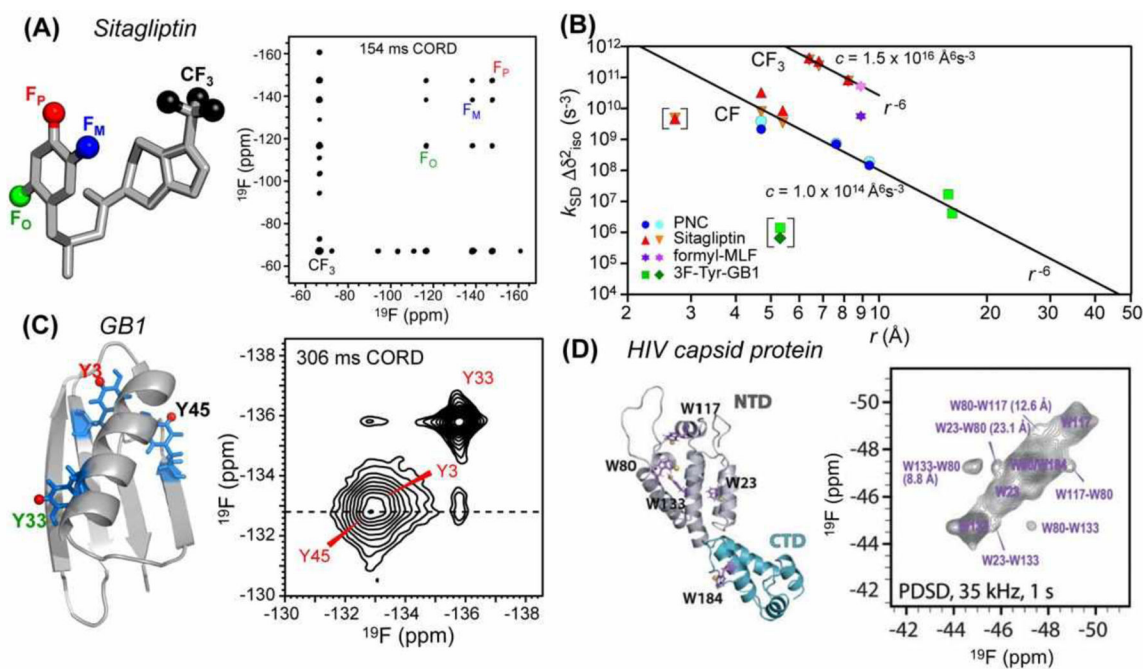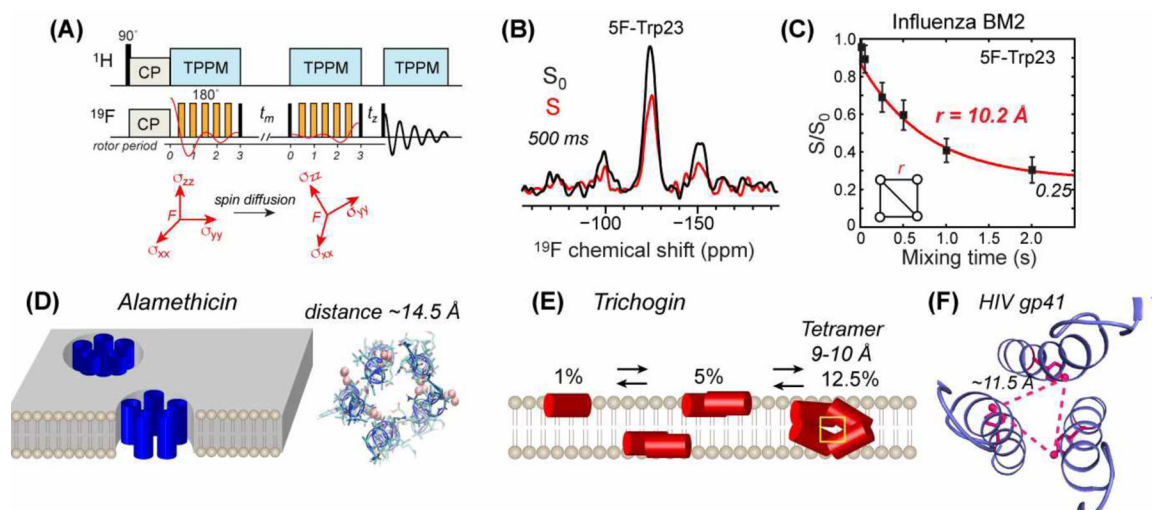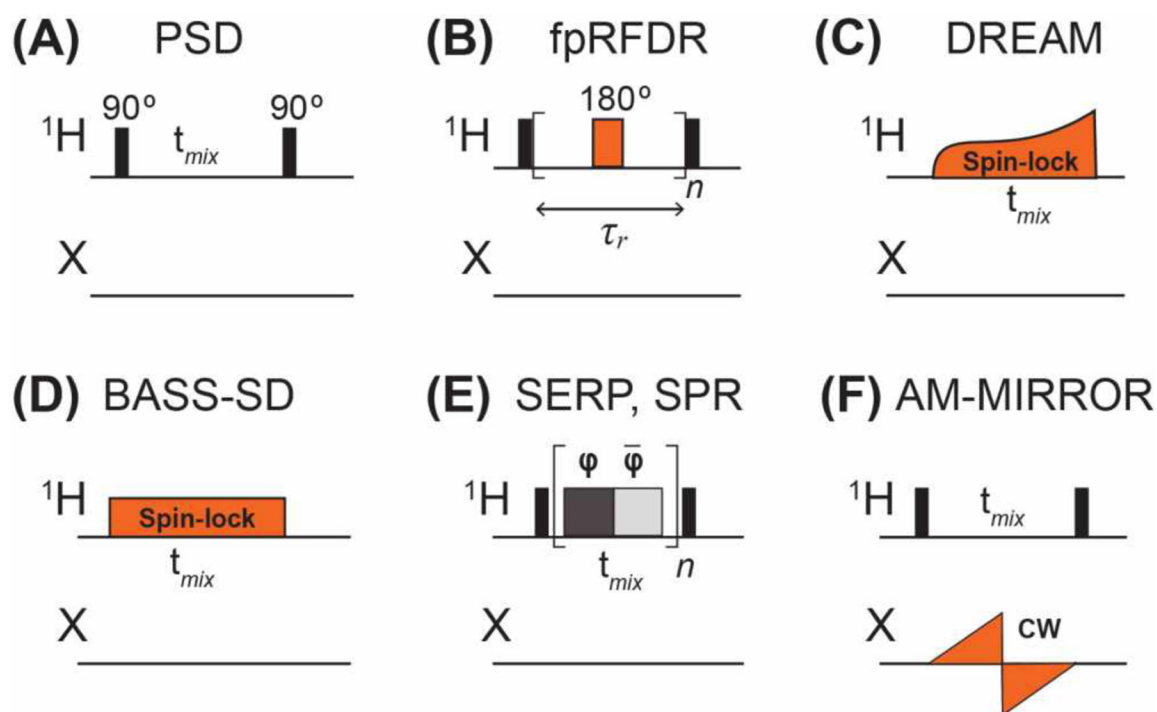
Figure 8.
^{19}F-^{19}F distance measurement using isotropic spin exchange. (**A**) Chemical structure of sitagliptin and its 2D ^{19}F spin diffusion spectrum measured with 154 ms CORD mixing[75]. (**B**) Chemical-shift corrected spin-exchange rates as a function of ^{19}F-^{19}F distances[75]. (**C**) 3F-Tyr-labeled GB1 (PDB 2JSV) and its 2D ^{19}F correlation spectrum, measured under 25 kHz MAS with 306 ms CORD mixing[75]. (**D**) 5F-Trp labeled HIV-1 CA monomer (PDB 4XFX), showing 5-^{19}F-Trp residues as purple sticks. 2D ^{19}F-^{19}F correlation spectrum of the tubular assemblies was measured under 35 kHz MAS using 1 s spin diffusion[76].

Figure 9.
Principles of ^{19}F spin diffusion CODEX and its applications to oligomeric membrane peptides and proteins. (**A**) ^{19}F CODEX pulse sequence and the principle of anisotropic spin diffusion between nuclei with different chemical shift tensor orientations[83]. (**B**) Representative ^{19}F CODEX control (S_0) and dephased (S) spectra, shown for 5F-Trp23 labeled influenza BM2 peptide[87]. (**C**) ^{19}F CODEX decay curve of 5F-Trp23 in BM2 shows an equilibrium S/S_0 value of 0.25, indicating that the peptide assembles into tetramers in lipid bilayers. Best-fit simulation gives a nearest-neighbor ^{19}F-^{19}F distance of 10.2 Å[87]. (**D**) Application of ^{19}F CODEX to alamethicin found that the peptide forms pentameric helical bundles at high concentrations[88]. (**E**) Application of ^{19}F CODEX to trichogin revealed concentration-dependent oligomeric structures[89]. (**F**) Application of ^{19}F CODEX to the HIV-1 fusion protein, gp41, constrained the trimer structure of the MPER-TMD segment[49] (PDB 6DLN).

Figure 10.
Selected pulse sequence elements for measuring ^{1}H-^{1}H distances under fast MAS. (**A**) ^{1}H spin diffusion (PSD). (**B**) The finite-pulse RFDR (fpRFDR) sequence involves a single 180° pulse per rotor period[100]. (**C**) The DREAM sequence uses an amplitude-modulated ^{1}H pulse whose field strength is swept across the HORROR condition, $\omega_1=\omega_r/2$[116]. (**D**) The BASS-SD sequence involves a ^{1}H spin-lock pulse at a field strength that spans the spectral region of interest to cause band-selective polarization transfer[119]. (**E**) The SERP and SPR sequences comprise a series of rotor-synchronized phase-modulated pulses. SERP is based on a $C2_2^1$ symmetry scheme where each pulse series block matches the rotation period[120,121]. SPR employs a user-defined CN_n symmetry scheme where the block length equals n times the rotation period[122]. (**F**) Reverse AM-MIRROR[123,124] comprises a sawtooth-shaped pulse on the X channel whose amplitude is defined by the chemical shift bandwidth of the X nucleus.
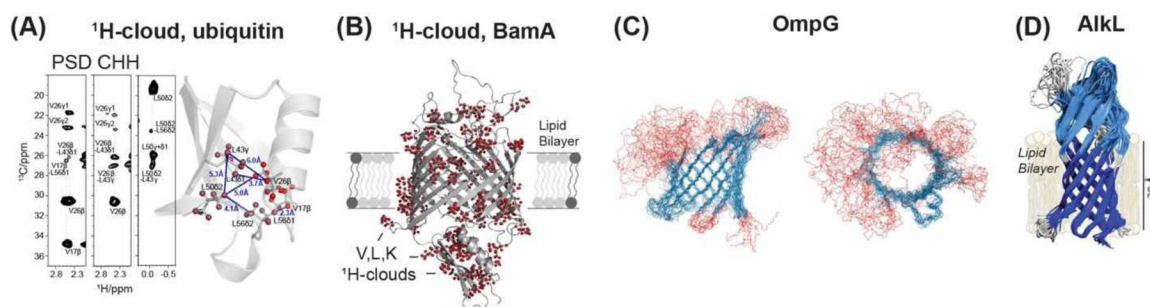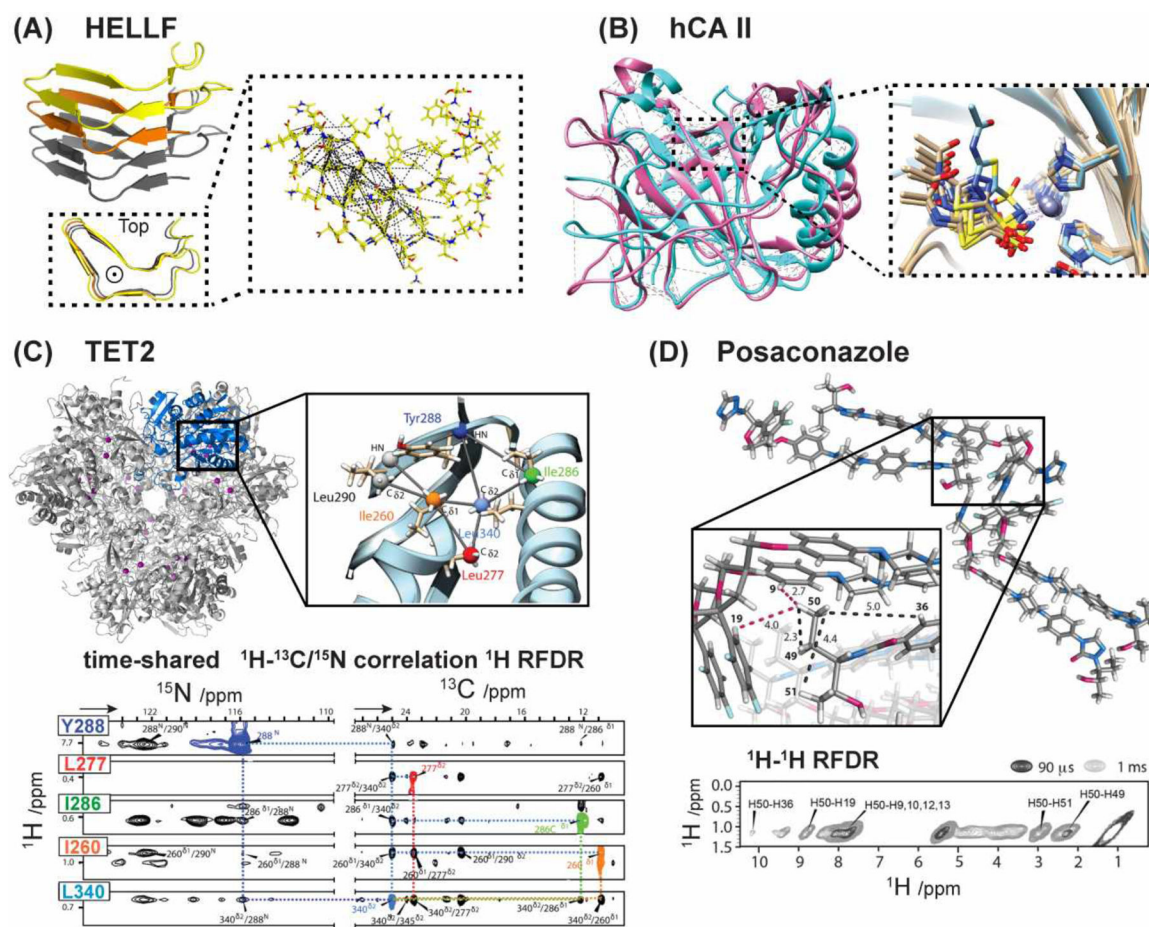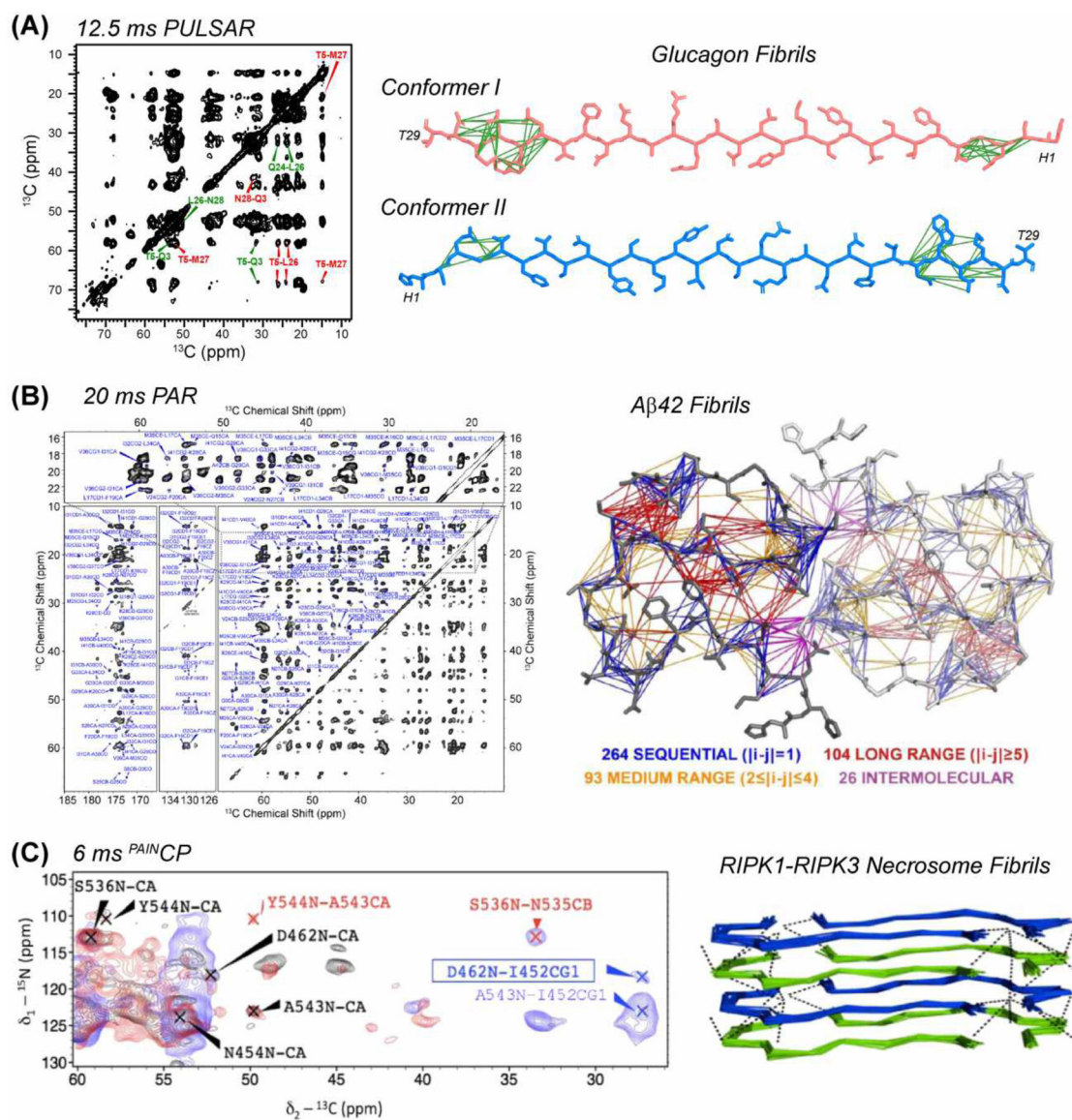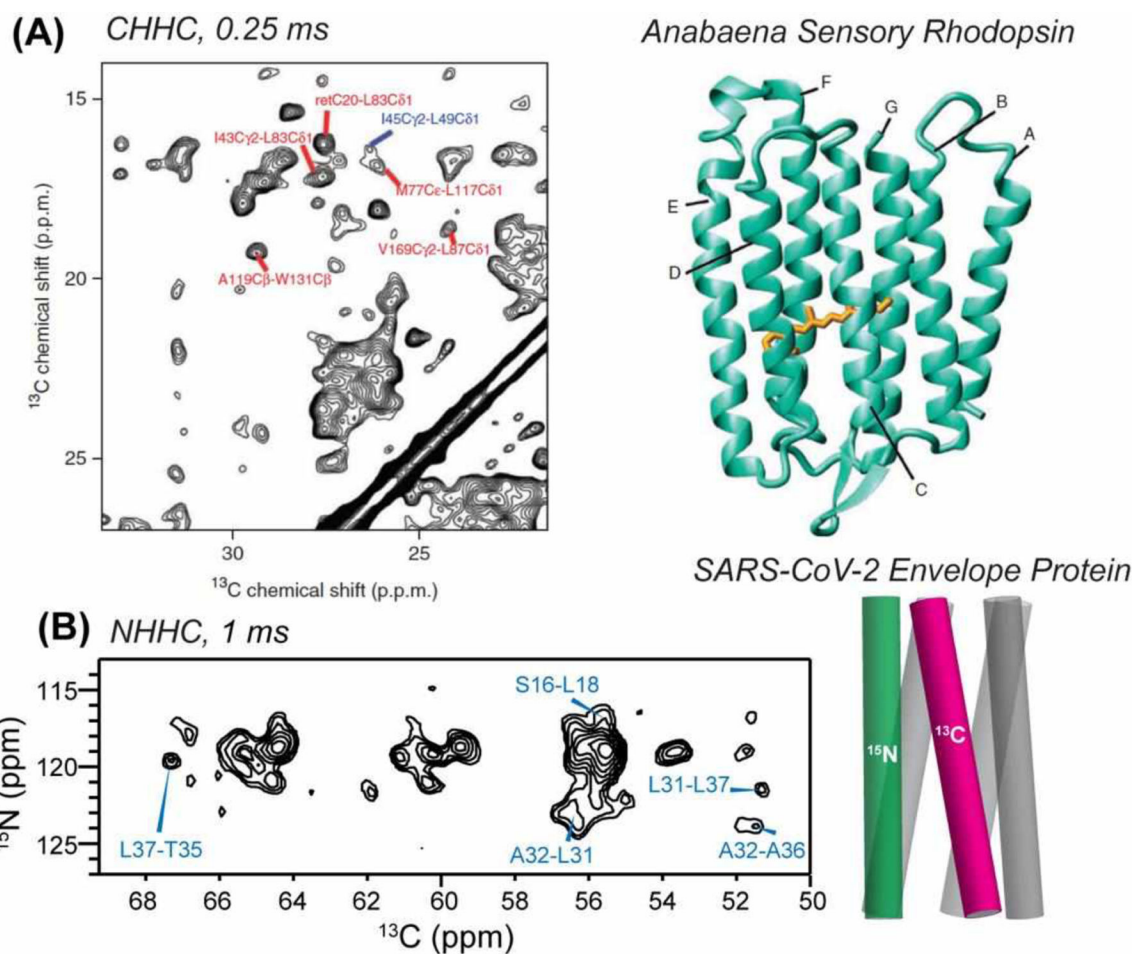
Figure 11.
Long-range ^{1}H-^{1}H distance measurements to determine virus protein structures. (**A**) Solid-state NMR structures of the viral capsid protein AP205CP (PDB 5JZR)[115]. (**B**) Intermolecular contacts of gp17.1 were measured using ^{1}H-^{1}H distance contacts in tailored labelled samples using RFDR mixing[138]. Reproduced with permission from reference[138]. Copyright 2018 Wiley.

Figure 12.

^{1}H-^{1}H distance experiments restrain the structure of membrane proteins. (**A**) Residue-specific ^{1}H-labeling (proton clouds) greatly reduces spectral congestion, as demonstrated on ubiquitin[142]. (**B**) Application of the proton cloud approach to structural studies of BamA[142] (PDB 4K3B). (**C**) Solid-state NMR structure of the β-barrel OmpG (PDB 5MWV) in *E. coli* lipid extracts[143]. (**D**) Solid-state NMR structure of the β-barrel AlkL (PDB 6QWR) in DMPC bilayers, determined using distance restraints obtained from ^{1}H-^{1}H RFDR and BASS-SD[144].

Figure 13.
^{1}H-^{1}H distance restraints obtained under fast MAS for determining the supramolecular structures. (**A**) Structure of the HELLF (209–277) amyloid protein (PDB 6EKA). ^{1}H-^{1}H distance restraints helped to define the rigid core[160]. (**B**) Solid-state NMR structure of the hCAII enzyme (magenta, PDB 6QEB) overlaid with the crystal structure (cyan, PDB 3HS4). The inhibitor aceazolamide binds the active site of the enzyme[167]. (**C**) Structure of the TET2 enzyme (PDB 6R8N) obtained from integrated analyses of NMR and cryo-EM data[174]. Representative 3D ^{1}H RFDR spectra and distance restraints are shown. (**D**) NMR crystallography of the antifungal compound Posaconazole[175]. Representative 2D ^{1}H-^{1}H RFDR spectra and measured distance restraints are shown.

Figure 14.
TSAR experiments for measuring long-range ^{13}C-^{13}C and ^{13}C-^{15}N distances to determine amyloid protein structures. (**A**) 12.5 ms ^{13}C-^{13}C PULSAR spectra of glucagon helped to determine antiparallel packing of this amyloid fibril[194,206] (PDB 6NZN). (**B**) 20 ms 2D ^{13}C PAR spectrum helped to determine the $A\beta_{42}$ fibril structure[211] (PDB 5KK3). (**C**) 6 ms 2D ^{15}N-^{13}C ^{PAIN}CP spectrum of RIPK1-RIPK3 necrosome fibrils and the resulting structure[217] (PDB 5V7Z).

Figure 15.
CHHC and NHHC distance experiments for studying membrane protein structure. (**A**) 0.25 ms 2D CHHC spectrum of *Anabaena* sensory rhodopsin[220] (PDB 2M3G). Unambiguous long-range distance restraints are assigned in red while medium-range distance restraints are assigned in blue. (**B**) 0.5 ms (in red) and 1.0 ms (in blue) 2D NHHC spectrum of the SARS-CoV-2 envelope protein[46]. ^{13}C-labeled and ^{15}N-labeled monomers were mixed at a 1:1 ratio to detect interhelical contacts.